POLITECNICO
MILANO 1863

SCUOLA DI INGEGNERIA INDUSTRIALE
E DELL'INFORMAZIONE

An innovative Fourier-transform hyperspectral microscope for excitation and emission spectroscopy

Tesi di Laurea Magistrale in
Engineering Physics- Ingegneria Fisica

Author: **Martina Riva**

Student ID: 221544
Advisor: Prof. Gianluca Valentini
Co-advisors: Dr. Cristian Manzoni
Academic Year: 2023-24

There is a driving force more powerful than steam, electricity and atomic energy: the will.

- Albert Einstein

Abstract

There are two approaches to measure the light spectrum. Dispersive spectroscopy separates the spectral components with dispersive elements. Fourier transform (FT) spectroscopy is a time-domain technique in which the spectrum is retrieved with the FT of the interference signal between two replicas of the radiation field, retarded by a variable delay in the two arms of an interferometer. This second approach brings in some relevant advantages in terms of throughput, signal-to-noise ratio, wavelength accuracy and tunable spectral resolution. Ordinary FT spectrometers are based on double-beam interferometers in which the two replicas travel along different paths; this causes problems in maintaining the interferometric stability between the two arms due to perturbations and vibrations. Politecnico di Milano and CNR developed a compact and ultrastable common-path birefringent interferometer (TWINS) that overcomes instability issues. It also enables a practical implementation of a hyperspectral imaging system in which the continuous spectrum of the light is recorded in parallel for all pixels of a 2D sensor. Since it provides both spectral and spatial information, spectral imaging is a versatile tool that has been applied to various fields, from microscopy to remote sensing.

In this Master's degree thesis we describe a multimodal FT hyperspectral microscope based on TWINS. Previous works already reported its versatility for reflectance, transmission, Raman and fluorescence emission measurements. Here, we aim to introduce an additional functionality: the acquisition of excitation spectra. This is obtained by temporally modulating a broadband source with a TWINS interferometer added in the illumination path of the microscope.

Excitation-resolved measurements typically provide complementary information to fluorescence emission spectroscopy. Still, there are cases in which they are preferable. For example, one advantageous aspect is the higher signal-to-noise ratio under equal incident power conditions. Moreover, they can be useful to discriminate a number of targets in the same field of view that have overlapping emission spectra. Typical excitation spectra are acquired by scanning the excitation wavelength and collecting the fluorescence signal in a narrowband spectral region; here, we adopt a time-domain approach in which all wavelengths, processed by an interferometer, excite the sample simultaneously.

A microscope for emission and excitation spectroscopy appears a promising tool for

sample investigation. We describe its implementation and present various measurements to demonstrate its multimodality, including tests to characterise and validate the efficacy of the FT excitation method.

Keywords: hyperspectral imaging; Fourier transform spectroscopy; microscopy; fluorescence; excitation imaging

Abstract in lingua italiana

Esistono due approcci per misurare lo spettro della luce. La spettroscopia dispersiva separa le componenti spettrali tramite elementi dispersivi. La spettroscopia a trasformata di Fourier è una tecnica nel dominio del tempo in cui lo spettro viene ottenuto come trasformata di Fourier del segnale di interferenza tra due repliche del campo di radiazione, ritardate di un ritardo variabile nei due bracci di un interferometro. Questo secondo approccio presenta alcuni vantaggi rilevanti in termini di *throughput*, rapporto segnale-rumore e possibilità di regolare la risoluzione spettrale. I comuni spettrometri a trasformata di Fourier si basano su interferometri in cui le due repliche viaggiano lungo percorsi diversi; questo causa problemi nel mantenere la stabilità interferometrica tra i due bracci a causa di perturbazioni e vibrazioni. Il Politecnico di Milano e il CNR hanno sviluppato un interferometro compatto e ultrastabile, a cammino ottico comune e birifrangente (TWINS) che supera i problemi di instabilità tipici di un interferometro con bracci distinti per le due repliche. Questo dispositivo consente anche l'implementazione pratica di un sistema di imaging iperspettrale in cui lo spettro continuo della luce viene registrato in parallelo per tutti i pixel di un sensore 2D. Poiché fornisce informazioni sia spettrali sia spaziali, l'imaging spettrale è uno strumento versatile applicato in vari campi, dalla microscopia al telerilevamento.

In questa tesi magistrale descriviamo un microscopio iperspettrale a trasformata di Fourier multimodale basato sul TWINS. Precedenti pubblicazioni hanno mostrato la sua versatilità per misure di riflettanza, trasmissione, Raman e emissione di fluorescenza. Qui, il nostro obiettivo è di introdurre una funzionalità aggiuntiva: l'acquisizione di spettri di eccitazione mediante la modulazione temporale di una sorgente a banda larga con un interferometro TWINS aggiunto nel ramo di illuminazione del microscopio.

Le misure risolte in eccitazione forniscono generalmente informazioni complementari alla spettroscopia di emissione di fluorescenza; tuttavia, ci sono casi in cui sono preferibili. Ad esempio, un aspetto vantaggioso è il rapporto segnale-rumore più elevato a parità di potenza incidente sul campione. Inoltre, possono essere utili per discriminare diversi target nello stesso campo di vista che si sovrappongono nello spettro di emissione. Gli spettri di eccitazione sono tipicamente acquisiti scansionando la lunghezza d'onda di eccitazione e raccogliendo il segnale di fluorescenza in una banda spettrale stretta; qui, adottiamo

un approccio nel dominio del tempo in cui tutte le lunghezze d'onda, processate da un interferometro, eccitano il campione simultaneamente.

Un microscopio per spettroscopia di emissione ed eccitazione sembra dunque uno strumento promettente per l'indagine dei campioni. Ne descriviamo l'implementazione e presentiamo varie misure per dimostrarne la multimodalità, inclusi test preliminari per caratterizzare e validare l'efficacia del sistema per l'analisi degli spettri di eccitazione.

Parole chiave: imaging iperspettrale; spettroscopia a trasformata di Fourier; microscopia; fluorescenza; imaging in eccitazione

Contents

List of Figures

List of Tables

Acronyms

CW continuous wave

EEM excitation-emission matrix

EMCCD electron multiplying charged coupled device

FFT fast Fourier transform

FID free induction decay

FOV field of view

FP fluorescent protein

FRET Förster resonance energy transfer

FT Fourier transform

FWHM full-width at half maximum

GECI genetically encoded Ca_{2+} indicator

HFV high fringe visibility

HSI hyperspectral imaging

IR infrared

NA numerical aperture

QE quantum efficiency

RGB red-green-blue

ROI region of interest

SNR signal-to-noise ratio

TWINS Translating-Wedge based Identical pulses eNcoding System

ZPD zero path delay

Introduction

Hyperspectral imaging is a powerful tool that has been used in a large variety of applications, from remote sensing to microscopy, from materials science to biology, because it combines both spatial and spectral information: each pixel of the image is associated with a continuous spectrum.

Two main techniques are available to measure the spectrum of light. Dispersive spectroscopy is based on dispersive elements (prisms or gratings) to separate the radiation into a series of wavelengths, such that their intensity can be measured in parallel with a linear detector array. Fourier transform (FT) spectroscopy is a time-domain technique that relies on Wiener-Kintchine's theorem to retrieve the spectrum from the autocorrelation signal of the radiation, called *interferogram*. It is the interference signal between two replicas of the incident light, retarded by a variable delay in the two arms of an interferometer. The FT approach brings in some advantages with respect to dispersive methods: (1) higher signal-to-noise ratio in a readout-noise-dominated regime (Fellgett's advantage); (2) higher throughput, due to the absence of slits (Jacquinot's advantage); (3) tunable spectral resolution, dependent on the interferometer scan range; (4) higher wavelength accuracy (Connes' advantage). Ordinary FT spectrometers are based on Michelson's interferometer: the two replicas of light are created with a beam splitter and travel two separated paths; the difference in optical path lengths establishes their reciprocal delay. This double-beam scheme has the problem of interferometric stability: any environmental vibration or perturbation can significantly affect the path length difference, therefore complex feedback loop systems are typically adopted for stabilization. A possible solution to this issue is a common-path configuration in which the replicas travel collinearly: since both optical paths fluctuate in the same amount, their difference is kept fixed. At Politecnico di Milano, in collaboration with CNR, a common-path birefringent interferometer, *Translating-Wedge based Identical pulses eNcoding System (TWINS)*, was developed [14]: its common-path configuration makes it robust to external vibrations, providing a delay accuracy of a small fraction of the optical cycle. The incident radiation is linearly polarized at 45° with respect to ordinary and extraordinary axes of a birefringent crystal. The two components of the field along the two axes propagate through two blocks of the same material, but with orthogonal optical axes, accumulating delays with opposite signs and

proportional to the propagation length. The total delay is then changed by varying the thickness of the material.

To acquire spectral information for all points of an extended source there are different strategies: collecting light of one pixel (or a line of pixels) at a time (*point* or *line-scanning* approach) or from the whole field of view simultaneously (*widefield imaging*). The latter is particularly interesting since it allows one to shorten the measurement time, but it typically requires a complex implementation. The FT spectrometer based on TWINS resulted to be suitable for this purpose, providing a simple parallel recording of spectra for all pixels of a 2D sensor; therefore, it has been coupled to different optical systems obtaining a hyperspectral camera [77] (also for macro imaging [5]) and a multimodal hyperspectral microscope [4], [17]. In this thesis work we focus on the latter: starting from the upgraded commercial microscope introduced in [4], used for fluorescence emission, Raman, reflectance and transmission measurements, we have developed an excitation path to measure excitation spectra of the sample.

Excitation spectra typically provide complementary information to emission ones and they may be even preferable. One advantage is that excitation-scanning gives an inherently higher signal-to-noise ratio under equal incident power conditions on the sample: since there are no filters between the sample and the detector, all the available fluorescence signal can be collected without losses. Moreover, excitation spectra can be particularly useful for multitarget imaging: the use of a number of fluorophores to label different targets (e.g., subcellular organelles) is limited by the width of probe fluorescence spectra. This issue can be addressed through excitation-resolved microscopy: differences in excitation spectra may be exploited to image multiple targets simultaneously.

The most common technique to measure an excitation spectrum consists in scanning the excitation wavelength while collecting fluorescence emission in a fixed detection passband. This can be done using a monochromator or a tunable filter along the excitation path. Rather than one spectral band at a time, a temporal approach allows one to investigate a continuous spectral range: all the wavelengths of a broadband source impinge on the sample simultaneously while being processed with an interferometer; a Fourier transform then retrieves the excitation spectrum from the fluorescence signal measured at each step of the scan.

Previous works presented two types of excitation-resolved imaging systems: (1) a point-scanning microscope based on a Michelson's interferometer [47], (2) a widefield microscope with a tunable filter for excitation wavelength selection [21], [34]. In this work we present a further upgrade of our widefield hyperspectral microscope such that also excitation-resolved measurements can be performed with the TWINS interferometer in the illumination path. Further optimisation would be necessary to make this instrument competitive,

but we still have obtained some results that prove its potentialities.

This thesis is structured in five main parts. Chapters 1 and 2 provide a theoretical background about spectral imaging, in particular the Fourier transform approach based on the common-path birefringent interferometer TWINS. Chapter 3 gives an overview of the available techniques for fluorescence emission, excitation and Raman spectroscopy. Chapter 4 describes the multimodal microscope with particular attention to the excitation path. Finally, Chapter 5 presents some measurements, including tests to validate the new implementation of the system.

1 | Chapter 1- Fourier transform spectroscopy

This Chapter provides a description of the available techniques for hyperspectral imaging, based on either dispersive or Fourier transform spectrometers. Particular attention is given to the latter, which is the technique developed in this thesis.

1.1. Principles of hyperspectral imaging

Spectral imaging is a powerful technique that combines spectroscopy and imaging, obtaining a rich dataset that contains a series of images of the same object captured at different wavelengths: spectral features are then investigated for each object point. In particular, if a continuous electromagnetic spectrum is retrieved for each pixel of the image we can talk about *hyperspectral imaging (HSI)*, otherwise, the technique is called *multispectral imaging*, when the spectrum is measured in discrete limited bands, rather than continuously.

Spectral imaging can be used in various applications, since it allows quick sample identification and analysis: microscopy, for both biological [58] or material science [6] samples, remote sensing, with airborne and spaceborne cameras [11], [26], cultural heritage [25], just to mention a few examples.

Any imaging technique requires a sensor: it generates a certain electrical signal, either voltage or current, related to the amount of incident photons that are properly detected; in most cases, the resulting image can be monochrome or a red-green-blue (RGB), thus it is represented respectively by a single matrix with NxM pixels, or three matrices one for each colour R,G,B. In spectral imaging, the result of a measurement is a more complex *hypercube*: it is a 3D dataset with two spatial coordinates (NxM pixels) and one spectral coordinate (wavelengths for each pixel).

It is then evident that the great advantage of richness of information comes along with much higher complexity of the resulting dataset that has to be processed, therefore algorithms have been developed to extract both spectral and spatial features of the object/scene under analysis (among them *k-means* [86], *N-FINDR* [99], *PCA* [53], *MCR*

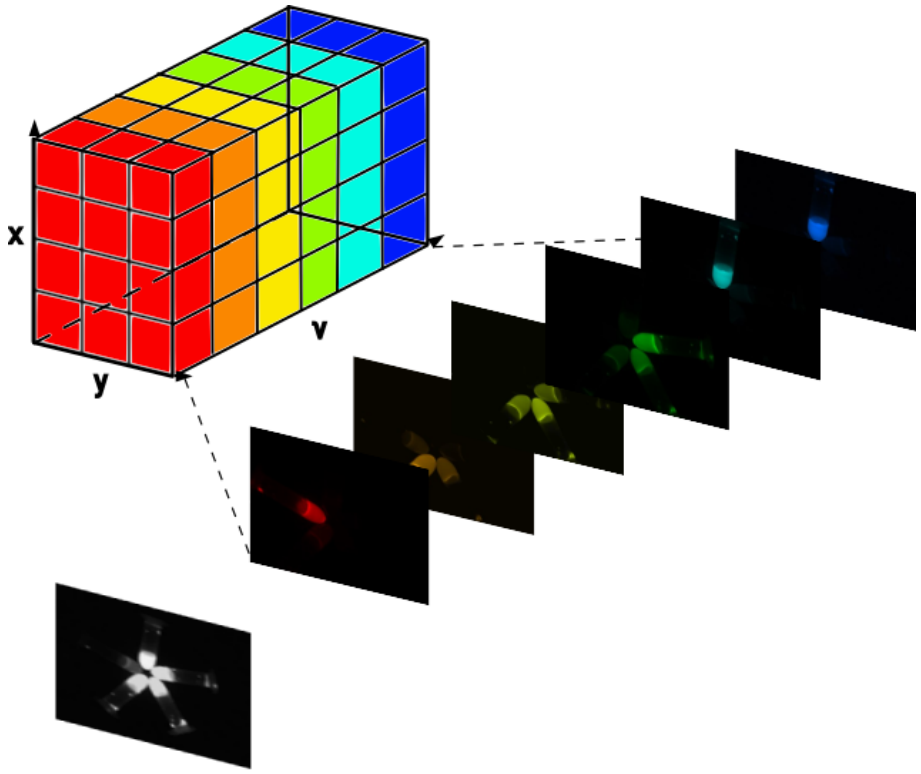

Figure 1.1: Spectral image dataset (hypercube). The spectral image is described as an intensity $I(x, y, \nu)$; it can be viewed either as an image $I(x, y)$ at each frequency ν (vertical slicing) or as a spectrum $I(\nu)$ at every pixel (x, y) (horizontal slicing).

[28], *SVD* [92] are the most common).

The most basic representation of the results of a hyperspectral measurement are the following rendering methods::

- a true-colour (RGB) image is obtained from the superposition of the three R,G,B matrices; they are derived from the dataset by integrating the product of the spectrum for each pixel with the spectral responsivities for the three colours, respectively;
- in a false-colour representation spectral sensitivity curves are shifted in different wavelength ranges; for example, one of the most common approaches in satellite images of the Earth centers the red spectral response in the near infrared (IR) range;
- in a pseudo-colour image colours are associated with values of a variable in order to enhance the visual interpretation with respect to a grayscale; some typical applications are thermal imaging, medical diagnostic and remote sensing.

Each representation allows one to highlight certain properties of the image, thus the choice is driven by the specific field of application.

Different strategies are available to obtain such a 3D dataset (x,y, spatial coordinates, and ν, frequency) [38], [43]:

1. **wavelength-scan** method measures the image one wavelength at a time: all light is collected at the same time and filtered with a tunable filter (commonly based on liquid crystals or acousto-optic modulators), that sends to the 2D sensor only a precise wavelength component (actually, a narrow range centered at a certain frequency; the narrower, the better spectral discrimination capability);

2. **spatial-scan** method measures the whole spectrum of a portion of the image at a time and then scans the image. There are two possible scanning strategies: in *point scan* (*whisk-broom*) light is collected only from one point at a time and dispersed onto a linear detector array; in *line scan* (*push-broom*) the whole image is acquired line-by-line since light is collected from one line of points and dispersed onto a 2D sensor with gratings or prisms;

3. **snapshot** method collects all light at the same time and an array of prisms/gratings disperses it toward a 2D detector array; it enables the acquisition of a complete spectral data cube in a single integration, generating images directly from the areas of interest;

4. **time-scan** method measures a set of images and retrieves spectral information only after acquisition through mathematical tools (e.g. Fourier transform, Hadamard transform).

They can be classified in *widefield imaging* techniques, when all the scene is imaged at once (1, 3, 4), and *raster-scanning* techniques (2), which require more acquisitions to retrieve the whole field of view (FOV). The second category suffers from longer measurement times than snapshot approach, in case of large objects, and the same problem arises for wavelength-scan methods when a lot of wavelengths are analysed (in other words, it is practical only when a few narrow spectral bands are needed).

Another criterion of classification is based on the type of information directly measured in each frame: (1, 2, 3) are *frequency-domain* techniques since each pixel of the detector measures an intensity for a fixed wavelength; on the other hand, a *time-domain* technique (4) gains access to spectral information only after the whole measurement since the intensity in each pixel is not directly related to a specific wavelength, but it is the result of a superposition of all spectral components. The first rely on filters or dispersive elements, such as prisms or gratings, that are able to select wavelengths (precisely, narrow spectral bandwidths). The latter requires an interferometer (in case of Fourier transform

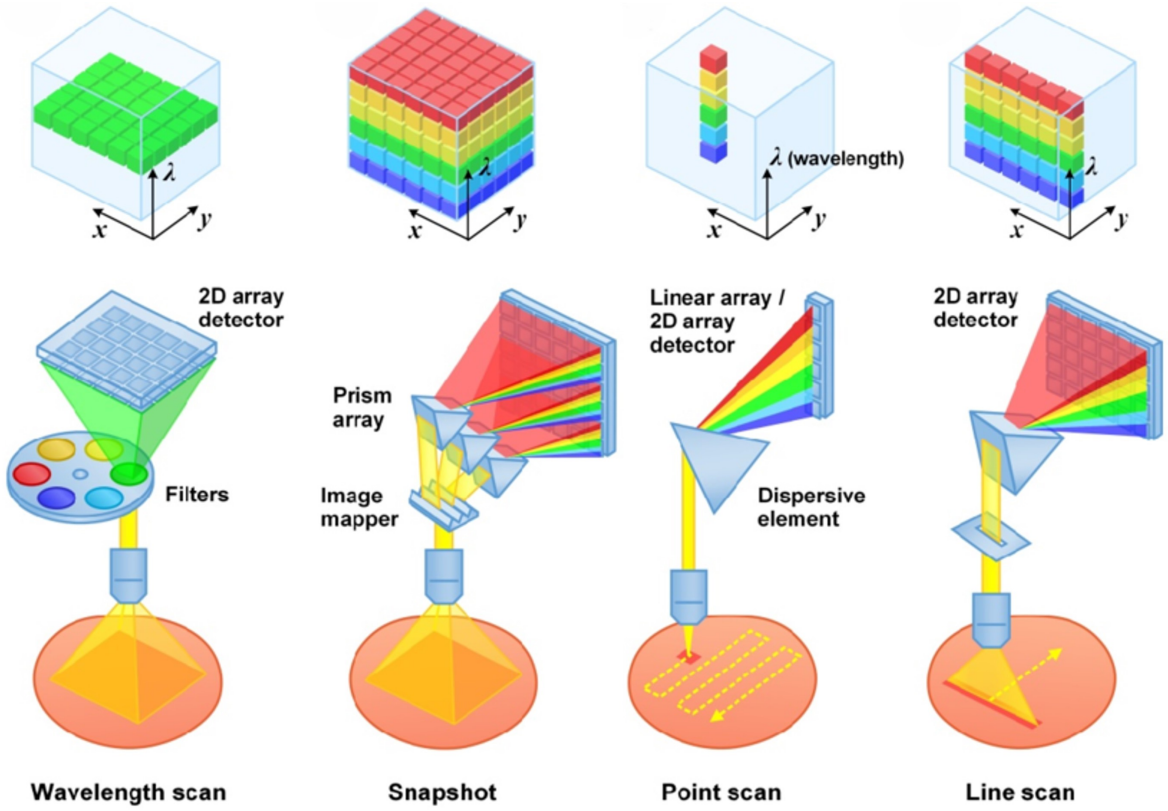

Figure 1.2: Various methods for spectral imaging in frequency domain. *Image adapted from [95].*

spectroscopy) or a spatial light modulator (for Hadamard transform spectroscopy) placed either in front of the detector or immediately after the illumination source.

Among these approaches we focus on time-domain FT detection: it brings in some relevant advantages with respect to frequency-domain techniques, known as Fellgett's, Jacquinot's and Connes' advantages, that will be discussed in 1.2.3.

1.2. Fourier transform spectroscopy

The basic concepts for Fourier transform spectroscopy [10] are interferometry and Fourier transform theory. It properly came into play in 1950s, but Fizeau, Focault, Michelson and Rubens had paved the way many years before [22]. The most famous contribution came from Albert Abraham Michelson [62], [63]: his interferometer (that earned him the Nobel Prize in 1907 *"For his optical precision instruments and the spectroscopic and metrological investigations carried out with their aid"*) is still widely used in many applications, such as in Fourier transform for infrared (FTIR) spectroscopy [42], while it has been replaced in other contexts by birefringent common path interferometers, due to their better insen-

sitivity to vibrations and compactness [9], [77].

Since the working principle is the same, we discuss it in detail referring to the original implementation of Michelson's interferometer and then generalise it to birefringent interferometers in Chapter 2.

1.2.1. Wiener Kintchine's theorem

The original implementation consists of a light beam impinging on a 50:50 beam splitter: light is split into two replicas travelling along two arms, one fixed and the other with variable length, delimited by plane mirrors; after reflection, the two replicas of the radiation (E_r, reference field, and E_d, delayed field) recombine and their interference pattern, called *interferogram*, is detected by a sensor (S).

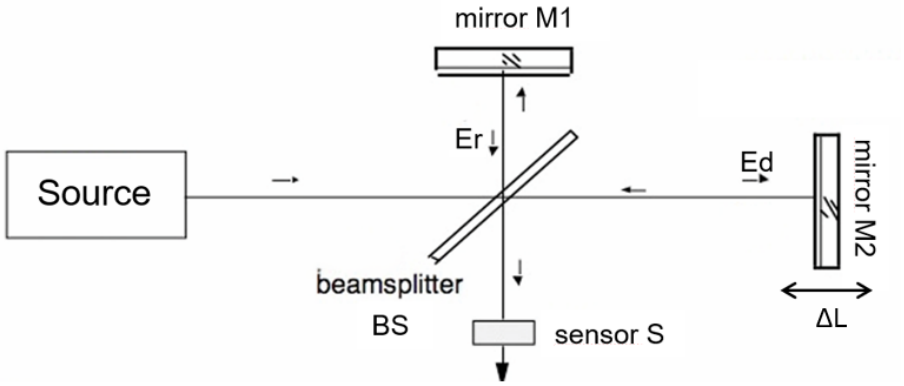

Figure 1.3: Michelson interferometer: radiation is divided into two identical replicas, E_r and E_d, that recombine and interfere at the detector plane; interference conditions are obtained by changing the moveable mirror (M2) position (ΔL is the difference between arms lengths).

Considering a displacement ΔL in the variable arm (with respect to the balanced condition, i.e., arms of equal length), the delay accumulated between the replicas is $\tau = \frac{2*\Delta L}{c}$; the total field at the detector is the superposition of the two, $E_r = E(t)$ and $E_d = E(t-\tau)$:

$$E_{tot} = E(t) + E(t-\tau) \tag{1.1}$$

whose intensity [41, Chapter 9] is

$$U(t,\tau) = \frac{1}{2}\epsilon v \mid E_{tot} \mid^2 \propto \mid E_{tot} \mid^2 = \mid E(t) \mid^2 + \mid E(t-\tau) \mid^2 + [E(t)^* E(t-\tau)] + c.c. \tag{1.2}$$

with ϵ dielectric constant, v speed of light in the medium, the symbol * indicates the complex conjugate of the field E. We recall that in complex notation the electric field has

amplitude and phase term:

$$E(t) = A(t)\ e^{-i2\pi\nu_0 t} \tag{1.3}$$

with ν_0 central frequency; if the amplitude has not got any temporal dependence, the radiation is monochromatic.

Using a slow, time-averaging detector the total time-integrated intensity (i.e., the energy) is recorded as a function of delay τ: the resulting interferogram is

$$I(\tau) \propto \int_{t_0}^{t_1} |\ E(t)\ |^2\ dt + \int_{t_0}^{t_1} |\ E(t-\tau)\ |^2\ dt + \left[\ \int_{t_0}^{t_1} E(t)^*\ E(t-\tau)\, dt + c.c\ \right] = \\ = 2\ C(\tau = 0) + [C(\tau) + c.c.] \tag{1.4}$$

having defined the *field autocorrelation* as

$$C(\tau) \equiv \int_{t_0}^{t_1} E(t)^*\ E(t-\tau)\, dt \tag{1.5}$$

where $t_0 = -\infty, t_1 = +\infty$, in the ideal case of an infinite measurement.

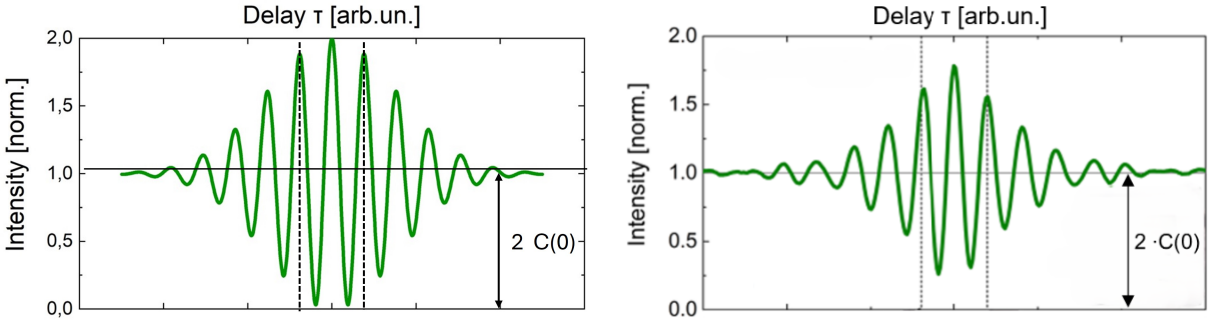

(a) Ideal interferogram (b) Measured interferogram

Figure 1.4: Example of ideal and measured interferograms: an oscillating term is superimposed on the constant $2{\cdot}C(0)$, but in (b) peak intensity is not $4{\cdot}C(0)$ and the function is not perfectly symmetric about zero delay, as happens in the ideal case (a).

Defining the Fourier transform of the field E(t) as

$$\tilde{E}(\nu) = FT(E(t)) \equiv \int_{-\infty}^{+\infty} E(t)\ e^{i2\pi\nu t}\, dt \tag{1.6}$$

the interferogram can also be written in the spectral domain for Parseval's theorem [48]

$$I(\tau) \propto \int |\ E_{tot}(t,\tau)\ |^2\ dt = \int |\ \tilde{E}_{tot}(\nu,\tau)\ |^2\ d\nu = \int |\ \tilde{E}(\nu) + \tilde{E}(\nu)\ e^{i2\pi\nu\tau}\ |^2\ d\nu \tag{1.7}$$

In Equation 1.4 we can distinguish two terms: $2 \cdot C(0)$ is constant and represents the average energy; C(τ) is oscillating (oscillations are referred to as *fringes* of the interferogram) and represents the field autocorrelation. Performing the Fourier transform of the delay-dependent term, it is possible to retrieve the power spectral density of the electric field for Wiener-Kintchine's theorem [98]:

$$S(\nu) \equiv \mid \tilde{E}(\nu) \mid^2 = FT(C(\tau)) = \int_{-\infty}^{+\infty} C(\tau)\, e^{i2\pi\nu\tau} d\tau \tag{1.8}$$

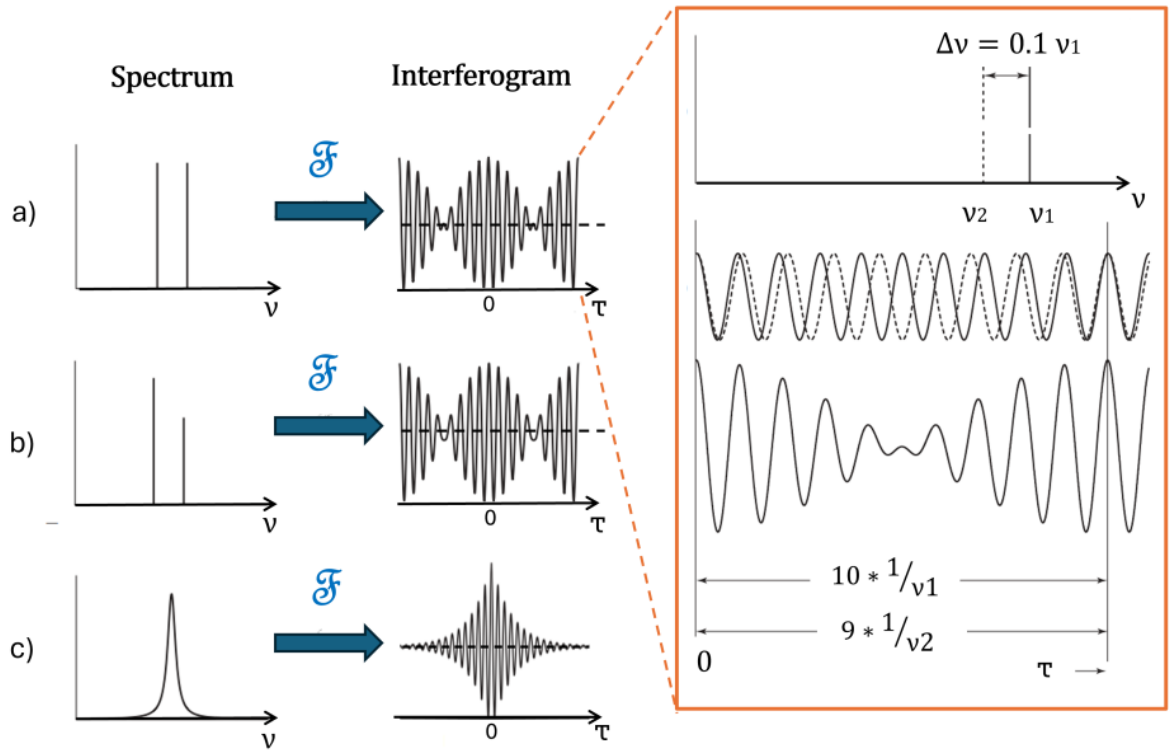

Figure 1.5: Examples of spectra and corresponding interferograms: two infinitesimally narrow lines of equal (a) and unequal (b) intensity; (c) Lorentzian shape, which gives a cosinusoidal interferogram with exponential decay of the envelope (the broader the lineshape, the faster the decay). *Image adapted from [42].*

Hence, the FT approach naturally retrieves a spectrum that is a function of frequency; on the other hand, a grating-based dispersive spectrometer measures a wavelength-dependent intensity. For this reason, in Chapter 5 we will represent measured spectra with an abscissa axis uniform in frequency.

Intuitively: each spectral component, $E(t) = Ae^{-i2\pi\nu t}$ with constant A, produces its own cosinusoidal interferogram

$$I(\tau) \propto 2 \mid A \mid^2 + 2 \mid A \mid^2 \cos(2\pi\nu\tau) \tag{1.9}$$

with same frequency ν. A generic radiation is the superposition of monochromatic components, therefore its interferogram results to be the superposition of cosinusoidal intensity patterns. Fourier analysis then gives access to the weight for each wavelength. Since the informative content is the oscillating part of the interferogram, whose transform gives the spectrum, a relevant parameter for the quality of the measurement is the *visibility* or *fringe contrast* defined as follows:

$$V \equiv \frac{I(0) - I_{ave}}{I_{ave}} = \frac{I_{max} - I_{min}}{I_{max} + I_{min}} \tag{1.10}$$

with $I_{ave} = 2 \cdot C(\tau = 0)$ and the maximum (optimal) achievable value is $V = 1$ (as in Figure 1.4a for the ideal interferogram).

It is interesting to note that the two replicas of the field can interfere giving the interferogram only when they are polarized along a common direction. This happens for both highly coherent (monochromatic) radiation and incoherent sources, provided that temporal coherence [90, Chapter 1] is always kept between the two replicas irrespective of the coherence of the source.

1.2.2. Management of data: from experimental interferogram to spectrum

In practice, the general method to retrieve the spectrum of a given source consists in:

1. measuring the intensity modulation $I(\tau)$ as a function of the delay introduced at each motor position, $\tau = \tau(x)$;

2. subtracting the average intensity 2 $C(\tau = 0)$ to extrapolate only the oscillating behaviour of the interferogram, $C(\tau)$, that is its informative part;

3. computing the Fourier transform to retrieve the spectrum of the radiation.

Sampling

The temporal integral that appears in Equation 1.8 implies an infinitesimal sampling step $d\tau$ for the interferogram, but this cannot be the case in a real measurement. Discrete sampling raises the problem of the adequate sampling step: *Nyquist-Shannon criterion* [71] states that an analog signal can be digitized without aliasing error, if and only if the sampling rate is greater than or equal to twice the highest frequency component ν_{max} in a given signal; only in this condition it is possible to reconstruct the original waveform unambiguously, otherwise spectral features would appear at incorrect frequencies.

Actually, this rule is strictly true when the spectrum extends from zero to ν_{max}; a lower sampling frequency can be employed when the bandwidth also has a lower bound, ν_{min}: it is the so-called *undersampling* [42].

Apodization

In practice it is not possible to measure the interferogram for an infinite time, i.e., to scan the delay τ infinitely, as specified in Equation 1.8 where integral limits are infinite. Mathematically, this means multiplying the ideally infinite interferogram $C(\tau)$ by a rectangular (boxcar) function so as to obtain a limited realistic interferogram $C_{apod}(\tau)$.

The consequences of this approach can be understood in the simplest case of a single infinitely narrow line light: its interferogram is an infinite cosinusoidal function, but only a certain delay range $[-T, T]$ is effectively scanned. In mathematical terms, it is equivalent to multiply the complete interferogram by a rectangular function with non-zero values in the interval $[-T, T]$

$$C_{apod}(\tau) = C(\tau) \cdot A(\tau) = C(\tau) \cdot rect(\frac{\tau}{2T}) \tag{1.11}$$

with $C(\tau)$ oscillating term of the interferogram $I(\tau)$ and

$$rect(\frac{\tau}{2T}) = \begin{cases} 1 & if \quad -T < \tau < T \\ 0 & if \quad |\tau| > T \end{cases} \tag{1.12}$$

For the properties of the Fourier transform [40, Chapter 6], the spectrum results from the convolution of the transforms of the two functions: delta functions are replaced by sinc functions with a finite full-width at half maximum (FWHM) and sidelobes

$$S(\nu) = FT(C_{apod}(\tau)) = FT(C(\tau)) * FT(rect(\frac{\tau}{2T})) = FT(C(\tau)) * 2Tsinc(2\pi\nu T) \tag{1.13}$$

The sinc function is called the *instrumental lineshape*, *ILS*, because it represents the effect of the measurement process of an ideal delta function. It is then possible to define the concept of *spectral resolution*, i.e., the minimum spectral separation $\Delta\nu$ between instrumental lineshapes associated with a monochromatic source. One possible criterion is based on FWHM: two lineshapes are distinguishable when their distance is equal to the FWHM (for a sinc function $\Delta\nu = FWHM = \frac{0.605}{T}$, as calculated in [42, Chapter 2]). Another possibility (popular in grating spectrometers) is Rayleigh criterion [13, Chapter 7]: two lineshapes are resolved when the peak of the first falls in the first zero of the second. The two criteria give quite interchangeable values.

False sidelobes represent the main issue with the rectangular truncation. If the boxcar is replaced with a different function, called *apodizing* function, their amplitude can be reduced significantly: this mathematical procedure is called *apodization*. From Equation 1.13 it is clear that spectral resolution cannot be univocally determined for an FT spectrometer, since it depends on the apodizing function: according to the required resolution and acceptable sidelobes amplitude, different apodizing functions can be chosen (conceptually any function that has a value of unity at zero displacement and decreases with increasing retardation can serve for this purpose). An example is the triangular truncation, which offers lower sidelobes but a broader peak compared to the boxcar; this can be advantageous when dealing with low spectral peaks that otherwise might be overwhelmed by sidelobes. Several studies were carried out on apodizing functions: Filler [36] investigated trigonometric functions; Norton and Beer [70] studied deeply the properties of a family of functions with the general form $A(\tau) = \sum_{i=0}^{n} c_i[1-(\frac{\tau}{T})^2]^i$; Gaussian, supergaussian, Blackman and Happ-Genzel functions are also frequently used. For our purposes, we will apply the Happ-Genzel apodizing window since it is a good compromise between spectral broadening and sidelobes suppression.

It is worth noting that spectral resolution only depends on the total scan allowed by the interferometer. Typically a double-sided scan of the interferogram is preferred for an improvement in photometric accuracy and higher signal-to-noise ratio with respect to a single-sided acquisition [19].

We may conclude that the maximum scan length is always preferable because it leads to the best achievable resolution; nevertheless, another factor has to be considered: signal-to-noise ratio [80]. A spectral feature with $\Delta\nu$ width gives an interferogram of finite duration $\sim \frac{1}{\Delta\nu}$; if the measurement lasts T and only signal-independent noise is present (this hypothesis will be commented on in Section 1.2.3), the square-root-noise is always proportional to $T^{\frac{1}{2}}$, while the signal either increases as a function of T, when T$\ll \frac{1}{\Delta\nu}$, or is constant, when the scan takes much longer time than the interferogram duration, because the oscillations are already damped. This implies two opposite trends in SNR: in

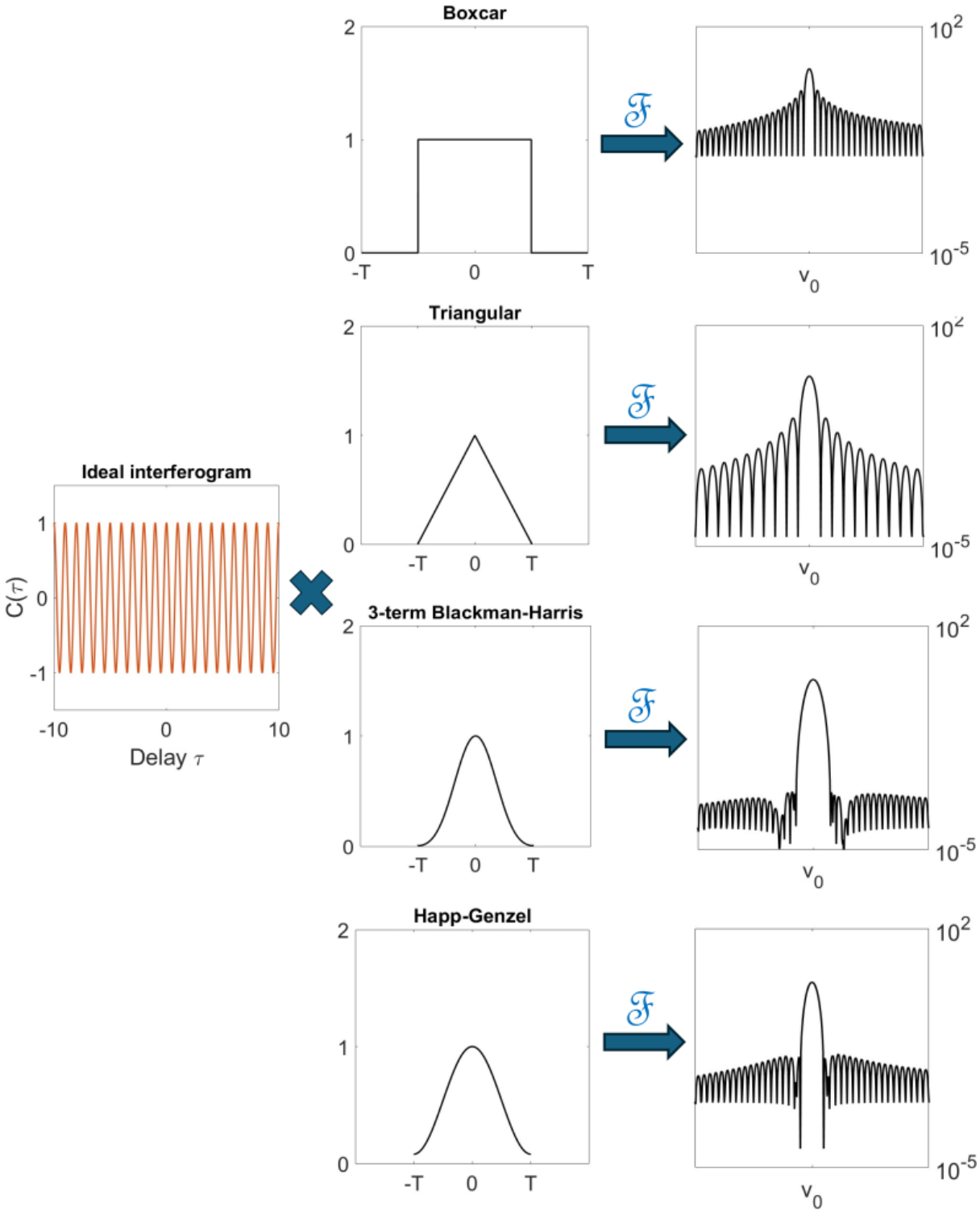

Figure 1.6: Common apodizing functions and corresponding lineshape of the spectrum for perfectly monochromatic radiation at frequency ν_0. Ideally the spectrum has a delta centered at ν_0, but in practice there are both spectral broadening and appearence of sidelobes, that strongly depend on the type of apodizing function.

the first case, it increases as $T^{\frac{1}{2}}$ and it decreases by the same factor in the latter. Scan duration is then the compromise between spectral resolution and SNR.

Fourier transform algorithm

Fourier transform spectroscopy would not have developed without an efficient algorithm for Fourier transform calculation.

A.A. Michelson was the first who recognized the potential of interferometry to analyze light spectrum: at first he performed by hand the Fourier analysis needed to determine the spectral components of different sources, but soon he needed to make the interferogram analysis much less laborious; he invented and built himself what he called *harmonic analyzer* [45], [64]. However, the computational power provided by that analog machine was not sufficient to carry out a deep and precise analysis of spectra, thus the effective birth of FT spectroscopy can be dated to 1950s when electronic amplifiers had become commonplace in physics laboratories and general-purpose digital computers began spreading. In this way, computational power increased considerably; in particular, the major step in Fourier transform calculation was the introduction of *fast Fourier transform (FFT)* algorithm by J.W. Cooley and J.W. Tukey in 1965: in [23] they demonstrated that, to compute a complex Fourier series with N terms, the number of required operations is $N \log N$ rather than N^2; therefore this algorithm is one of the most efficient methods to compute the discrete Fourier transform of a discretely sampled interferogram.

However, FFT cannot be used in practice since it works only for equispaced data, while a real interferogram is sampled at non-perfectly equispaced points (this is due to non-idealities in delay control): we have to perform the *non-uniform discrete Fourier transform*. MATLAB implementation of this algorithm is described in [32], but we will follow a different approach, since it shows better performances in terms of computational time (see Chapter 2).

Phase correction

Ideally, an interferogram is an even function, i.e., it is symmetric about zero delay position, $\tau = 0$; we will call this position *zero path delay (ZPD)*. However, noise and sampling effects always make the interferogram asymmetric in practice. The Fourier transform of a symmetric function is real

$$S_{ideal} = FT(C_{ideal}(\tau)) = |S_{ideal}(\nu)| \tag{1.14}$$

but this does not necessarily hold in presence of asymmetries; hence the spectrum computed by transforming the interferogram is complex

$$S_{real} = FT(C(\tau)) = |S_{real}(\nu)| \quad e^{i\phi(\nu)} \tag{1.15}$$

To retrieve a real spectrum as physical observable, a phase correction must be applied: for each frequency component ν, the phase $\phi(\nu)$ can be computed as $arctan(\frac{\Im(S_{real})}{\Re(S_{real})})$; then

$$|S_{real}| = S_{real} \quad e^{-i\phi} \tag{1.16}$$

Precisely, the measured interferogram can be written as

$$C(\tau) = C_{ideal}(\tau - \tau_{shift}) + n(\tau) \tag{1.17}$$

with temporal shift τ_{shift} with respect to the zero delay (assuming a rigid translation of the temporal axis of the interferogram) and noise $n(\tau)$. Therefore

$$S_{real} = S_{ideal}(\nu) \quad e^{i2\pi\nu\tau_{shift}} + N(\nu) \quad e^{i\phi_n(\nu)} \tag{1.18}$$

$$\sim \begin{cases} S_{ideal}(\nu) \quad e^{i2\pi\nu\tau_{shift}} & if \quad S_{ideal}(\nu) \gg N(\nu) \\ N(\nu) \quad e^{i\phi_n(\nu)} & if \quad S_{ideal}(\nu) \ll N(\nu) \end{cases} \tag{1.19}$$

where $S_{ideal}(\nu)$ and $N(\nu)$ are real. It follows that a linear correction phase $\phi = 2\pi\nu\tau_{shift}$ is computed from the complex spectrum only when signal prevails on noise, obtaining S_{ideal} after correction. The retrieved spectrum is the ideal one only when the noise contribution is much less intense than the signal. This phase correction method was developed by Mertz [61]; a second approach referred to as Forman method is mathematically equivalent to the first but performed in the interferogram domain [37].

1.2.3. Advantages of FT spectroscopy

As already mentioned, there are three main advantages that FT spectroscopy holds over dispersive spectrometers [10, Chapter 2].

Jacquinot's (or throughput) advantage *Throughput* (or *etendue*) for an infinitesimal source (receiver) of area dA that emits (receives) in an infinitesimal solid angle $d\Omega$ is defined as

$$dE \equiv dA_{\perp} d\Omega \tag{1.20}$$

where $dA_\perp$ represents the area dA projected along the sight direction forming a certain angle θ with the normal to dA itself. In lossless media etendue is conserved: stops and apertures of an optical system do not affect this quantity.
In a dispersive grating-based spectrometer the resolving power is proportional to the number of grooves illuminated on the surface of the grating; it is also determined by the entrance slit width: the narrower the slit, the better the resolution [73, Chapter 2]. However, the slit also determines the throughput of the optical system by blocking some percentage of the incident optical power (the narrower the slit, the less optical power available to the spectrometer, the longer the measurement time).

On the contrary, in FT spectroscopy resolution is not determined by an entrance slit, but it depends on the scan duration: since there is not the tight limitation on the amount of light accepted by the instrument, the throughput results to be higher than for a spectrometer.

Fellgett's (or multiplex) advantage An interferometer receives information from the entire range of a given spectrum during each time element of a scan, whereas a conventional dispersive spectrometer receives information from only the very narrow spectral range which lies within the exit slit of the instrument.

Assume that the measured spectrum contains M narrow spectral bands $\delta\nu$, measurement lasts T and noise is random and signal-independent: for each $\delta\nu$

- signal is proportional to observation time (this is strictly valid only when observation time is shorter or comparable to the interferogram duration, as discussed in Section 1.2.2), that is T for the interferometer and $\frac{T}{M}$ for a dispersive spectrometer;
- (random) noise is proportional to the square root of integration time;

therefore signal-to-noise ratio (SNR) ends up to be higher by a factor $M^{\frac{1}{2}}$ for an FT spectrometer with respect to a dispersive one

$$\frac{SNR_{FT}}{SNR_{dispersive}} = \frac{\frac{1}{T^{1/2}}}{\frac{1}{(T/M)^{1/2}}} = M^{1/2} \tag{1.21}$$

It is relevant to note that this advantage is lost in the case of signal-dependent noise, since SNR ends up being the same for both cases. This mainly happens in visible and ultraviolet ranges because detectors are much better than in the infrared: since individual photons can be detected, the noise is now governed by the statistical fluctuations in the number of photons emitted by the source during a measurement period.

Connes' advantage (or wavelength accuracy) High absolute frequency accuracy is achievable thanks to the possibility of calibrating the interferometer with known laser lines; furthermore, this procedure does not require to be repeated. On the contrary, dispersive instruments utilize a mechanically complex prism or grating which cause errors in peak positions and inaccuracies from scan to scan [88].

Furthermore, some other relevant features of FT spectroscopy can be mentioned:

- flexibility in spectral resolution, since it depends on the maximum achievable scan delay (the longer the scan, the better the resolution);
- broad wavelength coverage, only limited by detector spectral responsivity and optical elements transparency.

2 | Chapter 2- TWINS interferometer

In this Chapter we present our common-path birefringent interferometer TWINS, which enables FT spectroscopy: we describe its working principle, its coupling to an imaging system (camera and microscope) to acquire a temporal hypercube and the management of the 3D dataset to retrieve the spectral content for each pixel of the field of view.

2.1. Working principle

The main limitation of a double-beam interferometer (as Michelson's interferometer) is that field replicas travel along different paths, that may undergo different perturbations (vibrations, instabilities) from the environment, making stabilization a complex problem to deal with (bulky and costly feedback loops are typically employed). This is the reason why these instruments are mainly used in IR range, since shorter visible wavelengths would require higher stability (of the order of $\frac{\lambda}{10} \sim 50nm$).

A solution consists in the common-path birefringent interferometer, *TWINS*, presented for the first time in [14]: replicas, generated from a polarized radiation by means of a birefringent crystal, travel collinearly, thus any perturbation along the path is shared between them, leading to very high stability and reproducibility (the relative delay accuracy is of the order of a few attoseconds).

When light, either pulsed or continuous wave (CW), propagates in a uniaxial birefringent material, ordinary and extraordinary polarizations travel with different phase velocities ($v_{p,o}$ and $v_{p,e}$, respectively), thus accumulating a relative delay proportional to the propagation length; the optical path difference (and so the delay) can be tuned by varying the material thickness. To achieve this result: light crosses a polarizer (P1) with axis rotated by 45° with respect to the optical axis of the crystals, such that two identical field components, along x and y, are generated; a first birefringent plate (A), with fixed thickness L and optical axis orthogonal to light propagation direction, introduces a

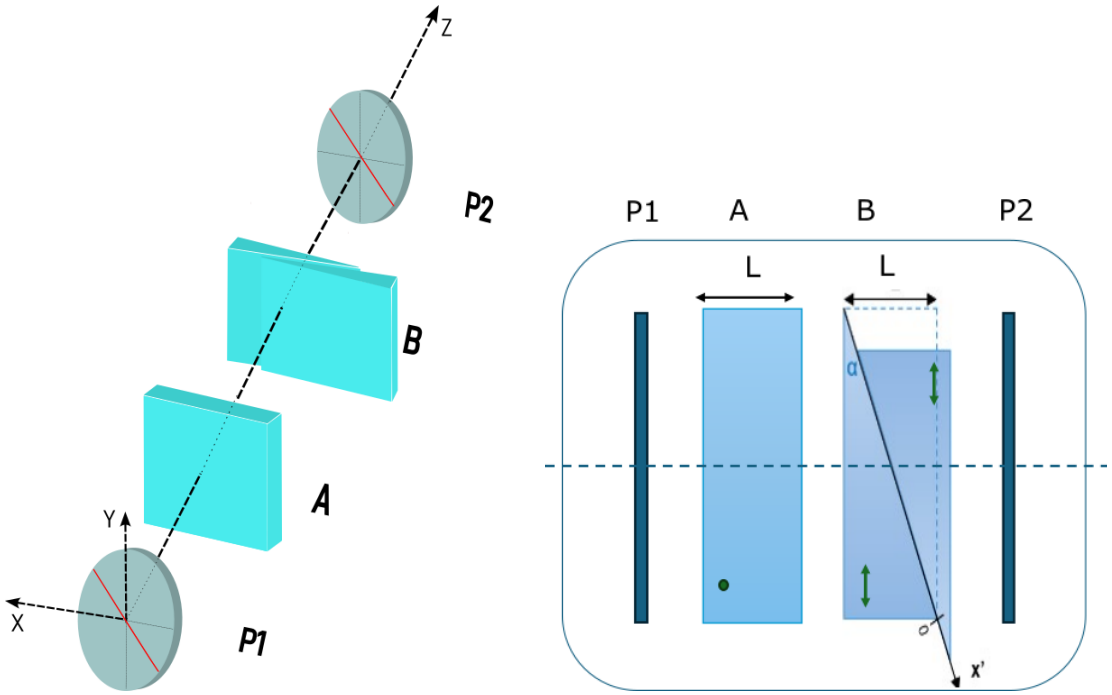

(a) (b)

Figure 2.1: Basic scheme of the TWINS interferometer (a) and top-view (b): P1, P2 polarizers; A,B birefringent blocks (plate and wedges) where green circle and green double arrow represent the orientation of the optical axes, respectively; the dashed-dotted line is the main axis of the optical system.

constant delay

$$\tau_{plate} = \tau_{xp} - \tau_{yp} = \frac{L}{v_{p,o}} - \frac{L}{v_{p,e}} = \frac{L}{\frac{c}{n_o}} - \frac{L}{\frac{c}{n_e}} \tag{2.1}$$

A second birefringent slab (B) with total thickness L is cut into two wedges, translating along their common hypotenuse: saying x' the apex coordinate of one of the two, along this direction, the introduced delay is now proportional to wedge position

$$\tau_{wedges} = \tau_{xw} - \tau_{yw} = \frac{L + x' \sin\alpha}{v_{p,e}} - \frac{L + x' \sin\alpha}{v_{p,o}} = \frac{L + x' \sin\alpha}{\frac{c}{n_e}} - \frac{L + x' \sin\alpha}{\frac{c}{n_o}} \tag{2.2}$$

obtaining an overall delay

$$\tau = \frac{x' \sin\alpha \quad (n_e - n_o)}{c} \tag{2.3}$$

where the material birefringence $\Delta n \equiv n_e - n_o$ is a function of frequency ν; Sellmeier's equations [13, Chapter 2] are typically used to express the wavelength-dependent refractive index of a transparent optical material: $n(\lambda)^2 = 1 + \sum_j \frac{A_j \lambda^2}{\lambda^2 - B_j}$. With a translator stage applied to the wedges it is then possible to tune the relative delay between replicas propagating in ordinary and extraordinary directions, similarly to Michelson's interferom-

eter mirror motion. Finally, a second polarizer P2 (with axis either parallel or orthogonal to the first one) projects the two replicas to a common linear polarization such that they can interfere.

We can highlight two main differences with respect to a Michelson's interferometer:

- the spectrum is retrieved through the Fourier transform of the interferogram after constant value subtraction

$$S(\nu) = \int_{-\infty}^{+\infty} C(\tau) e^{i2\pi\nu\tau} d\tau \tag{2.4}$$

With formula 2.3 the interferogram can be expressed as a function of wedge position x'

$$I(x') = \int_{-\infty}^{+\infty} \mid \tilde{E}(\nu) + \tilde{E}(\nu) \cdot e^{i2\pi\nu \frac{x' \sin\alpha\,(n_e - n_o)}{c}} \mid^2 \, d\nu \tag{2.5}$$

Then the spectrum becomes

$$S(f_x) = \int_{-\infty}^{+\infty} C(x') e^{i2\pi\nu \frac{x' \sin\alpha \Delta n(\nu)}{c}} dx' \tag{2.6}$$

with *pseudofrequency* (or *spatial frequency*)

$$f_x = \frac{\nu \, \sin\alpha \, \Delta n(\nu)}{c} \tag{2.7}$$

that is not a linear function of the optical frequency ν, as would happen for a Michelson's interferometer, due to the frequency-dependent birefringence $\Delta n(\nu)$. The procedure that associates the two quantities f_x and ν is called *spectral calibration* and will be described in detail in Chapter 4.

- the rate of delay variation with respect to mechanical displacement becomes

$$\frac{d\tau}{dx'} = \frac{\sin\alpha \Delta n}{c} \tag{2.8}$$

This value is much lower than for a Michelson's interferometer where

$$\frac{d\tau}{dx} = \frac{2}{c} \tag{2.9}$$

(with x displacement of the moveable mirror, equivalent to ΔL in Figure 1.3) since both $\sin\alpha$ and Δn are lower than the unity. This represents an advantage: the same displacement is related to a smaller variation of the delay between replicas, allowing a finer delay adjustment and better stability.

2.2. Imaging with the TWINS

Together with the advantages of FT spectroscopy presented in Chapter 1, the TWINS interferometer resulted to be suitable for parallel recording of spectra for all pixels of a 2D sensor, because it does not require a complex implementation as for dispersive or other FT spectrometers. For this reason, it was coupled to different imaging systems to perform FT spectral imaging.

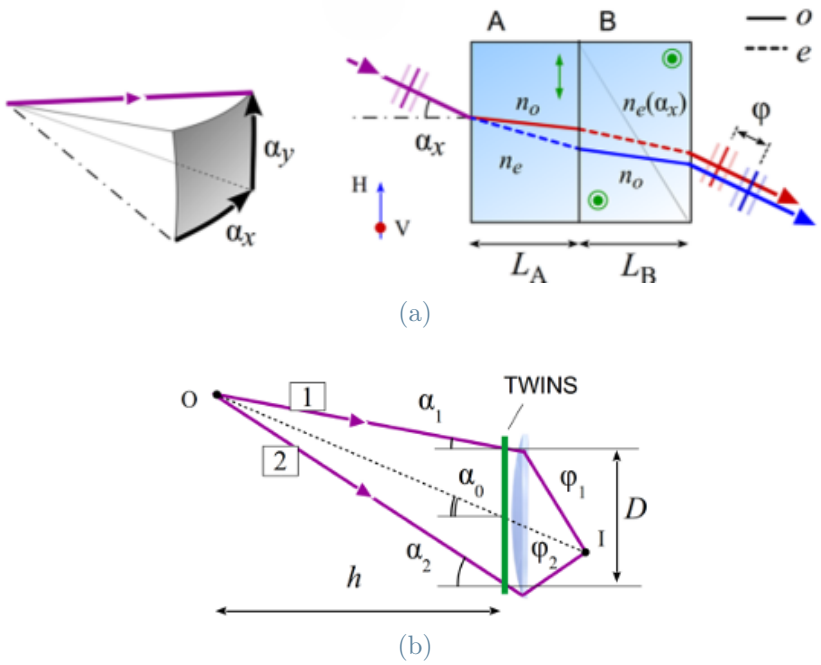

Figure 2.2: (a) Optical paths for vertically and horizontally polarized components (red and blue respectively) through the TWINS for a generic incident angle α. (b) Schematic representation of an imaging system with the TWINS: the two marginal rays (1 and 2) propagate from the source point O to the image point I accumulating different phase shifts ϕ_1, ϕ_2. *Images from [17], [77].*

A generic imaging system (represented synthetically as a lens in Figure 2.2b) captures the image of a scene on the detector plane. If the TWINS is placed in front of the imaging system, two replicas of the radiation from all the object points within the FOV are generated with tunable delay, therefore an interferogram (and then a spectrum) can be measured in all pixels of the detector. The requirement for the system is then maintaining the coherence, i.e., similar path delay, among the rays of the bundle from an object point O, since their superposition gives the interferogram in the image point I on the detector plane.

To study this configuration more in detail it is interesting to follow the pencil of rays

propagating from the object point O through the imaging system.

Consider a generic angle α_x (α_y) in the horizontal x-z plane (vertical y-z plane) formed between a ray and the normal to the surface of the birefringent material (in Figure 2.2a it is represented as a pair of plates with orthogonal optical axes and lengths L_A and L_B). Birefringence causes a separation of the two orthogonal components of the ray: they travel slightly different geometrical paths inside the material, thus different optical phases are accumulated even when the nominal delay τ (computed for normal incidence) is set to zero ($x' = 0$ in Figure 2.1b), i.e., when $L_A = L_B = L$.

To understand the consequences on the interferogram in I, we can compute the total resulting field due to the bundle of rays at frequency ν coming from the point object O: a bundle is identified by an *average angle* α_0 (same reasoning for angles in x-z or y-z planes) formed by the chief ray and an *angle range* $\Delta\alpha$ that describes the displacement with respect to α_0. Equivalently, we can refer to the additional phase shift ϕ_{add} introduced between the two replicas that is associated with a specific angle of incidence α, obtaining a univocal bundle identification through $[\phi_0, \Delta\phi]$. It follows that the total phase shift for each ray of the bundle is

$$\phi = 2\pi\nu\tau + \phi_0 + \delta\phi = 2\pi\nu\tau + \phi_{add} \tag{2.10}$$

where τ is the delay controlled by wedge position, $\delta\phi$ the shift from ϕ_0, then ϕ_{add} the additional phase shift due to non-normal incidence.

The total field at I is the result of superposition of fields for each ray of the bundle: if the external rays form respectively $\alpha_1 = \alpha_0 + \Delta\alpha_1$ and $\alpha_2 = \alpha_0 + \Delta\alpha_2$ with the normal, phase shift varies from $\phi_1 = \phi_0 + \Delta\phi_1$ to $\phi_2 = \phi_0 + \Delta\phi_2$, thus the total field for the bundle $[\alpha_0, \Delta\alpha]$ is

$$\begin{aligned} E_{[\alpha 0, \Delta\alpha]} &= \int_{\phi_1}^{\phi_2} \left(E(2\pi\nu t) + E(2\pi\nu t + 2\pi\nu\tau + \phi_{add})\right) d\phi_{add} = \\ &= \int_{\phi_1}^{\phi_2} \left(Ae^{-i2\pi\nu t} + Ae^{-i(2\pi\nu t + 2\pi\nu\tau + \phi_{add})}\right) d\phi_{add} \end{aligned}$$

using the previously-mentioned complex notation $E = Ae^{-i2\pi\nu t}$ for the single replica (always assuming same amplitude A for the two polarization directions).

The interferogram turns out to be

$$I(\tau) \propto \int_{t_1}^{t_2} \left| \int_{\phi_1}^{\phi_2} (Ae^{-i(2\pi\nu t)} + Ae^{-i(2\pi\nu t + 2\pi\nu\tau + \phi_{add})}) d\phi_{add} \right|^2 dt$$
$$= |A|^2 (t_2 - t_1) \left| (\Delta\phi_2 - \Delta\phi_1) + ie^{-i(2\pi\nu\tau + \phi_0)} \left(e^{-i\Delta\phi_2} - e^{-i\Delta\phi_1}\right) \right|^2 \tag{2.11}$$

With precise calculations one can derive maxima and minima for I(τ) as functions of the variable phase shift $\Delta\phi = \Delta\phi_2 - \Delta\phi_1$. Recalling the definition of *visibility* (*fringe contrast*)

$$V = \frac{\Delta_I}{I_{ave}} = \frac{I_{max} - I_{min}}{I_{max} + I_{min}} \tag{2.12}$$

we can plot $V(\Delta\phi)$ to understand how it is affected by the range of phases introduced for the rays of a bundle due to non-normal incidence on the crystal.

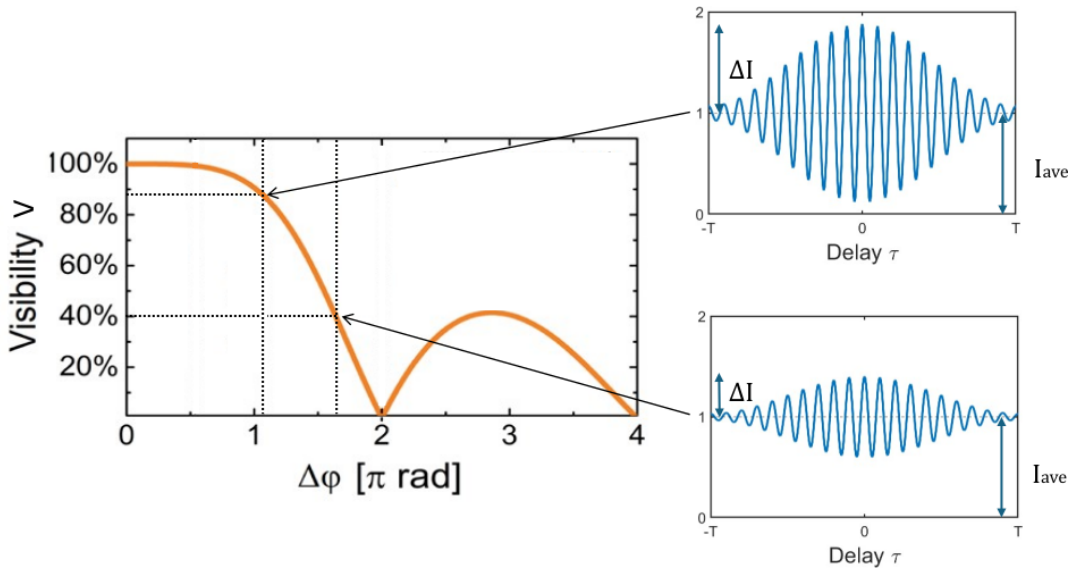

Figure 2.3: Visibility V of the interferogram of a monochromatic radiation as a function of the phase spread $\Delta\phi$ between marginal rays of the considered bundle across the TWINS. The inserts show two interferograms with different values of visibility. *Image adapted from [77].*

It is possible to precisely relate the phase shift ϕ_{add} to the incidence angle α_0, as reported in [77] for specific working conditions of the interferometer. Since $\Delta\phi \sim \frac{\partial\phi_{add}}{\partial\alpha_0} \cdot \Delta\alpha$, larger values of $\Delta\phi$ are obtained (1) where the slope of the curve $\phi_{add}(\alpha_0)$ is the steepest, i.e. at the edge of the field of view (this is intuitive because the average incident angle α_0 is larger for a bundle of rays from an object point far from the optical axis, thus the additional phase shift ϕ_{add} is higher), and (2) for large values of $\Delta\alpha$, i.e. when the

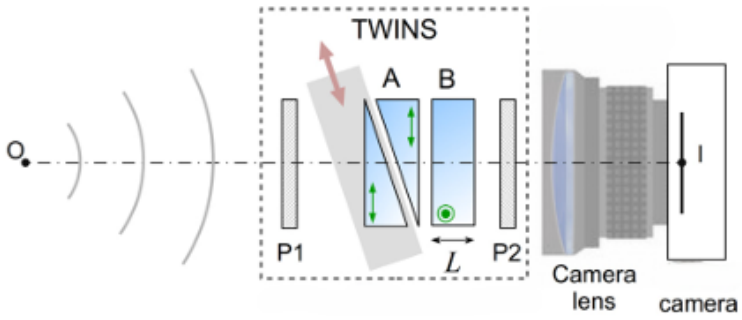

(a) Hyperspectral camera

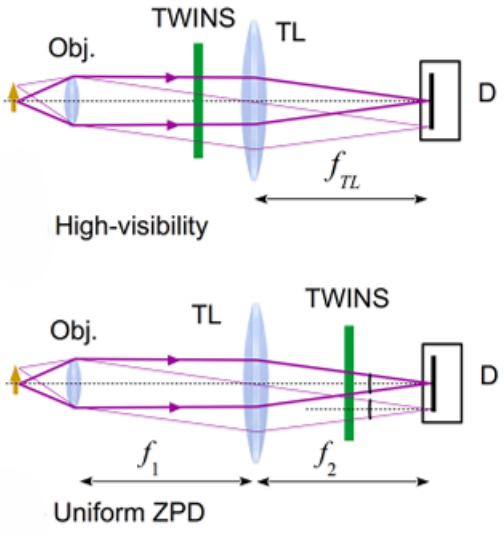

(b) Hyperspectral microscope.

Figure 2.4: Main imaging schemes developed with the TWINS intereferometer: (a) hyperspectral camera; (b) two possible configurations for a microscope. *Images from [77], [17].*

object is close to the camera lens according to

$$\Delta\alpha = |\alpha_1 - \alpha_2| \sim arctan\frac{D/h}{1 + tan^2\alpha_0} \tag{2.13}$$

where D is the dimension of the TWINS (that represents the aperture stop of the system) and h the distance of an object point from the camera (Figure 2.2b).

So far we have considered a scheme with the TWINS in front of the imaging system (lenses and camera); however, depending on the position of the interferometer with respect to the object plane and camera sensor, light rays can form different angles with the normal to the interferometer itself:

- in a hyperspectral camera [77] rays coming from the scene form a plethora of angles, i.e., various α_0 and $\Delta\alpha$; this results in the almost hyperbolic spatial pattern of the

accumulated phase shift ϕ_{add} typical of uniaxial crystals [13, Chapter 14]);

- in a hyperspectral microscope [17] two other configurations have been implemented: ***high fringe visibility (HFV)***, where bundles of parallel rays impinge with different angles (different α_0, but same $\Delta\alpha = 0$), and ***uniform-ZPD***, with an average angle $\alpha_0 = 0$ across the FOV.

Since this thesis focuses on the TWINS applications in microscopy, we will analyse the latter in detail.

Firstly, we recall the optical scheme of a microscope. As shown in Figure 2.4b, two lenses, objective and tube lens, create the image I of an object point O; precisely, the object is placed in the front focal plane of the objective; the second lens then intercepts bundles of parallel rays and focuses them in points of its back focal plane. The object undergoes a magnification $M = \frac{f_{tube}}{f_{obj}}$ (with f_{tube} and f_{obj} focal lengths for tube and objective, respectively) and the diffraction limit of the imaging system is $\frac{\lambda}{2NA}$, where the numerical aperture (NA) is defined as $n \cdot \sin\theta$, with n refractive index of the surrounding medium and θ the angle subtended by the objective lens from an on-axis object point [60, Chapter 1]. An interesting property of this system is telecentricity [13, Chapter 4]: microscope objectives typically have a diaphragm in their back focal plane that acts as the aperture stop; this means that the entrance pupil is at infinity and the system is said to be *telecentric in the object space*. When this diaphragm is at focal distance from the tube lens, also the exit pupil is at infinity, therefore the system results to be *telecentric* also *in the image space*. Two important properties follow: (1) a longitudinal shift in the object position results in a blurring without any change in image size, i.e., magnification remains a constant independent of defocus; (2) NA is constant over the entire field of view.

We can now study how TWINS can be placed with respect to the microscope scheme:

- if it is between objective and tube lens, all the rays from one object point are parallel when entering the interferometer, i.e., they all propagate at the same angle α_0, with $\Delta\alpha = 0$. This implies that the maximum contrast is achieved in all image points (from here the origin of the name *high fringe visibility*), but since different object points have bundles that form different angles α_0 with the interferometer, total delay τ varies along the FOV with object position, giving an almost hyperbolic phase pattern;

- if it is between the tube lens and the detector, provided that $f_1 = f_2$ in Figure 2.4b such that the system is telecentric in the image space, bundles from each object point impinge on the wedges with null average angle ($\alpha_0 = 0$, $\Delta\alpha \neq 0$). This implies a

uniformity of the delay across the FOV, that can be useful when unconventional sampling strategies are adopted (e.g., spectral compressive sampling [17]), at the cost of a lower fringe contrast due to the plethora of angles $\Delta\alpha$ for rays of the same bundle.

2.3. Management of dataset

Fourier transform algorithm

As already discussed, the interferogram for each pixel p of the image is sampled at discrete motor positions, therefore the spectral hypercube is retrieved from the temporal one through a discrete FT. Since samples are not equally spaced, a fundamental condition for the FFT is not satisfied, thus non-uniform discrete FT becomes more appropriate.

We will not exploit the existing MATLAB algorithm (*nufft*), but a different matrix implementation, since simulations demonstrated shorter execution time.
In real measurements interferograms are sampled in discrete points, $\{\tau\}_{real} = (\tau_1, \tau_2, ..., \tau_n)$, within a finite temporal window, therefore Equation 1.8 can be rewritten as

$$S_{real,p}(\nu) = \sum_{\tau \in \{\tau\}_{real}} C_{apod,p}(\tau)\, e^{i2\pi\nu\tau} \Delta\tau \tag{2.14}$$

Defining a set of frequencies $\{\nu\}_{real}$ and the differential $\{\Delta\tau\}_{real}$ respectively

$$\begin{gathered} \{\nu\}_{real} = (\nu_1, \nu_2, ..., \nu_{m-1}, \nu_m) \\ \{\Delta\tau\}_{real} = (\Delta\tau_1, \Delta\tau_2, ..., \Delta\tau_{n-1}, \Delta\tau_n) \equiv (\tau_2 - \tau_1, \tau_3 - \tau_2, \quad ..., \tau_n - \tau_{n-1}, \tau_n - \tau_{n-1}) \end{gathered} \tag{2.15}$$

It is possible to compute the spectrum for the p-th pixel as

$$\begin{pmatrix} S_{real,p}(\nu_1) \\ S_{real,p}(\nu_2) \\ \vdots \\ S_{real,p}(\nu_m) \end{pmatrix}^T = \begin{pmatrix} C_{apod,p}(\tau_1)\Delta\tau_1 \\ C_{apod,p}(\tau_2)\Delta\tau_2 \\ \vdots \\ C_{apod,p}(\tau_n)\Delta\tau_n \end{pmatrix}^T \cdot \begin{pmatrix} e^{i2\pi\nu_1\tau_1} & e^{i2\pi\nu_2\tau_1} & ... & e^{i2\pi\nu_m\tau_1} \\ e^{i2\pi\nu_1\tau_2} & e^{i2\pi\nu_2\tau_2} & ... & e^{i2\pi\nu_m\tau_2} \\ \vdots & \vdots & \vdots & \vdots \\ e^{i2\pi\nu_1\tau_n} & e^{i2\pi\nu_2\tau_n} & ... & e^{i2\pi\nu_m\tau_n} \end{pmatrix} \tag{2.16}$$

Since the matrix with exponential terms is the same for all pixels of the image, it is sufficient to calculate it once and then use it to compute the spectrum for each point, thus dramatically reducing the calculation time.

Analysis of spectral hypercube

The computed spectra are complex because any real interferogram is asymmetric about zero delay due to errors in motor positions (that translate into incorrect delays $\{\tau\}_{real}$) and noise that perturbs the measurement. Moreover, there is a temporal shift τ_{shift} related to the angle α between the rays crossing the TWINS and optical axis: even with an ideally symmetric interferogram, this shift of its temporal axis from ZPD introduces a phase term.

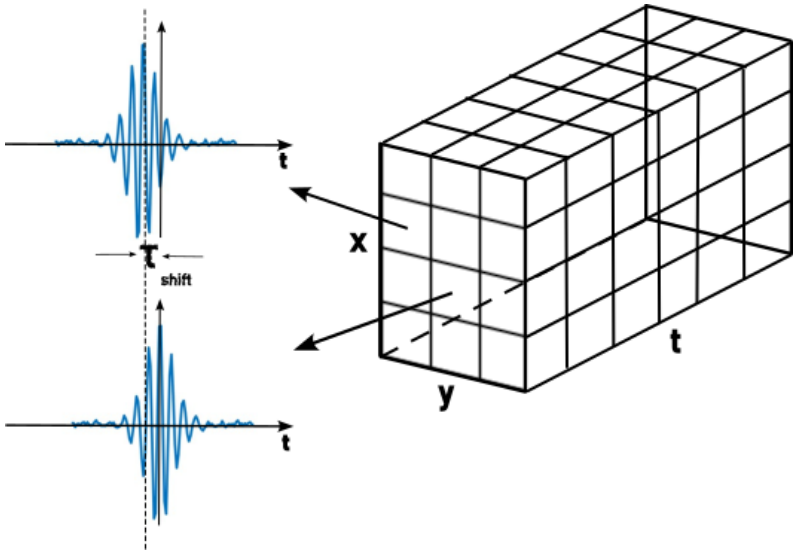

Figure 2.5: The measured dataset is a temporal hypercube with interferograms for each pixel of the FOV. Two real interferograms are represented: in this example the intensity at the origin of temporal axis is not the same for two different pixels, due to a shift τ_{shift} in ZPD.

Recalling the generic form of the computed complex spectrum

$$S_{real} = S_{ideal}(\nu) \quad e^{i2\pi\nu\tau_{shift}} + N(\nu) \quad e^{i\phi_n(\nu)} = |S_{real}|e^{i\phi(\nu)} \tag{2.17}$$

$$\sim \begin{cases} S_{ideal}(\nu) \quad e^{i2\pi\nu\tau_{shift}} & if \quad S_{ideal}(\nu) \gg N(\nu) \\ N(\nu) \quad e^{i\phi_n(\nu)} & if \quad S_{ideal}(\nu) \ll N(\nu) \end{cases} \tag{2.18}$$

For phase correction it is possible to apply Mertz method (see Chapter 1), which consists in multiplying S_{real} by the term $e^{-i\phi_{fit}(\nu)}$, where ϕ_{fit} is the linear fit of the phase $2\pi\nu\tau_{shift}$ (a good approach to retrieve it is based on considering only spectral peaks since $S_{real} \sim S_{ideal}(\nu) \quad e^{i2\pi\nu\tau_{shift}}$). Once the spectrum is corrected, its phase is almost zero for peaks,

while it can assume different values for noise spikes

$$S_{corr} = S_{real}e^{-i\phi_{fit}} \sim \begin{cases} S_{ideal}(\nu) & if \quad S_{ideal}(\nu) \gg N(\nu) \\ N(\nu) \quad e^{i\phi_n(\nu)}e^{-i\phi_{fit}} & if \quad S_{ideal}(\nu) \ll N(\nu) \end{cases} \tag{2.19}$$

In a hyperspectral image, when dealing with more pixels in a region of interest (ROI), we can retrieve the mean spectrum across the region by taking the real part of the corrected spectrum for each pixel and averaging over all the pixels: for a significant component of the spectrum (ν_1 such that $S_{ideal}(\nu_1) \gg N(\nu_1)$), it results in a sum of positive real quantities $S_{ideal}(\nu_1)$; for a noisy component (ν_2 such that $S_{ideal}(\nu_2) \ll N(\nu_2)$) the real part of S_{corr} can be either positive or negative, therefore the average over a multitude of pixels is almost zero.

A similar approach is taking directly the absolute value of the computed complex spectrum: for spectral peaks $|S_{real}| \sim S_{ideal}$, otherwise $|S_{real}| \sim |N|$. Following the same idea as before, when dealing with more pixels, we could think of averaging the spectra absolute values. However, it is better to compute the absolute value of the mean of the complex spectra to cancel out noise, because the average of all positive values $|N(\nu)|$ for different pixels is always positive and higher than the absolute value of the average of both positive and negative values, for real and imaginary parts in complex spectra.

An explicative pictorial view of the problem is Gauss plane. Assume that ν_2 is referred to a noise component of the spectrum and ν_1 to a significant peak; S(ν) in a pixel can be represented as a point in this plane: points associated with all the pixels fall around the origin when ν_2 is considered, since their phase is random, otherwise they concentrate around a point with phase $2\pi\nu_1\tau_{shift}$ and absolute value S_{ideal}. It is then clear that this second method for phase correction holds for a hyperspectral image when interferograms have the same τ_{shift} in the FOV, because points in the Gauss plane need to share the same phase $2\pi\nu\tau_{shift}$ (when there is a spectral peak at frequency ν) to take advantage of the complex mean. This happens only in the uniform-ZPD configuration, while in all the other cases we must rely on Mertz method or work directly with the absolute value of spectra and average it.

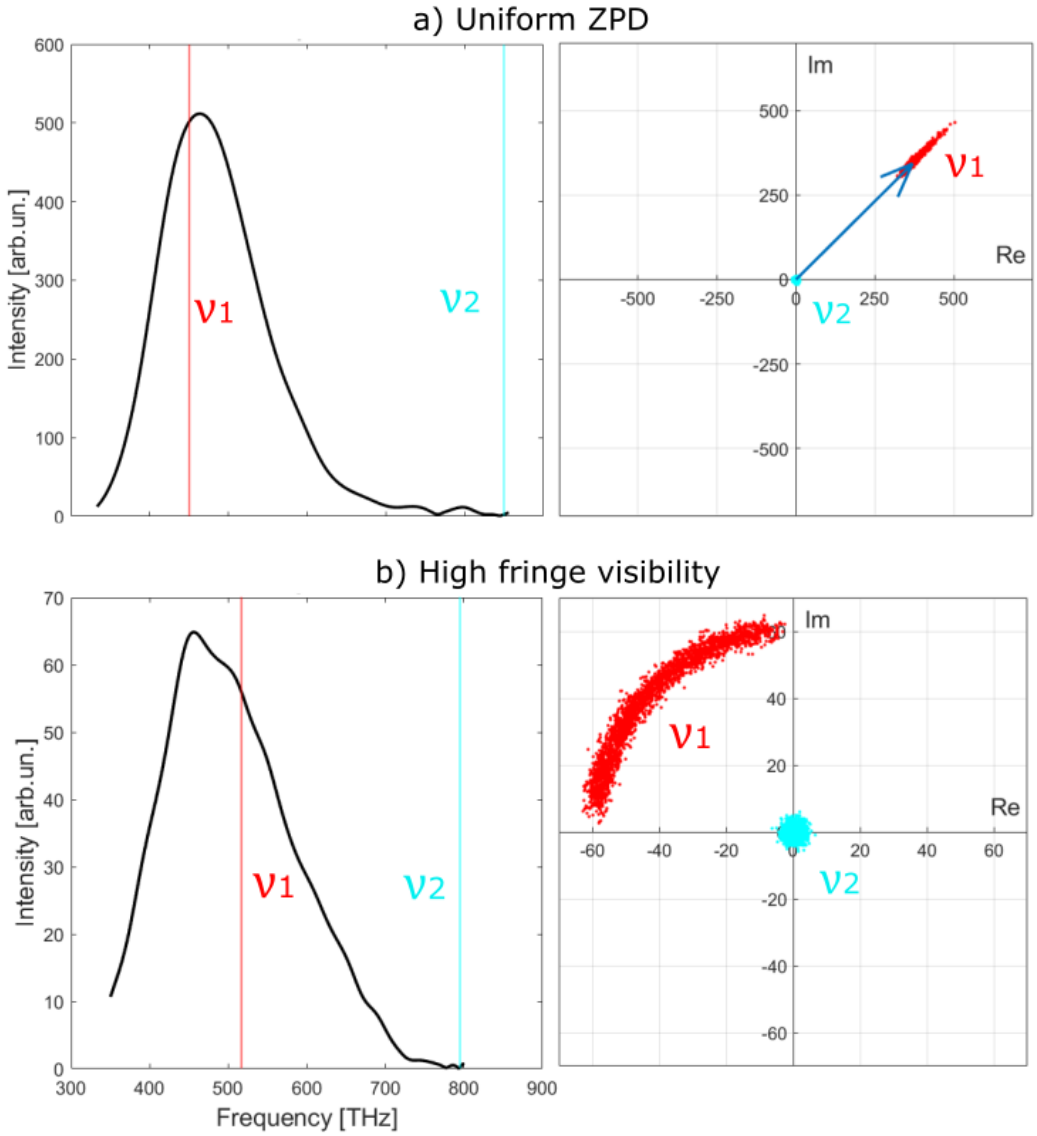

Figure 2.6: On the left, the average spectrum for a ROI of 50x50 pixels is shown, with a peak frequency, ν_1, and a noise component, ν_2. On the right, each component is represented in the Gauss plane for all the considered pixels. As expected, the noise component has a random phase for different pixels, thus they create a cloud of points about the origin. The significant frequency is associated with the same linear phase $2\pi\tau_{shift}\nu_1$ for all pixels in (a); on the contrary, phase shift τ_{shift} varies across the FOV in (b), therefore points show a phase that spans a wider range.

3 | Chapter 3- Basics of light-matter interaction

This Chapter aims to give an overview of the physical origin of various spectra that can be measured in a sample: fluorescence emission and excitation spectra in Section 3.1 and Raman signal in Section 3.2. In both cases we also report the principal experimental techniques available to perform these measurements.

3.1. Fluorescence spectroscopy

Considering a generic molecular system: *Perrin-Jablonski*'s diagram [56, Chapter 1] is a schematic representation of energy states and radiative and non-radiative transitions that can occur after photoexcitation.

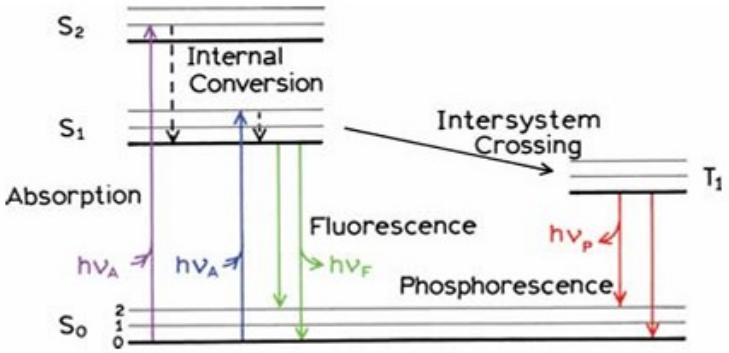

Figure 3.1: Perrin-Jablonsky's diagram. Bold lines represent the lowest vibrational level of each electronic state, with the higher vibrational levels represented by thinner lines. Electronic states are labeled according to the total spin angular momentum, i.e., **S** for singlet states with zero total spin and **T** for triplet states with angular momentum of one. Arrows describe the different mechanisms of transitions among energy states. *Image from [56].*

Absorption consists in a transition from a lower to a higher energy level of the system. If vibrational levels of the same electronic state are involved we can talk about *IR absorption*, since infrared radiation is absorbed; while *electronic absorption* between different electronic energy levels takes place in presence of higher energy radiation.

A transition from the singlet ground-state to a higher energy electronic state (still singlet for momentum conservation rule) takes place when the final state wavefunction has a good overlap with the initial one (Franck-Condon principle, [7, Chapter 11]). Photon energy is translated into internal energy very rapidly ($\sim 10^{-15}s$), i.e., the internuclear distance does not change immediately (transition is said to be *vertical*). The system then relaxes to the lowest vibrational level of the reached excited electronic state ($\sim 10^{-12}s$) with a vibrational relaxation called *internal conversion*.

Different mechanisms can then occur:

- radiative decay, *fluorescence* (green arrows), to electronic ground-state, typically to an excited vibrational level, that relaxes rapidly. Since fluorescence emission results from the lowest vibrational level of S_1 (or S_2), even when higher vibrational levels are reached after absorption, its spectrum is red-shifted with respect to the absorption one (*Stokes' shift*) and different excitation wavelengths lead to the same emission spectrum (*Kasha's rule*);

- non-radiative decay to same spin electronic ground-state;

- non-radiative decay to a different spin electronic state (triplet state), called *intersystem crossing*. Since the transition to a singlet state (red arrows) is now forbidden for selection rules, this state lifetime is much longer, resulting in a lower emission rate constant (*phosporescence*).

In presence of more than one molecular species even more complex processes may take place:

- *quenching* is a reduction of the fluorescence intensity due to an energy transfer from an excited molecule to another one in solution called *quencher*, i.e., the first returns to ground-state without emitting any photon;

- *photobleaching* consists in a reduction of the number of molecules available for fluorescence. This happens mainly: (1) when a triplet state is reached after intersystem crossing, since the long state lifetime increases the probability for these molecules to react with different coexisting ones; (2) for photochemical reactions that involve directly the excited molecule and other environmental compounds. In both cases the result is a non-fluorescent molecule;

- *Förster resonance energy transfer (FRET)*, occurs when energy is transferred from one excited molecule, called *donor*, to another one, called *acceptor*. Specifically, when the molecules are well separated and the incident light is energetic enough

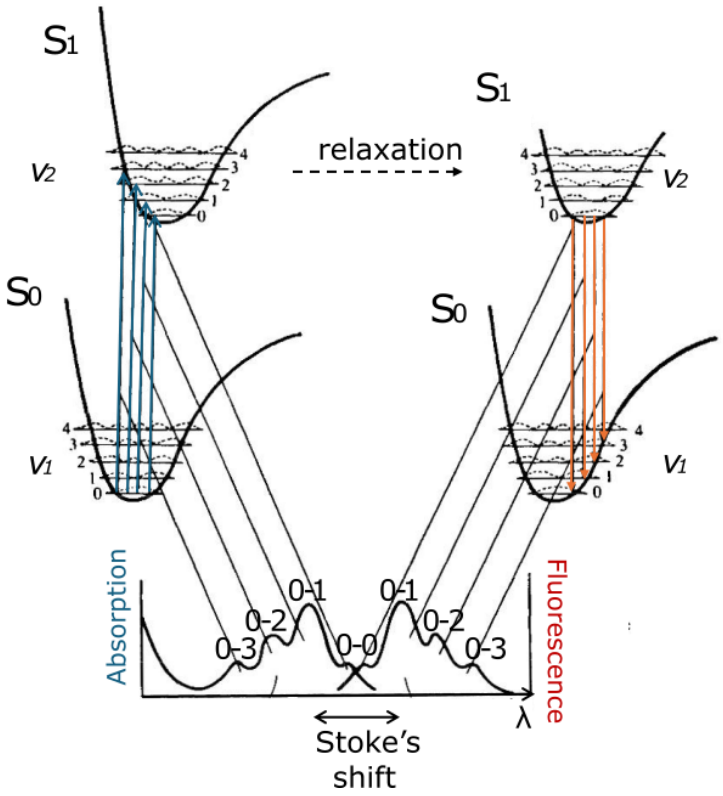

Figure 3.2: Potential energy curves for ground (S_0) and exicted (S_1) electronic states. Quantum numbers v_1 and v_2 indicate vibrational levels for ground and excited electronic states respectively. Dotted lines represent vibrational probability functions: a transition (blue and orange arrows) is more probable when there is a good overlap between functions of initial and final state (Franck-Condon principle). This probability translates in intensity of the absorption or emission spectrum.

to excite the molecule with the higher energy gap, the donor absorbs the light and subsequently emits. Otherwise, if the molecules are in close proximity, energy transfer occurs between their excited states, resulting in emission from the acceptor. This mechanism is specifically referred to as *resonant energy transfer* because there is not any intermediate photon, i.e., it does not involve the emission of a photon from the donor that is going to be absorbed by the acceptor, but donor and acceptor are coupled by a dipole-dipole interaction.

The rate of energy transfer depends not only on the donor-acceptor distance, but also upon the spectral overlap of the donor emission and acceptor absorption spectra and the relative orientation of the molecules dipoles.

Energy levels of a system can be inferred by fluorescence spectroscopy which consists in the spectral characterization of excitation and emission spectra of materials.
It can be divided into two categories:

- in (fluorescence) emission spectroscopy the excitation wavelength is kept fixed and

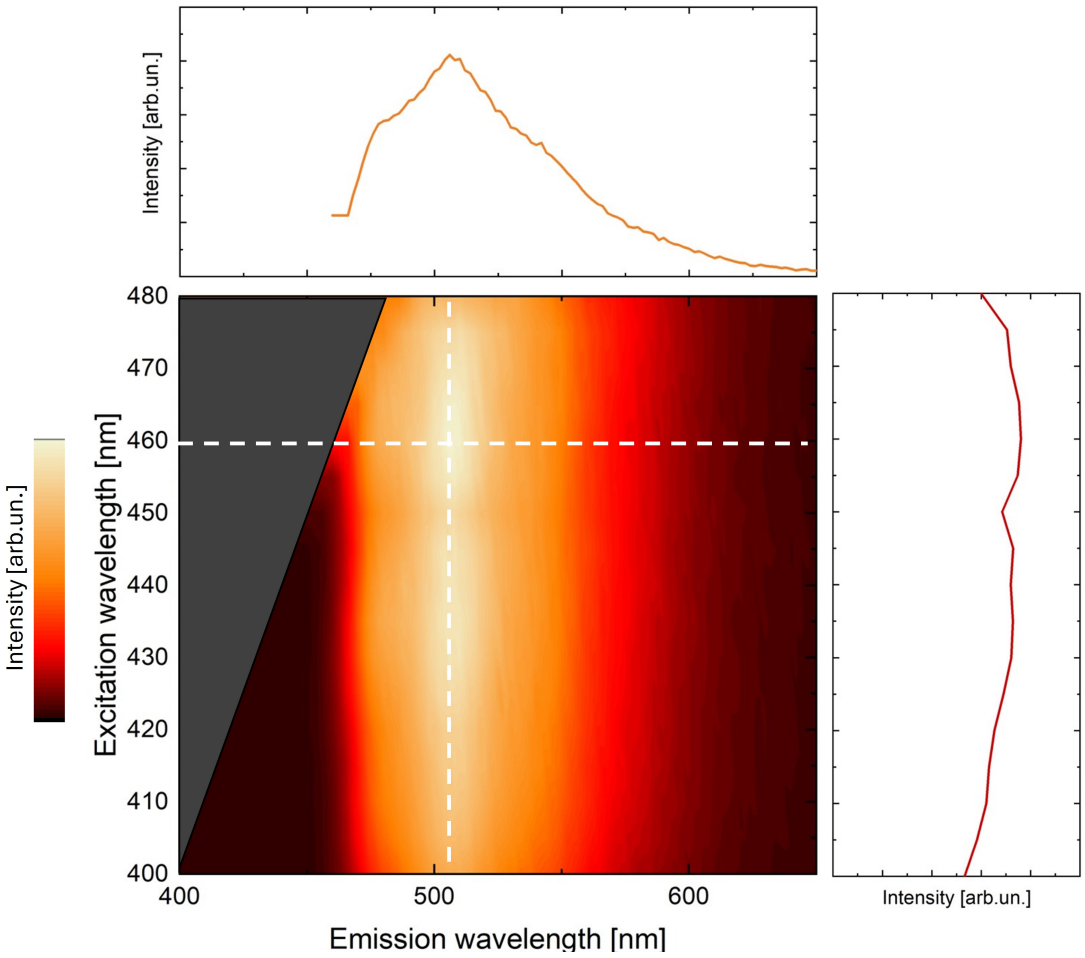

Figure 3.3: Example of a 2D EEM for CHROMA® green auto-fluorescent slide measured with Fluorolog®-3 Model FL3-21 spectrofluorometer. The inserts represent the excitation spectrum measured by observing the emission at 510nm (vertical cut) and the emission spectrum with excitation at 460nm (horizontal cut).

the emitted radiation is analyzed;

- in (fluorescence) excitation spectroscopy a tunable source excites the sample and only one emission wavelength is observed.

Information retrieved from these spectra is different. (1) Emission gives information about vibrational levels of the ground electronic state, since the excited state reached after absorption quickly relaxes toward its ground vibrational level; radiative decays then involve the same initial vibronic state but different vibrational levels of the ground state. (2) Excitation gives information about vibrational levels of the excited electronic state, since the majority of the molecules of the system usually are in the lowest vibrational level of the ground electronic state, so slightly different absorbed wavelengths are referred to different vibrational levels of the reached electronic state.

It is interesting to note that excitation and absorption spectra may appear equivalent,

but a conceptual difference underlies: *absorption* reveals how many photons are removed from the incident beam due to the presence of the sample, i.e., they are all absorbed inducing an excitation of the system, but this can end up with either a radiative emission or an increasing of internal energy in presence of non-radiative processes. On the other hand, an *excitation* spectrum reveals only those absorbed photons that lead to detectable radiative emission.

It is even possible to measure both emission and excitation spectra obtaining the so-called *excitation-emission matrix (EEM)*: it is a 2D map where emission spectra are acquired as a function of excitation wavelength. Referring to Figure 3.3, a vertical cut corresponds to a single excitation spectrum measured at a fixed emission wavelength, while a horizontal cut to the emission spectrum with a specific excitation.

Experimental techniques for emission spectroscopy

Radiation emitted by the sample after a certain excitation (either with a monochromatic or a broadband source) can be analysed in the frequency domain, with a traditional dispersive spectrometer, or with a temporal approach (FT spectrometer). The first is the case of a traditional spectrofluorometer (Figure 3.4), where an excitation monochromator allows one to select a specific incident frequency and the second one scans the fluorescence signal spectrally.

Experimental techniques for excitation spectroscopy

The basic idea is to measure emission intensity in a fixed passband, upon scanning the excitation wavelength. In a traditional spectrofluorometer (Figure 3.4) the scan is performed through an excitation monochromator but the same result can be obtained with a tunable filter [21] after a broadband source.

An alternative technique is based on Fourier transform: a temporal modulation of the excitation radiation is obtained with an interferometer [47], [79], [91]; since the resulting emission from the sample inherits the same modulation, a Fourier transform of the fluorescence signal gives access to the excitation spectrum.

To better understand this concept, we can focus on the effect of a single spectral component ν_A on the sample (see Appendix B for details). At the output of the interferometer we expect a cosinusoidal interferogram with frequency ν_A that is sent on the sample. Assume that these photons are absorbed, inducing the transition $S_0(0) \rightarrow S_1(1)$ (numbers in parenthesis are referred to vibrational levels). After a rapid decay (internal conversion) to the lowest vibrational level of S_1, photons at optical frequency ν_E are emitted. If fluorescence intensity is measured for each step, an interferogram with the same

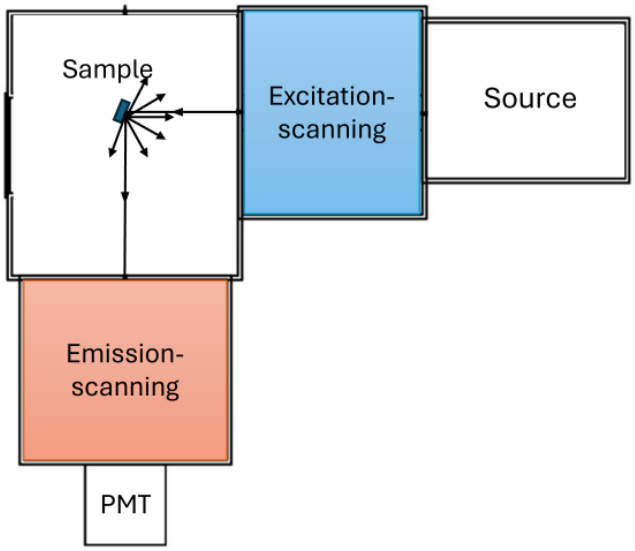

Figure 3.4: Schematic diagram of a spectrofluorometer. The source typically has high intensity for all the wavelengths (e.g. xenon lamp). Excitation and emission monochromators can be based on a single or double-grating configuration; the latter improves the system stray light rejection (scattered light from the sample often finds its way through the exit along with the selected band of emitted light, but, when the band is re-dispersed by a second grating, most stray light is stripped away). The detector must be sensitive in the spectral range of interest and adequate for low light conditions (e.g. a photomultiplier tube, PMT).

frequency as the incident one ν_A is retrieved irrespective of the emitted photon energy. A Fourier transform of this interferogram then gives information about the incident spectral component that has been absorbed and has stimulated the emission.

The real measurement consists in

1. scanning the delay between the two replicas of the source field generated through an interferometer;

2. detecting fluorescence signal from the sample in a broad wavelength range, as a function of delay;

3. computing the Fourier transform of this interferogram (after constant value subtraction) to retrieve the excitation spectrum.

Of the two principal methods for measuring excitation spectra discussed so far, which involve either a scanning of the excitation wavelength or a modulation of a broadband source, the latter brings in two significant advantages:

- the sample is continuously excited by radiation spanning the entire spectral range of interest, therefore a higher excitation power, and consequently an increased flu-

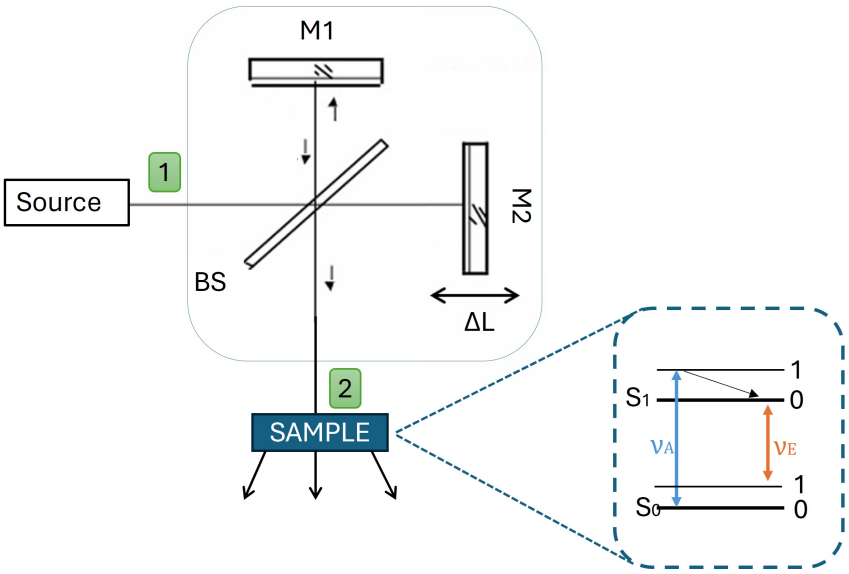

Figure 3.5: Implementation of Fourier transform excitation spectroscopy: a broadband source (1) passes through an interferometer (here, a Michelson interferometer), hence a modulated intensity (2) excites the sample. Its energy levels and transitions are represented in the insert.

orescence emission, is available with respect to the case of narrowband incident radiation;

- since emitted wavelengths are detected at the same time, SNR is increased with respect to single-emission wavelength detection; an increase in signal strength may enable high-speed hyperspectral imaging for time-dependent measurements, such as live-cell FRET and Ca_{2+} imaging.

As already mentioned, absorption and excitation spectra may not be identical, in particular in presence of complex systems; it is then interesting to highlight the difference in acquisition methods.

To acquire an absorption spectrum the amount of incident light transmitted by the sample is measured. The most intuitive approach consists in splitting the incoming radiation into two branches, one for reference and the other with the sample, and using an interferometer as FT spectrometer. The absorption spectrum then results from transmitted light normalization by the source. Actually, it can be more convenient to place the interferometer before the sample [42], [72], [76]: since we are looking at transmitted frequency components, introducing the modulation of light before or after the interaction with the material gives identical results due to linearity of Fourier transform operation. One may prefer analysing excitation spectra rather than absorption ones since far superior signal-to-noise ratios are usually obtainable with the background-free fluorescence-based detection; single molecules represent an example due to their very limited absorption [91].

Experimental techniques for EEM

With these concepts we can understand how to measure also the EEMs (*excitation-emission matrices*). In a traditional spectrofluorometer (Figure 3.4) an emission spectrum is acquired for each excitation wavelength scanned in the range of interest. Alternatively, time domain approach consists in

1. exciting the sample with a modulated source (as described above for excitation spectroscopy);
2. measuring the emission spectrum (either with a second interferometer [75] or with a dispersive spectrometer [76]) $I(t_1, \nu_2)$ as a function of delay t_1, introduced by the excitation interferometer, and emission frequency ν_2;
3. performing the Fourier transform with respect to t_1.

The 2D map $I(\nu_1, \nu_2)$ as a function of both excitation, ν_1, and emission, ν_2, frequencies is retrieved.

An EEM can be measured for each pixel of an extended sample typically with a raster-scanning approach. A widefield configuration, in which an EEM is recorded for all pixels in parallel, may be implemented using two synchronised TWINS interferometers, one in the excitation path, to modulate the broadband source, and another one in the detection path, to measure fluorescence emission.

3.2. Raman spectroscopy

In a quantum mechanical description [7, Chapter 10] the molecule is described through a wavefunction; with Born-Oppheneimer approximation nuclear motion can be treated separately from the electronic problem: a normal mode is a collective motion of the atoms in which nuclei vibrate around their equilibrium positions with a characteristic frequency of oscillation, ν_V. Vibrational levels of the system are then separated by the quantum of energy $h\nu_V$. Vibrational transitions involve two vibrational levels of the same electonic state, but only some of them are allowed by selection rules (see Appendix A).

To study vibrational levels in molecules two approaches are available: (1) absorption of infrared radiation (IR spectroscopy) [42]; (2) (inelastic) Raman scattering [83]. The first is based on the same principle of the above-mentioned electronic spectroscopy, since absorption peaks define the energy separation between vibrational levels (of the same electronic state); the commonly used range for IR spectroscopy is 2.5-25 μm (4000-400 cm^{-1}). The latter has a different physical origin. When a monochromatic light at frequency ν_0

irradiates the sample, both elastic (Rayleigh) and inelastic (Raman) scattering occurs; in a quantum-mechanical description, the incident photon leads the system to a *virtual state* given by the superposition of stationary states of the molecule, therefore it has a very short lifetime and rapidly decays to the ground state. If the final vibrational level has energy $h\nu_v$ higher from the initial state, the emitted photon, at frequency $\nu_S = \nu_0 - \nu_V$, will be less energetic than the absorbed one (*Stokes peak*), otherwise a higher frequency $\nu_{AS} = \nu_0 + \nu_V$ radiation will be emitted (*anti-Stokes peak*). Since at thermal equilibrium most of the population is in the lowest energy level, the Stokes component is much more intense than the anti-Stokes one. Nevertheless, the main drawback of Raman scattering spectroscopy is the very low cross section (only one photon over incident $10^9 - 10^{12}$ photons undergoes such inelastic scattering).

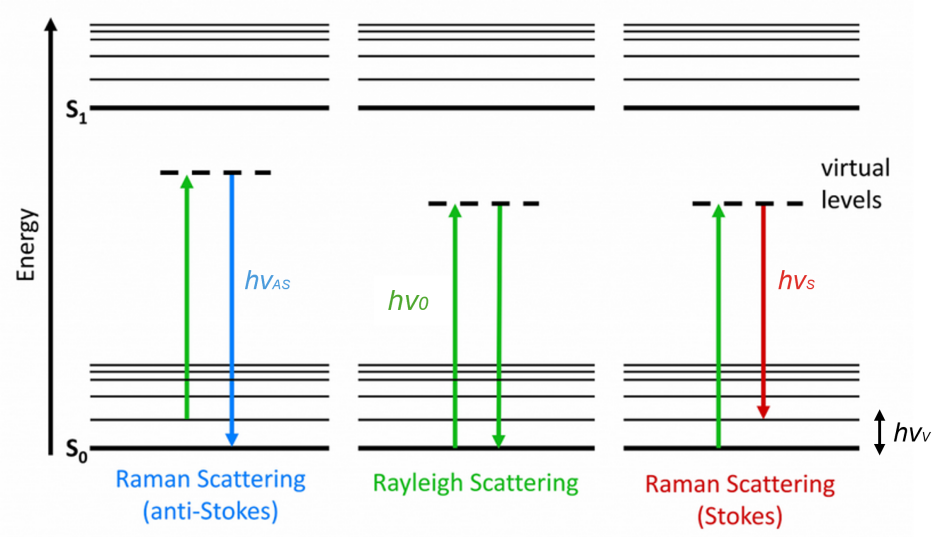

Figure 3.6: Perrin-Jablonski's diagram showing the origin of Rayleigh, Stokes and Anti-Stokes Raman scattering. *Image adapted from [29].*

Both Raman scattering and IR-absorption are useful to explore all the vibrational states, since different selection rules govern the transitions induced in one and the other mechanism, i.e., there can be *IR-active* or *Raman-active* transitions. In this way the chemical composition of the sample can be fully investigated.
We will focus on Raman scattering technique that brings in some advantages with respect to IR-absorption spectroscopy:

1. better spatial resolution is achieved when working with visible or near-IR radiation, since longer wavelengths and typically lower numerical apertures for IR objectives increase the dimension of diffraction-limited spots;

2. visible and near-IR detectors are much less expensive and typically less noisy than IR detectors (e.g., based on narrow energy gap mercury cadmium telluride);

3. in biological samples there is a strong absorption from water that affects particularly IR-absorption measurements.

Experimental techniques for Raman spectroscopy

Since spontaneous Raman cross section is very low, the excitation light power on the sample has to be high in order to increase Raman signal at the detector, but at the same time it must not exceed the damage threshold of the material under investigation. Another requirement is a precise incident wavelength such that narrow Raman peaks can be seen in the acquired spectrum: with an ideal monochromatic radiation a peak shifted from the incident frequency by the characteristic vibration frequency ν_V would show a width only determined by the instrumental spectral resolution; in practice, the broader the excitation light linewidth, the broader the resulting Raman peak, since all the incident photons undergo the same shift. The excitation source for Raman measurements is then a narrowband laser light and the measured spectrum is typically given as a function of *Raman shifts* rather than in wavelengths: saying λ_0 the laser incident light and λ the detected wavelength, Raman shift is defined as $\frac{1}{\lambda_0} - \frac{1}{\lambda}$ that is directly proportional to the vibrational energy difference $\hbar\nu_V$.

Raman microscopy is typically performed with a point-scanning technique: monochromatic radiation is focused on the sample point after point; by means of proper spectral filters, Rayleigh-scattered excitation light is not collected while Raman photons and eventual fluorescence signal can be detected and analysed through a spectrometer. The main drawbacks of this approach are: (1) long exposure time for each point of the sample, since Raman signal is very weak, which leads to long acquisitions for a large FOV imaging; (2) fluorescence signal is usually more broadband and much more intense than Raman peaks, therefore post-processing techniques have to be adopted to remove fluorescence background and enhance significant peaks.

A strategy to reduce fluorescence contribution is using a longer excitation wavelength, since absorption (and hence fluorescence) is typically lower; however, this also implies a reduction of Raman signal itself because the scattered (both elastically [41, Chapter 11] and inelastically [78, Chapter 7]) light power is proportional to the fourth power of the excitation frequency.

Another solution is represented by time-gated Raman spectroscopy, based on pulsed excitation and time gated detection: fluorescence has a slower temporal dynamics compared to Raman scattering, therefore fluorescence can be rejected by detecting only the instantaneous Raman signal [57], [93].

Fourier transform spectrometers have been exploited for raster-scanning Raman mi-

croscopy: they have higher throughput, due to the absence of filters for fluorescence and slits, but no significant improvements in terms of acquisition times have been introduced with respect to dispersive techniques. To increase acquisition speed it is then possible to exploit a widefield configuration, i.e., illuminating a large field of view of the sample and measuring the interferogram (and so the spectrum) for each pixel of a 2D detector simultaneously. This approach has two main requirements: (1) delays between replicas produced by the interferometer must be controlled to a fraction of the optical cycle; (2) all rays of the pencil from an object point should undergo similar phase delay to guarantee high fringe visibility. In [50] and [66], [94] some possible implementations are presented, but with some limits in terms of insufficient spectral resolution for Raman spectroscopy or complexity of the apparatus, respectively. On the other hand, as already discussed in the previous Section, the TWINS birefringent interferometer in the uniform-ZPD configuration is adequate for this purpose. Moreover, also the fluorescence background can be managed with a proper sampling strategy. Practical implementation will be described in Chapter 3.

4 | Chapter 4- Hyperspectral microscope design

In Chapter 3 we gave an overview of various signals that can be measured from a sample. Now we describe the implementation of a multimodal hyperspectral microscope that allows us to collect all this spectral information: Section 4.1.1 refers to the uniform-ZPD configuration in a widefield microscope for fluorescence and Raman spectra acquisition; in Section 4.1.2, we discuss how to modulate the excitation light of the microscope in order to measure also excitation spectra.

4.1. Hardware implementation

To acquire the various spectra described in previous Chapters we use an upgraded Leica DMRBE microscope: a TWINS interferometer placed in the *detection* path, before the detector, allows us to acquire emission and Raman signals and to perform reflectance and transmission measurements. An interferometer in the *excitation* path modulates a broadband light source in order to retrieve excitation spectra.

4.1.1. TWINS in detection for fluorescence and Raman spectroscopy

A TWINS interferometer is placed between the tube lens and the 2-dimensional pixelated detector (EMCCD camera, ANDOR Luca^{EM}-R, Oxford Instruments, Ireland) with $8 \times 8mm^2$, 1002×1004 pixels, 14-bit depth and spectral sensitivity from 400 nm to 1000 nm. This guarantees to obtain a 55% visibility and almost a uniform-ZPD configuration across the FOV due to the mechanical constraints posed by the microscope chassis that does not allow a perfect match of focal distances between optical elements, as presented in Chapter 2.

Both monochromatic laser and broadband light can be coupled to the microscope via a multimode fiber: a series of optical elements projects the image of the fiber tip on the

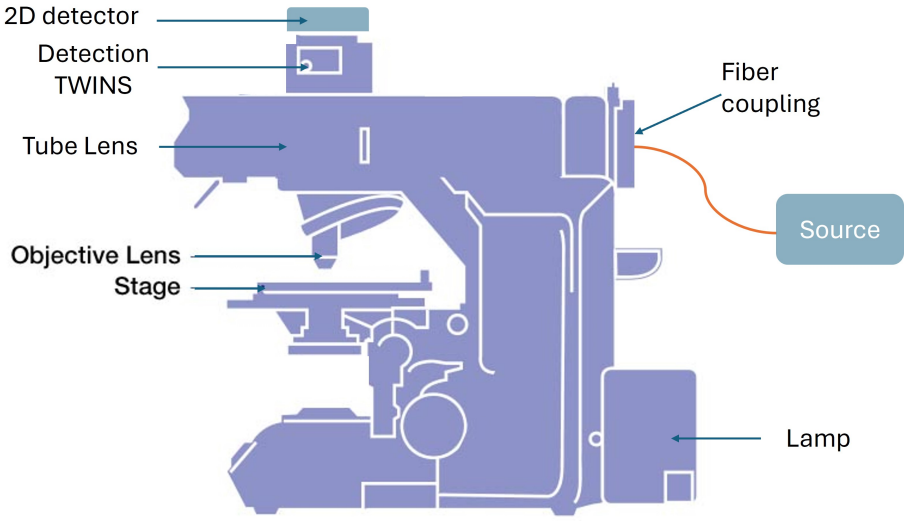

(a)

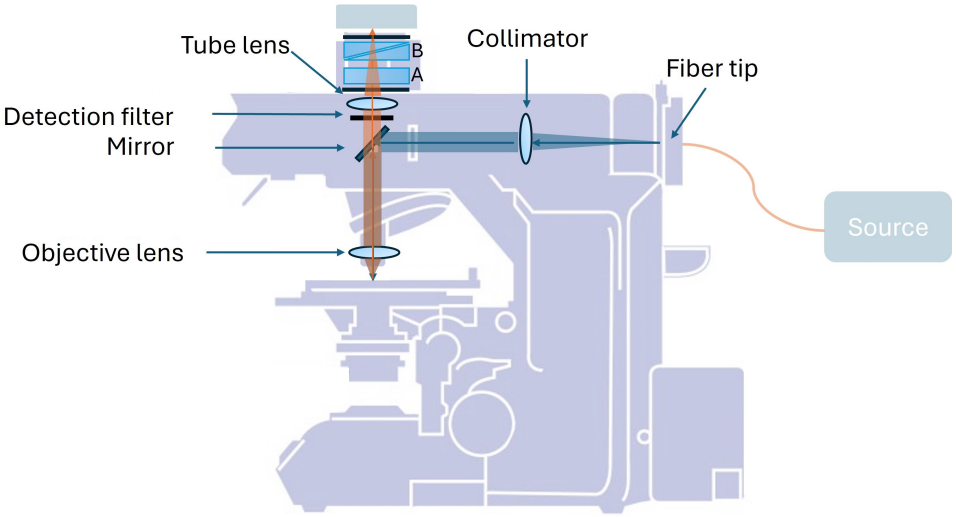

(b)

Figure 4.1: Schematic of the hyperspectral microscope with TWINS placed between detector and tube lens in uniform-ZPD configuration. (a) In the epi-illumination configuration light from a *Source*, either a laser or an incoherent source, is coupled to the microscope through a fiber and arrives on the sample from the top. Alternatively, a widefield transmission geometry is also available, in which a halogen lamp (*Lamp*) illuminates the sample from the bottom. (b) Optical elements along both illumination and detection paths are highlighted: the collimator is a simplified representation of the optics that produce a collimated beam from the fiber tip; a mirror (either a 50:50 beam splitter or a dichroic mirror) reflects this light such that the objective lens can focus it on the sample plane; the signal is collected from the sample by objective and tube lenses that create the conjugated image on the detector.

sample plane, guaranteeing a uniform spot of variable dimension according to the fiber core size and the objective magnification (see Section 4.2.2 for details). In the so-called *epi-illumination* configuration, radiation from the sample is collected by the same objective as the one for illumination, then an $f = 250mm$- focal length tube lens focuses it on the detector plane. Proper filters (typically excitation filter, dichroic mirror and suppression/detection filter) are necessary to spectrally separate the emission/scattering from the sample from the excitation light.

Crystal	$\mathbf{\Delta n = n_e - n_o}$	$\mathbf{n_0(\lambda = 630nm)}$	**Transparency μm**
YVO_4	+0.222	1.9929	0.4-5
$CaCO_3$	-0.1705	1.6557	0.35-2.3
α-BBO	-0.139	1.6707	0.19-3.5
$LiNbO_3$	-0.086	2.286	0.4-5
Hg_2Cl_2	+0.6596	1.9641	0.38-20

Table 4.1: Uniaxial birefringent materials; positive (negative) uniaxial crystals have $\Delta n > 0$ ($\Delta n < 0$).

The design of TWINS requires two steps: the choice of birefringent material and geometrical parameters of wedges and plate.
Different uniaxial birefringent materials are available and the choice is the result of a trade-off among

1. transparency range;
2. birefringence (the higher Δn, the larger delay is introduced at fixed wedge displacement, as discussed in formula 2.3);
3. value of the refractive index (the higher it is, the stronger spatial walk-off [13, Chapter 14] is introduced between replicas propagating inside the wedges, reducing the interferometric contrast at detector plane).

In the detection path, YVO_4 resulted to be the best option: its large transparency range allows us to detect emission with a tunable illumination wavelength; its refractive indexes introduce a limited walk-off and its high birefringence makes it possible to scan long delays (a relevant feature for Raman scattering measurements, as will be discussed in Section 4.2). Wedges (block B in Figure 4.1b) were cut from the same crystal with $\alpha = 10°$ apex angle and transverse size of 30 mm (limited by constraints in crystal growth

technique). Translation is performed by a motorized step system (25 mm travel range, 0.02 μm step size) and driven by a motor controller connected to the PC. A custom LABVIEW software allows us to set measurement parameters (see Section 4.2) for both the motor and the camera, in order to automatise the acquisition of temporal hypercube: an image is recorded for every motor/wedges position during the scan.

4.1.2. TWINS in illumination for excitation-resolved spectroscopy

This thesis work mainly focuses on a further implementation of the above-mentioned upgraded Leica DMRBE microscope: it consists in an additional module that allows us to modulate properly the excitation light in order to have access to the excitation spectrum of the sample.

The working principle of the temporal-domain approach for excitation spectroscopy was described in details in Chapter 3: modulating the spectral components of the broadband source results in a modulation, with identical period, of the fluorescence signal stimulated by the frequencies absorbed by the sample; its Fourier transform retrieves the excitation spectrum. In our microscope the modulation is obtained through an α-BBO TWINS interferometer: wedges, with apex angle of $\alpha = 7°$, are translated through a motorized system driven by a motor controller connected to the PC. The temporal hypercube acquisition is performed with the same LABVIEW software mentioned above. In this case, an entire delay scan generates an intensity modulation (interferogram) for each frequency component of the source spectrum; exploiting the microscope optical system for uniform illumination, the sample is excited with these modulated spectral components, thus it emits a modulated red-shifted fluorescence signal. The entire fluorescence emission detected at each step allows us to acquire a temporal hypercube, which gives the excitation spectrum of the sample after a Fourier transform operation.

It must be noticed that the YVO_4 TWINS after the sample is not necessary when acquiring excitation spectra: to avoid losses associated with all the optical elements inside this TWINS (polarizers reduces the incident power by a factor of 4 and all surfaces introduce Fresnel losses), it can be removed from the microscope during these measurements.

Set-up development

We coupled the modulated excitation source through the same fiber coupling system described for emission measurements: this allows us to change source (for example to switch from excitation to emission spectra acquisition) in a few minutes.

The main requirements for this set-up are:

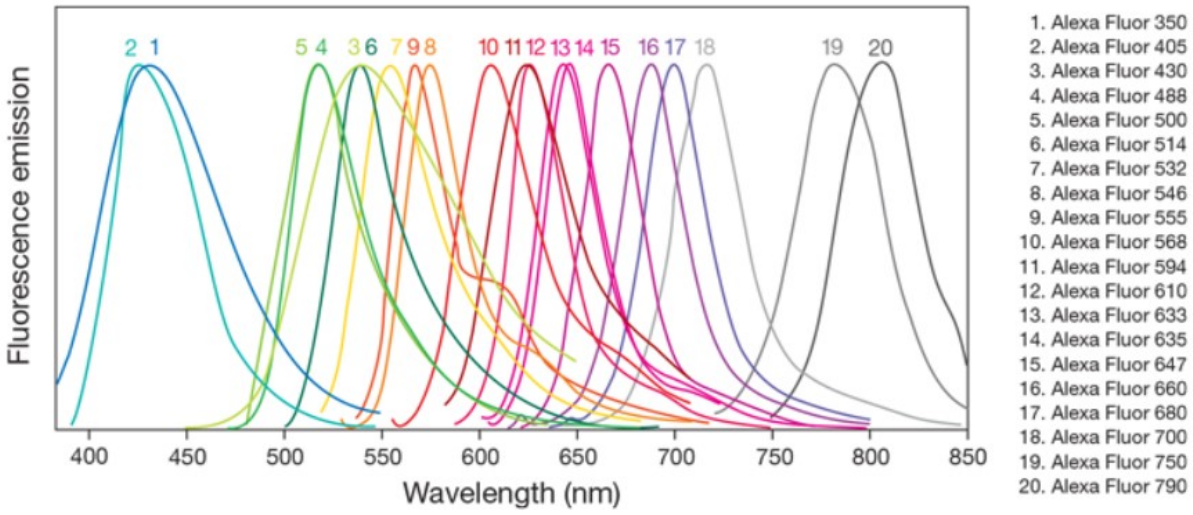

Figure 4.2: Emission spectra for Alexa Fluor^{TM} fluorescent dyes: emission peaks span from 442 nm to 814 nm and correspondingly excitation wavelengths are a few tens of nanometers blue-shifted. Since they are largely employed as cell and tissue labels in fluorescence microscopy, they are representative of the typical range of interest for excitation spectra for biological samples. *Image from ThermoFisher SCIENTIFIC online catalog.*

1. a broadband source with a uniform spectrum extended from low-wavelength components (350 nm) to near IR (750 nm) to match the excitation wavelength of a large variety of samples (e.g. fluorescent proteins widely used to label biological tissues, Figure 4.2);

2. coupling as much power as possible from the incoherent lamp into the microscope;

3. keeping a good contrast of interferometric fringes at the output of the excitation TWINS and on the sample plane.

The final adopted configuration represents a good compromise among these conditions: referring to numbered elements in Figure 4.3

1. a 100W halogen lamp with dichroic reflector (64627 HXL, OSRAM) provides the excitation light. It is an incandescent lamp that produces thermal radiation from an electrically heated filament placed in a glass bulb filled with a gas mixture that contains a small amount of a halogen (xenon). Its spectrum is associated with the temperature of the emitter by Wien's law [97]:

$$\lambda_{max} T = constant \tag{4.1}$$

with maximum power density at λ_{max}. Since its temperature is 3200K, its spectrum has a peak in the infrared (around 1 μm), therefore, to keep only the visible light,

the lamp reflector is a dielectric mirror that reflects the visible, transmitting or absorbing most of the infrared; its elliptical shape guarantees a relatively small image of the filament on the fiber tip and so the possibility of a better coupling of the light within the fiber NA;

2. a fiber collimator creates a collimated beam from the fiber output; this happens ideally for a point-like source placed at focal distance f_1 from the lens, but in pratice there is a beam divergence due to the spatial extension of the fiber core;

3. a series of metallic mirrors guides the beam through the TWINS parallel to its optical axis;

4. a lens collects the beam emerging from the interferometer and focuses it on the tip of a second fiber; its focal length f_2 is chosen adequately to match the fiber acceptance angle and core dimension. Since the two fibers are identical, $f_1 = f_2$;

5. light is coupled to the microscope, as in Section 4.1.1.

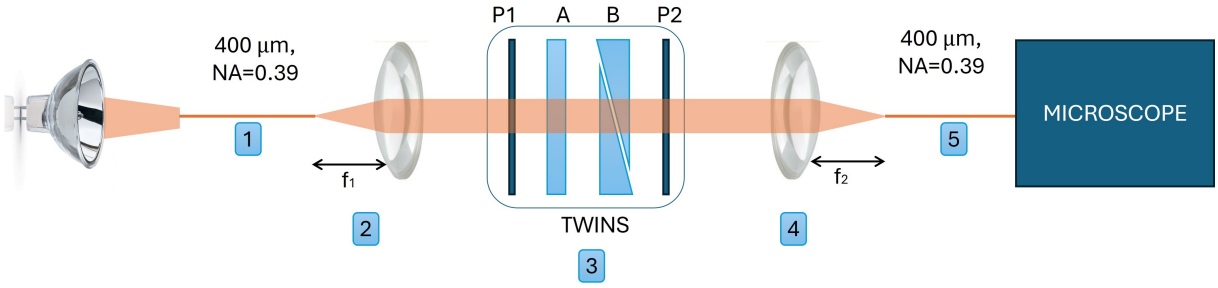

Figure 4.3: Practical implementation of microscope excitation path: light from a halogen lamp is coupled to a fiber and collimated; after crossing the α-BBO TWINS interferometer it is focused back into a second fiber connected to the microscope.

Steps 1. and 2. are fundamental to create a high degree of collimation from a completely incoherent source: the resulting configuration is the *high fringe visibility* scheme described in Chapter 2, with the first fiber output representing the object plane. The limited divergence of the beam after the collimator means that bundles of parallel rays cross the TWINS with relatively small angles α_0 (using the same notation as before), therefore the phase does not vary significantly within the spot at the input of the second fiber. This guarantees a high contrast also on the sample plane, after the effect of intensity averaging introduced by the fiber (Figure 4.4).

To characterise the interferograms, we measured a Spectralon (Labsphere, Inc., North Sutton, USA), which is a sample with white highly diffusive surface, in reflection configuration (a 50:50 beam splitter is used as mirror in Figure 4.1b). Incident light is reflected

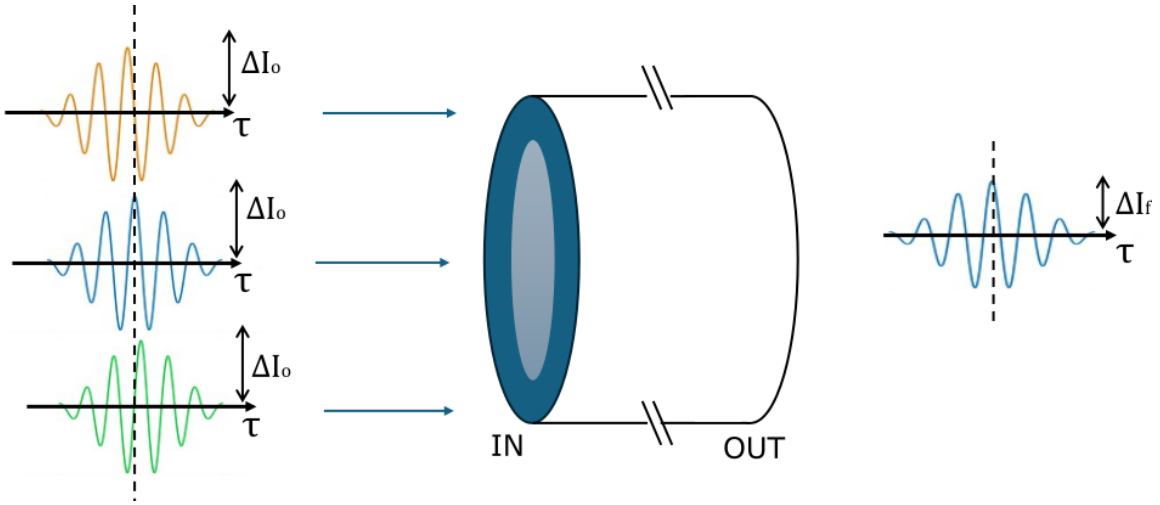

Figure 4.4: Pictorial view of the averaging effect of the fiber: interferograms in different positions of the fiber tip have different zero path delay positions, therefore the output interferogram shows a reduced contrast (same average intensity, but lower oscillation amplitude $\Delta I = I(0) - I_{ave}$), resulting from the average.

by the sample and directly detected with the monochrome camera while it is modulated with the α-BBO TWINS; after Fourier transforming the acquired temporal hypercube, the source spectrum is retrieved for each pixel. Figure 4.5 shows the uniform distribution of zero path delay positions throughout the illuminated spot (ZPD is given in units of phase shift for a wave at 600nm) and the average contrast achieved of 75%.

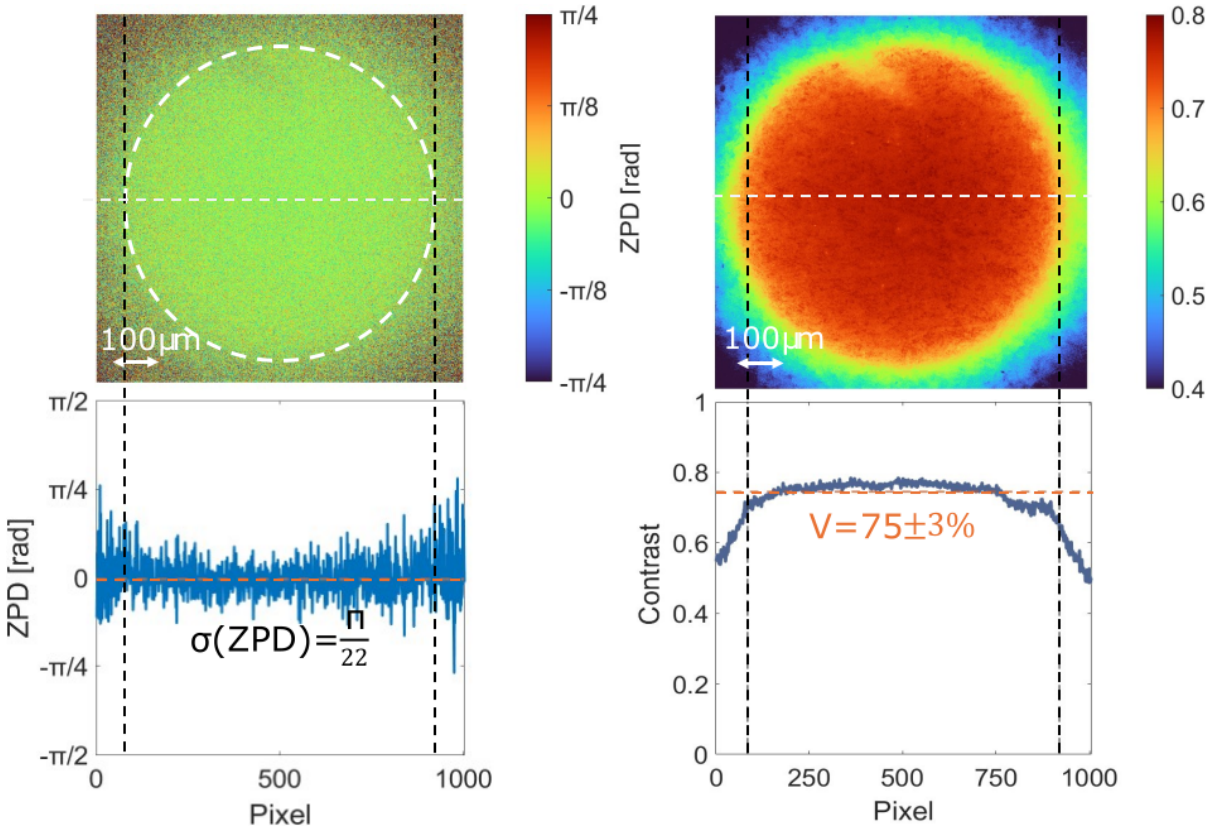

Figure 4.5: (a) Map and horizontal section of the ZPD expressed in units of the phase shift for a wave at 600nm: it can be considered uniform across the illuminated spot (white dotted line) since the standard deviation $\sigma(ZPD)$ is $\frac{\pi}{22}$. The phase fluctuation for adjacent pixels is an artifact of the analysis algorithm. (b) Contrast evaluated in the range of interest [380-750]nm across the FOV: only a section (horizontal white dotted line) of the illuminated spot (delimited by vertical dotted lines) is considered to compute the average contrast. Note that there is light also outside the illuminated spot: it is diffusion by the surface of the Spectralon.

4.2. Measurement parameters

In this Section we will discuss the general concepts of acquisition parameters and calibration, which hold for all operating modes discussed so far.

4.2.1. Detector parameters

Our detector is an electron multiplying charged coupled device (EMCCD), that is a typical silicon-based CCD with an additional *multiplication* (or *gain*) register that provides on-chip electron amplification: this allows us to deal with extremely weak signals.

Apart from the improved readout channel, what happens in each pixel of the 2D sensor is the same as in a usual CCD. During the **integration time** of each frame the sensor image area is exposed to radiation and some of the detected photons are converted into electrons (the likelihood of collecting an output electron per absorbed photon is the quantum efficiency (QE) of the camera); the electronic charge generated is then shifted toward the frame store area, not illuminated, where the real readout and the amplification processes take place. The latter is based on the concept of *impact ionization*: when the charge is moved through a register by varying potentials applied to potential wells [59, Chapter 6], the probability of impact ionization is low, since it occurs only when an electron has sufficient energy to create another electron-hole pair (in other words, a free electron charge in the conduction band can create another charge). If charge energy is increased with proper electrode design, the viability of this process increases and the more potential wells are present in the gain register, the higher the amplification becomes. The tunable parameter in case of very weak signals is then the **gain** of this multiplication.

The importance of amplification is related to the detection system noise. A signal can be effectively detected only when it overcomes the detection limit of the system; this condition occurs when the signal-to-noise ratio is higher than one. In modern silicon-based detectors the two primary sources of noise are dark current noise (shot noise) and readout noise (thermal and flicker noise) [59, Chapter 7]; the amplification is useful when the system is dominated by the second.

Another strategy to improve SNR is via **binning**: during readout the charge accumulated in each pixel is moved toward the readout register; binning is a process that allows charge from two or more pixels to be combined before readout. Summing charge and doing a single readout gives better noise performance than reading out several pixels and then summing their signal in post-processing, because each act of reading out contributes to noise [101]. The choice of an adequate binning is also driven by the requirements in terms of spatial resolution, since it leads to a minimum distinguishable detail (dimension

of pixel cluster) that is larger, and so more limiting, than the diffraction limit given by $\frac{\lambda}{2 \cdot NA}$.

4.2.2. Microscope parameters

Our microscope illumination is provided through the same objective lens as the one in the detection path: this is the so-called **epi-illumination**. It follows that the choice of filters is fundamental in order to excite the sample with a certain wavelength (or range of wavelengths) and collect only the red-shifted emission, without any residual excitation light.

In Section 4.1.1 we already mentioned the possibility of adjusting the illuminating spot dimension on sample plane by a proper choice of the objective: with a 400 μm-core fiber used for illumination, spot diameter is 82% of the whole FOV, that can vary from 1600μm with 5x to 80μm with 100x objective (Table 4.2 summarises the main characteristics for objectives used in this thesis work).

Objective	NA	FOV dimension
Leica® PL FLUOTAR 10x	0.30	800μm
Leica® PL FLUOTAR 20x	0.50	400μm
Leica® PL FLUOTAR 50x	0.80	160μm

Table 4.2: Magnification, numerical aperture (NA) and corresponding field of view dimensions for the objectives used in this thesis work.

4.2.3. Scan parameters

In Chapter 1 we mentioned that two main parameters must be chosen to acquire properly the interferograms: (1) scan length; (2) sampling step.

Scan length

It determines the achievable **spectral resolution**: the longer the scan $2T$ (recalling the same notation as in Chapter 1), the better the spectral resolution $\Delta\nu$ (in terms of FWHM), since the relation between these two quantities is

$$\Delta\nu = 0.605\frac{1}{T} \tag{4.2}$$

or alternatively in the wavelength domain

$$\Delta\lambda = \frac{\lambda^2}{c}\frac{0.605}{T} \tag{4.3}$$

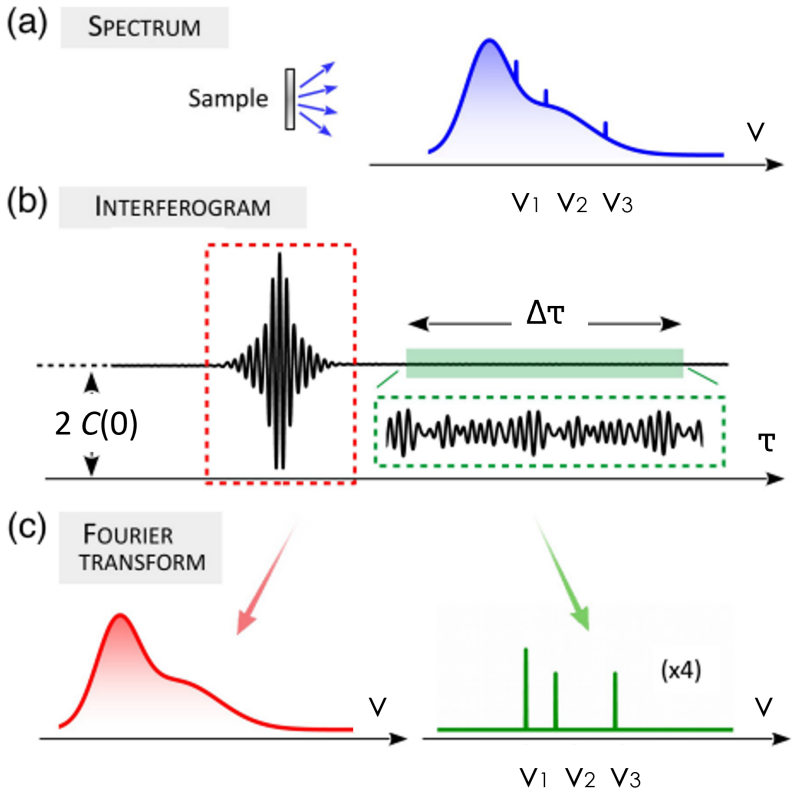

Figure 4.6: Schematic representation of the multimodality in Fourier transform spectroscopy: different sampling windows (dotted red and green respectively) allow us to retrieve separately different spectral features of the same sample. *Image adapted from [4].*

Additionally, the proper choice of initial and final delays, τ_1 and τ_2 respectively, enables us to retrieve different features of the radiation spectrum. To understand this, it is necessary to recall the correspondence between spectral features and temporal behaviour of the interferogram: a steep profile, i.e., a very rapid variation, in the spectrum gives a long-lasting interferogram (it is an infinitely-extended cosinusoidal function in the ideal case of the Dirac delta function for an ideal monochromatic radiation); on the contrary, a broad spectrum gives rise to a limited interferogram with the so-called *central burst* in correspondence of zero delay.

It follows that sampling the interferogram only at large delays allows one to obtain the narrow spectral features, while sampling around zero delay position gives access to broad ones (Figure 4.6). Therefore, when dealing with broad spectra, as in case of fluorescence

or excitation spectra, scan is centered around zero delay in order to include the central burst of the interferogram. On the other hand, a scan on the tails is chosen to retrieve only narrow peaks (e.g., Raman peaks). One can separate these signals without changing any other parameter but the sampling strategy, either symmetric early-delay interferogram or long-lived oscillations.

This temporal approach results to be extremely powerful when dealing with Raman spectra: acquiring only the tail of the interferogram, the retrieved spectrum does not show any fluorescence contribution, but only narrow peaks (Figure 4.6c). On the contrary, a dispersive spectrometer measures fluorescence and Raman peaks simultaneously, therefore the background can be removed only in post-processing with much more difficulty. Still, we have to deal with fluorescence during the acquisition: long-lasting oscillations are superimposed on the constant $2 \cdot C(0)$ which is the average energy on the detector. As the fluorescence signal becomes stronger, the energy increases, limiting the integration time for collecting Raman photons; extending it too long can cause fluorescence to saturate the detector dynamic range.

The importance of a high-birefringent crystal, as YVO_4, is now clear: to resolve the narrow peaks of a Raman spectrum, a long scan on the tail of the interferogram is required; a high Δn is more suitable, since it increases the maximum achievable delay, according to $\tau_{max} = \frac{\sin\alpha\, \Delta n\, x_{max}}{c}$. With the geometrical features discussed in Section 4.1.1 (maximum wedges excursion of 18 mm, or equivalently 2930 fs delay at 600 nm) we can achieve a spectral resolution of 21 cm^{-1}.

We recall that performing the longest available scan is not always the best approach: when the spectrum is broad, a scan much longer than the interval of early-delay oscillations is detrimental (artifacts appear in the spectrum) because, when oscillations are damped (interferogram becomes constant), what is effectively sampled is nothing but noise. Spectral resolution is necessarily worsen with a shorter scan, but this does not impact significantly on a broad spectrum.

Sampling step

The second relevant acquisition parameter is the **sampling period**, since any analog signal can be properly reconstructed only when a sufficient set of samples is acquired. The theoretical limit is given by Nyquist-Shannon's theorem (see Section 1.2.2): starting from the formula for the delay in a TWINS interferometer, we can derive the motor

sampling step Δx that fulfills the theorem

$$f_{sampling} = \frac{1}{\Delta\tau} = \frac{c}{\sin\alpha\ \Delta x\ \Delta n} \geq 2 \cdot \nu_{max}$$
$$\Delta x \leq \frac{1}{2}\frac{c}{\sin\alpha\ \Delta n\ \nu_{max}} \tag{4.4}$$

We already pointed out that this is the most restrictive sampling criterion which assumes a signal spectrum (0, ν_{max}); if $\nu_{min} \neq 0$ a longer sampling period can be chosen without the risk of spectral aliasing, enabling a significant reduction of the acquisition time, as shown in [4].

On the contrary, there is no lower bound, i.e., the sampling step can be chosen arbitrarily small: this can be useful since the higher the number of samples (N), the better SNR (increased by a factor N) is achieved [80], at the cost of lengthening the measurement time. Therefore, in a real measurement the optimal step is a trade-off between an improved SNR and a longer acquisition.

4.3. Calibrations

Any TWINS interferometer requires calibration procedures to (1) correlate the computed pseudofrequencies to the effective optical frequencies and (2) manage the errors in motor positions during the measurement. We highlight that these procedures, spectral and wedge translator calibrations respectively, do not need to be repeated at each utilization of the interferometer, since they only depend on the chosen birefringent crystal, its geometrical shape, namely the wedge apex angle, and the encoder for motor position, that do not change in multiple scans.

4.3.1. Spectral calibration

Interferograms are acquired as functions of wedge position x, therefore, a Fourier transform operation results in a spectrum $S(f_x)$, with f_x *pseudofrequency* or *spatial frequency* (see Section 2.1). To retrieve the spectrum $S(\nu)$ as a function of optical frequency ν it is necessary to find the relation F between the two variables ν and f_x, such that $\nu = F(f_x)$: this is the spectral calibration.

Considering a monochromatic radiation with optical frequency ν: we have already seen that the associated interferogram as a function of delay τ is a cosinusoidal function with same frequency

$$I(\tau) \sim 2 \mid A \mid^2 + 2 \mid A \mid^2 \cos(2\pi\nu\tau) \tag{4.5}$$

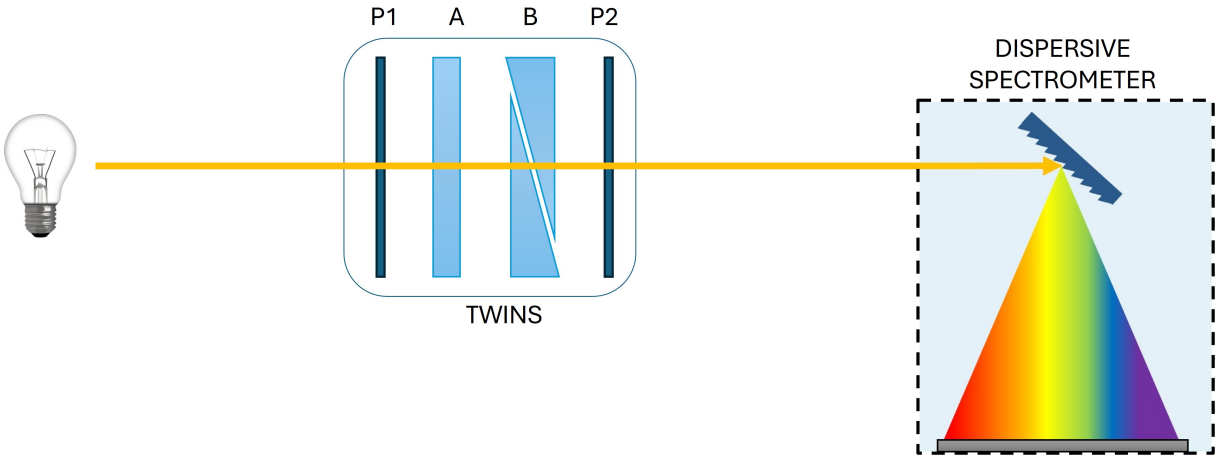

Figure 4.7: Schematic representation of the setup used for spectral calibration: light from a broadband source is modulated by the TWINS; a dispersive spectrometer is placed at the output of the interferometer to acquire a spectrum for each delay.

Since the measured interferogram depends on wedge position x, we can exploit the relation $\tau = \frac{\sin\alpha\,\Delta n\,x}{c}$ to obtain

$$\begin{aligned} I(x) &\propto 2 \mid A \mid^2 + 2 \mid A \mid^2 \cos(2\pi(\frac{\nu\ \sin\alpha\ \Delta n}{c})x) \\ &\propto 1 + \cos(2\pi f_x x) \end{aligned} \tag{4.6}$$

Performing the Fourier transform of the measured interferogram, after constant value subtraction, the spectrum $S(f_x)$ is retrieved: it has two peaks centered at f_x and $-f_x$, from which the pseudofrequency associated to the known optical frequency ν is determined. Repeating this procedure for different monochromatic beams, it is possible to derive the calibration function

$$\nu = F(f_x) = \frac{f_x\ c}{sin\alpha\ \Delta n} \tag{4.7}$$

In practice there are two possible approaches to work with more monochromatic beams: either narrow laser lines or, less intuitive, a broadband light source.

The first consists in measuring the interferogram as a function of motor positions for each laser and retrieve the corresponding pseudofrequency as discussed above: the more lasers are used, the more precise polynomial interpolation of the experimental values $\nu = F(f_x)$ is obtained.

The latter requires a different setup (Figure 4.7): the monochrome detector used to measure the interferogram is replaced by a dispersive spectrometer and the source is now broadband (the spectrometer acts as a stack of bandpass filters). The TWINS modulates the light: at each motor position x the spectrum of the total field E_{tot} at the output of

the interferometer is

$$\begin{aligned} S(\nu) = \mid \tilde{E_{tot}} \mid^2 = \mid \tilde{E}(\nu) + \tilde{E}(\nu)\, e^{i2\pi\nu\tau} \mid^2 = \\ = 2 \mid \tilde{E} \mid^2 + 2\, \Re\left\{ \mid \tilde{E} \mid^2 \; e^{i2\pi\nu\tau} \right\} = \\ = 2 \mid \tilde{E} \mid^2 (1 + \cos(2\pi\nu\tau)) \end{aligned} \tag{4.8}$$

It is modulated in the spectral domain (a phenomenon called *spectral interference*) with a period $\frac{1}{\tau}$ (the larger the delay, the closer the spectral fringes). Its physical origin is the interference among single spectral components of a generic radiation: a fixed delay τ between its replicas gives constructive interference for frequencies ν_1 such that $\tau = \frac{m}{\nu_1}$, with m positive integer, destructive interference when $\tau = \frac{2m+1}{\nu_2}$ and all intermediate conditions for other frequencies. Therefore the intensity of the spectrum is modulated with maxima for ν_1 and minima for ν_2.

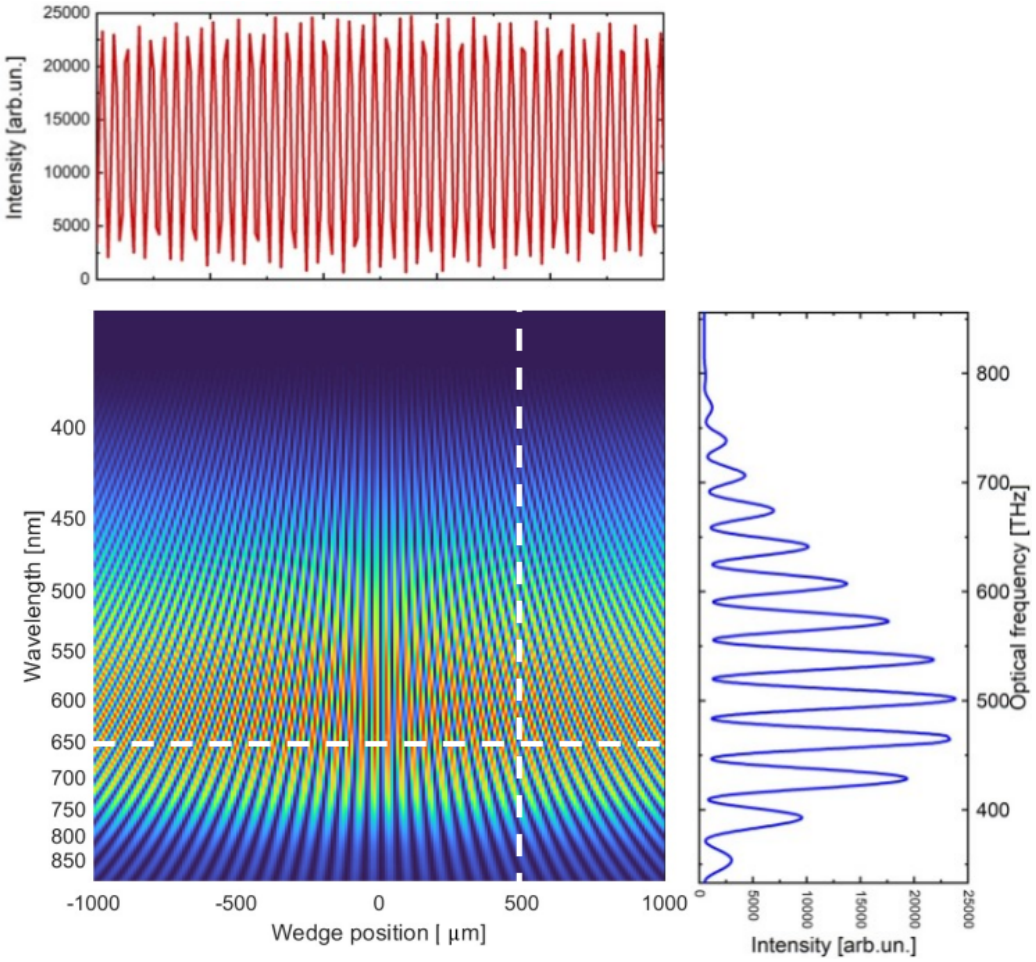

Figure 4.8: Stack of output spectra as a function of the wedge position: each column (vertical cut) is a spectrum at a fixed delay; each row (horizontal cut) corresponds to the interferogram at a specific optical frequency. This map was measured with a dispersive spectrometer (Hamamatsu Mini Spectrometer C10083CA) placed at the output of the interferometer.

Map in Figure 4.8 is obtained with a series of modulated spectra as function of motor position: a horizontal cut represents the intensity modulation for a specific wavelength at different positions, i.e., the interferogram for that monochromatic component. We can then apply the procedure previously described to any frequency in order to get the calibration curve $\nu = F(f_x)$ (Figure 4.9): it is almost a linear function, where the deviation from linearity lies in the frequency-dependent birefringence $\Delta n(\nu)$. In the insert we plot the peak in the spectrum (only positive frequency) obtained after Fourier transforming the interferogram for 650nm (461 THz): its FWHM is determined by the 2mm-scan length according to Equation 4.2 and the apodizing function (Happ-Genzel).

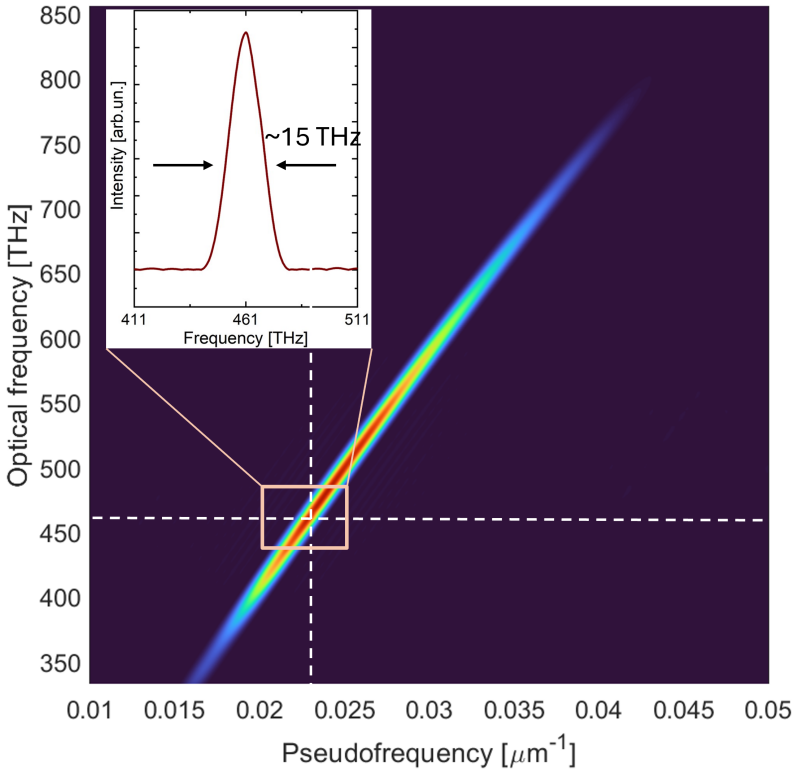

Figure 4.9: This intensity map results from Fourier transforming the interferograms for each wavelength in the range [350, 900]nm (horizontal cuts in Figure 4.8). The peaks allow us to retrieve the calibration function $\nu = F(f_x)$. In the insert an example of spectral peak: its FWHM is determined by total scan length (2mm) and apodizing function (Happ-Genzel).

4.3.2. Wedge translator calibration

During a scan, real wedge positions may differ from the expected ones generally due to imperfections of the wedge mounting or errors in the controller readings. This means that the interferogram is sampled in slightly different positions with respect to the expected, therefore artifacts may appear in the computed spectrum; they are mainly in the form of sidebands around the spectral peaks, thus they may be particularly detrimental for

already weak Raman peaks. To solve this problem a correction of the delay axis must be adopted.

Consider a monochromatic beam with optical frequency ν whose interferogram is sampled in $\{x\}$: Fourier transform of an ideal cosinusoidal function (after average value subtraction) results in two delta functions at f_x and $-f_x$; the back Fourier transform of only one of them is the complex interferogram

$$I_T(x) \sim e^{i2\pi f_x x} \tag{4.9}$$

In practice, an incorrect sampling leads to an improper reconstruction of the waveform, thus the above-mentioned inverse Fourier transform gives a complex interferogram

$$I_T(x) \sim |I_T| e^{i\phi_T(x)} \tag{4.10}$$

To retrieve the corrected wedge positions $\{x_{corr}\}$ we must impose the equality between the phases in (4.9) and (4.10)

$$\phi_T(x) = 2\pi f_x x_{corr} \Rightarrow x_{corr} = \frac{\phi_T(x)}{2\pi f_x} \tag{4.11}$$

This method works successfully for $\alpha - BBO$ TWINS interferometer [77]. An alternative approach, better suited for long scans with YVO_4 was developed [4]. The main difference is a multiplication by the phase term $e^{-i2\pi f_x x}$ before back-trasforming: motor-positioning errors introduce an additional phase term in the monochromatic wave interferogram

$$\begin{aligned} I(x) \sim \cos(2\pi f_x(x + \Delta x_{err})) &= \frac{1}{2}(e^{i2\pi f_x(x+\Delta x_{err})} + e^{-i2\pi f_x(x+\Delta x_{err})}) \\ &= \frac{1}{2}(e^{i2\pi f_x x + i\phi_{err(x)}} + e^{-i2\pi f_x x - i\phi_{err(x)}}) \end{aligned} \tag{4.12}$$

Then, a slowly-varying and a fast-oscillating terms appear after demodulation

$$I(x) \sim \frac{1}{2}(e^{i\phi_{err(x)}} + e^{-i2\pi 2 f_x x - i\phi_{err(x)}}) \tag{4.13}$$

Isolating only the first term, we get $\tilde{I}(x) \sim \frac{1}{2} e^{i\phi_{err(x)}}$; we can then retrieve the phase ϕ_{err} and Δx_{err}

$$\Delta x_{err} = \frac{arg(\tilde{I}(x))}{2\pi f_x} \tag{4.14}$$

Similarly to the previous discussion about frequency calibration, we extend the rea-

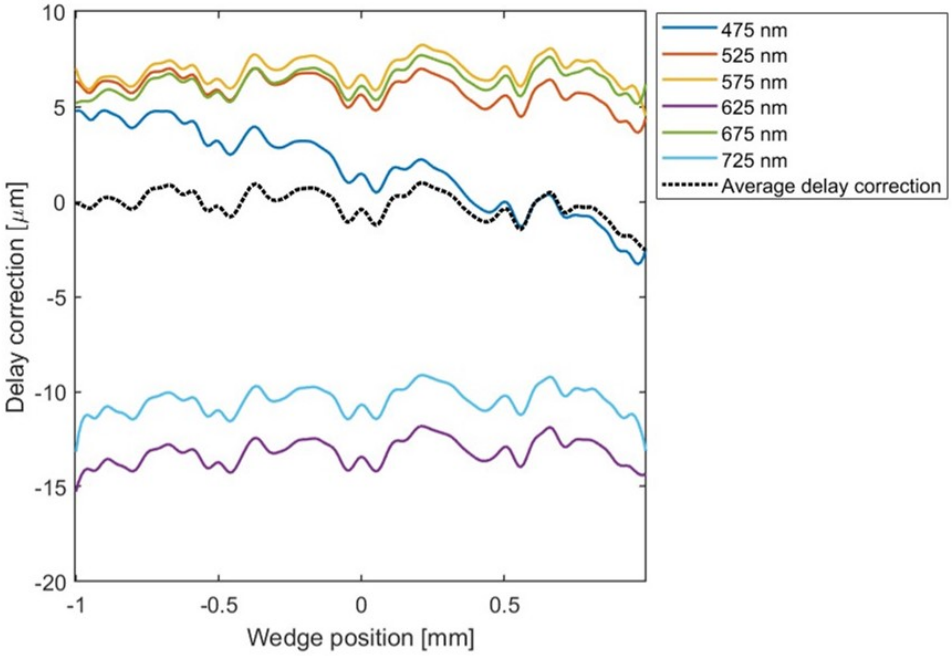

Figure 4.10: Delay correction as a function of wedge translator position for selected wavelengths of the source spectrum and their average: the shape is the same, while the vertical offset is an arbitrary shift in the delay axis of the interferogram, that can be removed easily.

soning from one monochromatic beam to a set of wavelengths measured with a dispersive spectrometer: repeating the procedure for each spectral component, i.e., by considering the associated interferograms obtained as horizontal slicing of the map in Figure 4.8, a delay correction can be retrieved for each wavelength. Since all interferograms are acquired at the same time, we do not expect much different positioning errors, so the final calibration is obtained as the average of the curves in Figure 4.10.

As shown in Figure 4.11, spectral artifacts are removed efficiently after delay correction; moreover, it has been noticed that this correction works properly in different measurements due to the high reproducibility of positioning error, therefore this calibration procedure does not need to be repeated for each scan.

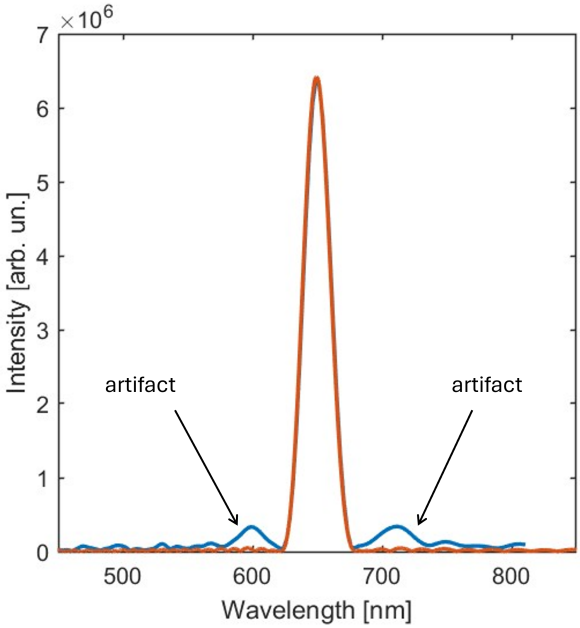

Figure 4.11: Representation of the effect of delay correction: considering a monochromatic component in the broadband source (in this example 650nm), the blue solid curve is the spectrum retrieved without applying wedge position correction; artifacts (sidelobes) appear clearly around the central peak with respect to the corrected spectrum (orange solid curve).

5 | Chapter 5- Applications of the hyperspectral microscope

In the present Chapter we will show the huge versatility of the FT hyperspectral microscope described so far. Section 5.1 is dedicated to Raman measurements on lithium niobate poled crystals carried out through the YVO_4 detection TWINS, while Section 5.2 presents the results of preliminary tests and measurements on living biological samples obtained with the implemented branch for excitation spectra analysis.

5.1. TWINS in detection

5.1.1. Raman measurements on lithium niobate crystal

Lithium niobate ($LiNbO_3$) is an artificial dielectric and ferroelectric material, that is of particular interest in integrated [89], guided-wave [100] and non-linear [16] optics for pyroelectric, piezoelectric, electro-optic, and photo-elastic properties, which have origin in its trigonal crystal structure [96].

Ferroelectric materials have natural electric polarization that can be reversed by applying an external electric field; this spontaneous polarization vanishes in the so-called *paraelectric phase* that is reached above a phase transition temperature, the *Curie temperature*. $LiNbO_3$ typically exhibits ferroelectric behaviour, since its Curie temperature is quite high (1210° C). In this phase the crystal is a member of C_{6v} group (in Schönflies notation [55, Chapter 8]): it has mirror symmetry about three planes that are 60° apart and a three-fold rotation symmetry about its z-axis (crystallographic axis [0 0 0 1] referred to as c axis in [96]), where it has the highest spontaneous polarization due to the particular stacking of atomic layers.

Similarly to molecules (discussed in Chapter 3), also in the periodic structure of crystals it is possible to describe nuclei dynamics with a quantum mechanical approach: the energy of the collective oscillations of atoms (normal modes) can be quantized; each quantum of energy is a quasi-particle called *phonon*. According to the crystal structure, there can be various branches of phonons: acoustic (A) or optical (O), transverse (T) or longi-

tudinal (L) (whether their displacements are perpendicular or parallel to the direction of the mode propagation vector) [78, Chapter 3].

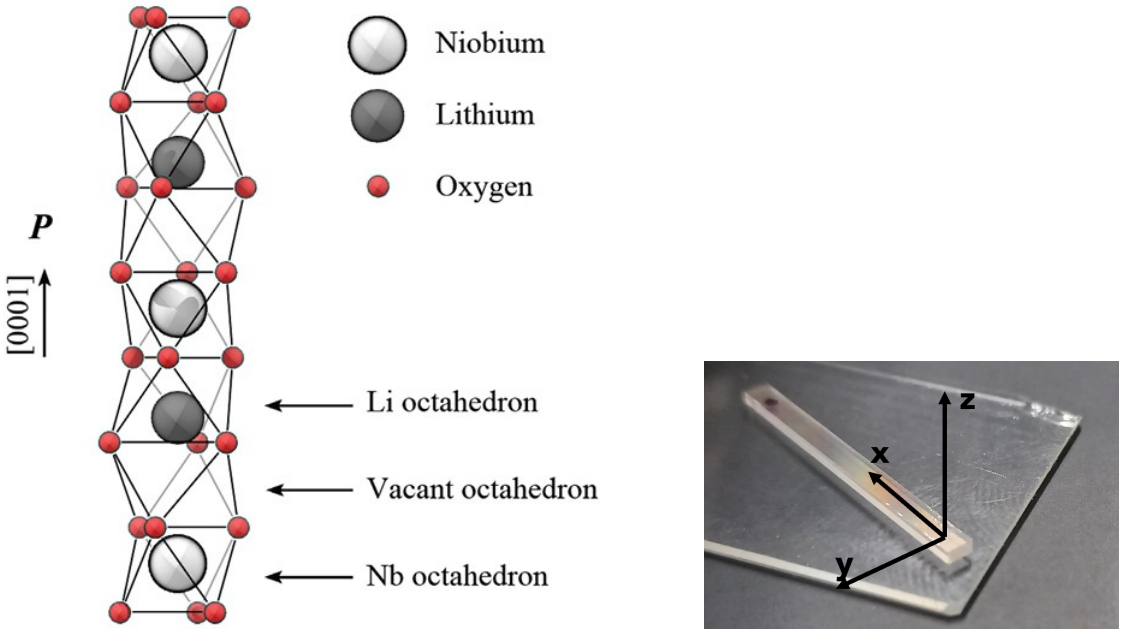

(a) (b)

Figure 5.1: (a) Representation of $LiNbO_3$ crystal structure along the [0 0 0 1] crystallographic axis (*image from [85]).* (b) Picture of the measured crystal above a microscope cover slip with reference axes.

In these measurements we used a 25.19 (x) by 2.00 (y) by 1.00 (z) mm^3 periodically poled lithium niobate crystal (Figure 5.1b) obtained from HC Photonics with period length of 16 μm. The typical technique for periodic poling consists in the application of a strong electric field to the ferroelectric crystal by means of patterned electrodes on the crystal surface, which are usually produced with a photolithographic process. This results in a sequence of ferroelectric domains (separated by the so-called *domain walls*) with reversed orientation, i.e., opposite polarizations. Raman microscopy has been employed to analyze ferroelectric domain structures [84] since frequency and intensity of certain phonons are strongly influenced by propagation direction and polarization of light with respect to the crystal axes, resulting in different Raman spectra. This is evident from Table 5.1, where observable phonon branches are reported for different scattering configurations: a certain incident radiation can stimulate a particular collective motion in the crystal, e.g., E-TO in z-incidence; since the (inelastically) scattered light has a well-defined polarization [78, Chapter 9], also detection polarization is relevant. To identify scattering geometries we use Porto notation $k_i(u_{pol,i}, u_{pol,s})k_s$: k_i, k_s identify the incident and scattered light propagation directions and $u_{pol,i}$, $u_{pol,s}$ the respective polarizations.

Scattering geometry	Phonon branch
$y(x,x)\bar{y}$	A_1-TO+ E-LO
$y(x,z)\bar{y}$	E-TO
$y(z,z)\bar{y}$	A_1-TO
$z(x,x)\bar{z}$	A_1-LO+ E-TO
$z(x,y)\bar{z}$	E-TO
$z(y,y)\bar{z}$	A_1-LO+ E-TO

Table 5.1: Scattering geometries in Porto notation (only for y and z incidence that are explored in this thesis work) and respective observable phonons [85]. A_1, E are irreducible representations of the $LiNbO_3$ symmetry group. TO, LO are transversal and longitudinal optical phonons respectively.

In particular, $z\bar{z}$ ($y\bar{y}$) corresponds to a back-scattering configuration, i.e., $k_i = -k_s$, that were adopted in our measurements.

In our hyperspectral microscope we excited with a CW diode-pumped laser at 532nm (*Cobolt Samba ™ 1000*, maximum power 1W) coupled to the microscope by means of a 400-μm-core multimode fiber. To guarantee a flat-field profile at the fiber tip a mechanical scrambler mixed the modes in the core and averaged out the speckle pattern caused by the spatial coherence of the laser beam. The resulting incident radiation was unpolarized, while the detected light had a precise polarization determined by the first polarizer (P1) of the detection TWINS: referring to spectra in Figure 5.2, the sample was oriented with its x-axis (y-axis, z-axis) parallel to P1 polarization axis to measure x-polarized (y-polarized, z-polarized) Raman signal.

Excitation wavelength	Irradiance	Fiber core	Objective magn./NA	Scan length	Integration time	Gain	Binning
532nm	$11.1\frac{W}{mm^2}$	$400\mu m$	50x/0.80	15.3mm ($5\mu m$ step)	0.6s	0	4

Table 5.2: Parameters for Raman measurements on lithium niobate crystal. The irradiance is the density of radiant flux (power carried by a radiation field) received per unit area. In this case the laser power is 150mW on a uniform circular spot of $\sim 131\mu m$ (the spot diameter is the 82% of the FOV size, that is equal to $160\mu m$ with a 50x objective).

To remove the back-scattered pump at 532nm we used a dichroic beam-splitter *Semrock® LP D02-532RU-25* and a *Semrock® RazorEdge LP03-532RU-25* in the detection path. We managed the fluorescence background by performing a long unilateral acquisition of the

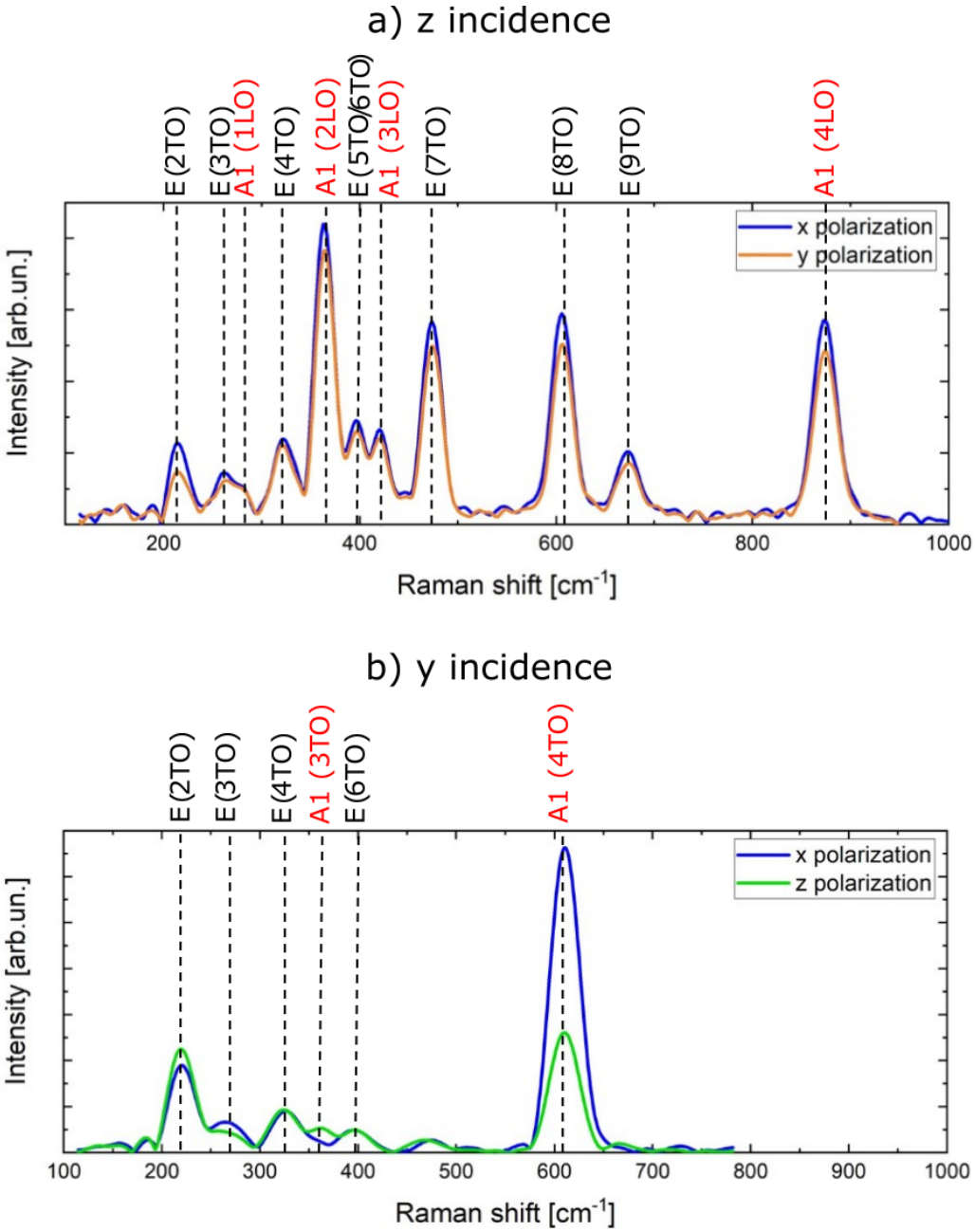

Figure 5.2: Raman spectra for z and y incidence obtained as the mean of a ROI on the crystal surface. Two possible polarizations of scattered light are shown, while incident radiation is unpolarized. The range of interest is 100-1000 cm^{-1} because there is no evidence of higher and lower frequency phonons in literature. Red and black labels refer to A1 and E phonon modes, respectively; the transverse or longitudinal nature of the phonon is indicated in parenthesis.

interferogram with wedge excursion of 15.3mm, which corresponds to a spectral resolution of $\sim$23 cm^{-1} (after Happ-Genzel apodization of the interferogram). Actually, since expected Raman spectra are extended up to 1000 cm^{-1} ($\sim$ 560 nm) and measured photoluminescence signal has a peak around 700 nm, an additional short-pass filter at 600nm, *Thorlabs® FESH0600*, was introduced in detection to reduce detrimental fluorescence contribution.

In Figure 5.2 we have assigned peaks to expected phonons according to theoretical and experimental values reported in [85]. Since our measurements are not polarized-resolved in excitation, we expect to see peaks related to phonons excited by both the orthogonal polarization directions of the incident light, by selecting a specific polarization in detection. In comparison with spectra from literature, where some peaks have been identified only by means of an extensive theory, our fluorescence-background-free technique enabled us to isolate modes (e.g., E(9TO)) without any particular effort. It follows that it can be adopted to address the problem of assignment of some weak phonons that are usually buried in photoluminescence signal and to characterize spatially ferroelectric waveguides faster than a typical raster-scanning approach.

5.2. TWINS in excitation

5.2.1. Preliminary tests: Egyptian blue and cadmium orange

Materials science and biology are important fields of applications of hyperspectral microscopy since emission and excitation spectra allow one to investigate the properties of samples. In this Section we test our microscope capability to perform excitation-resolved measurements. We first present the results obtained from the analysis of a mixture of powders; finally we report measurements on living biological samples.

The powders we investigated are two inorganic pigments: Egyptian blue and cadmium orange. The first is a synthetic pigment made of cuprorivaite ($CaCuSi_4O_{10}$) that was first produced in the 4th Dynasty in Egypt (around 2500 BC) and widely used in the whole Mediterranean basin for centuries [15]. It exhibits a high emission quantum efficiency (10.5%, that can be even tripled by exploiting a new synthesis method presented in [69]) in the near IR region (800-1000nm) with visible excitation. Therefore, nowadays it has been exploited also for energy saving applications [49], [82]. This intense photoluminescence is associated with the electronic transition $^2B_{2g} \rightarrow ^2B_{1g}$ of Cu_{2+} ions in a D_{4h} symmetry [81].

Cadmium orange belongs to a class of yellow and orange pigments based on CdS, introduced during 19^{th} century [35]. To obtain lighter yellows Cd is replaced by Zn, while a deeper orange colour results from the substitution of S with Se. In these IIb-VIa semiconductors absorption consists in the promotion of an electron from valence to conduction band [78, Chapter 6], thus the generation of an electron-hole pair. There can be either a radiative recombination that leads to a narrow emission band with energy close to the energy gap E_g, or an electron trapping in deep trap states follwed by a recombination with holes, that results in the emission of lower energy photons (studies have shown the existence of at least two near IR emission bands associated with these states [8]). These radiative decays show quite different temporal dynamics: the band-edge emission is much faster than the trap state emission [18].

For our measurements ground pigments purchased from Kremer Pigmente GmbH & Co (Germany) were mixed on a microscope cover slip: Egyptian blue and cadmium zinc sulfide yellow No.4 (we refer to it as KP4). They are well-distinguishable both in excitation and emission spectra. Egyptian blue has a broadband absorption at 630nm ($^2B_{1g} \rightarrow ^2E_g$) with other bands at 780nm ($^2B_{1g} \rightarrow ^2B_{2g}$), 536nm ($^2B_{1g} \rightarrow ^2A_{1g}$) [1] and in the UV around 260nm, as recently demonstrated [12]. KP4 band-edge absorption is around 510nm; its emission spectrum overlaps with that of Egyptian blue in the range 800-1000nm, where

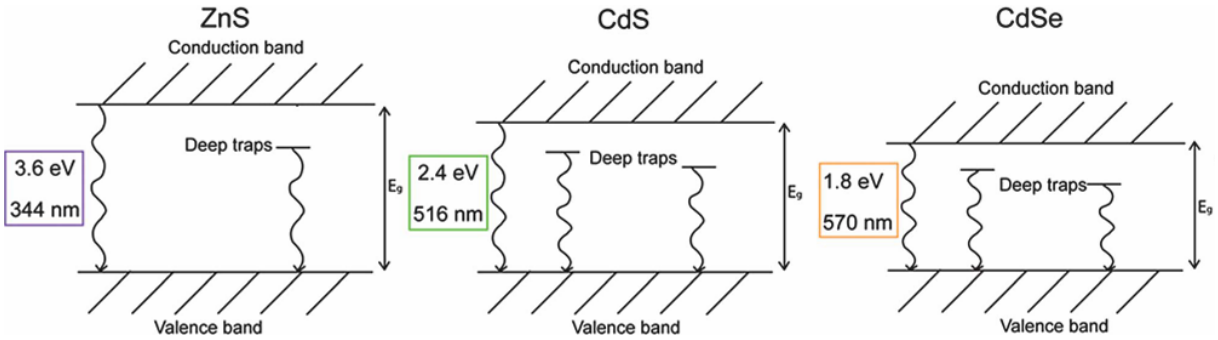

Figure 5.3: Energy diagrams for ZnS, CdS and CdSe: arrows represent both band-edge and trap states emission. Different hues can be obtained by proper substitutions of Cd with Zn or S with Se: they can be considered binary alloys of ZnS and CdS, $Zn_{1-x}Cd_xS$ with $0<x<1$, or CdS and CdSe, CdS_xSe_{1-x} with $0<x<1$, where the resulting energy gap varies proportionally to the composition [78, Chapter 9].

the second trap state emission from KP4 is centered, and differs from it for the first trap state emission at 710nm [18].

To test our set-up capability of discriminating different species on the basis of their excitation spectrum, we compared the results obtained separately from emission and excitation measurements, conducted on the same field of view. In both cases we excited with the halogen lamp (64627 HXL, OSRAM) filtered below 500nm with a *Thorlabs® FESH0500* (resulting spectrum is the light green area in Figure 5.4) and collected fluorescence above 515nm by using a dichroic beam-splitter at 510nm and a 515nm-long-pass filter in detection. Since the expected spectra do not show narrowband spectral features in these ranges, the related interferograms oscillate only at short delays around zero-path-delay position, therefore wedge excursions were bilateral (around the central burst) and short (with respect to the longest ones allowed by wedge translators) for both TWINS interferometers.

	Excitation band (nm)	Detection band (nm)	Fiber core	Objective magn./NA	Scan length	Integration time	Gain	Binning
em.	380-500	515-1000	$400\mu m$	20x/0.5	1mm ($5\mu m$ step)	0.25s	0	4
exc.	380-500	515-1000	$400\mu m$	20x/0.5	1.5mm ($6.5\mu m$ step)	0.9s	0	4

Table 5.3: Parameters for fluorescence emission (first row) and excitation (second row) measurements on mixture of Egyptian blue and KP4. Wedge excursions are bilateral for both TWINS; binning 4 limits the resolution; detection band upper bound is taken where the detector spectral sensitivity decreases to 20%.

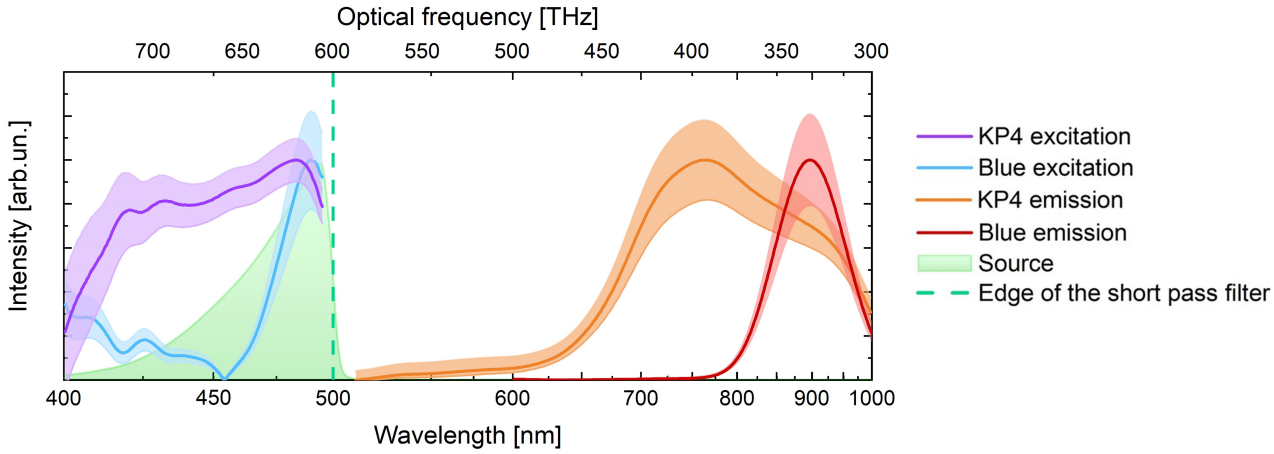

Figure 5.4: Each powder was deposited on a cover slip and analyzed; a ROI was chosen across the observable FOV to compute the average spectrum. Solid lines are normalized mean excitation (purple and blue) and emission (orange and red) spectra. Shaded areas are the wavelength-dependent standard deviations of the spectra. The green area is the source spectrum filtered below 500 nm (vertical dotted line). The abscissa is uniform in frequency and represented also in the more common wavelength unit.

Before analysing the mixture of powders we measured excitation and emission spectra of FOVs with single pigments. The mean spectra of large ROIs across the field of view are reported in Figure 5.4: in agreement with the literature, emission spectra (red and orange solid lines) differ due to the first trap state emission peak at 710nm and KP4 has a stronger absorption than blue in the range 400-500nm. These excitation spectra are the result of normalization on source spectrum: normalization consists in dividing the measured excitation spectrum by the incident radiation. This procedure is necessary to retrieve a real spectrum, because the measured one depends on fluorescence intensity which is proportional to both the optical response of the sample (excitation probability) and the exciting radiation spectral power.

Then, we chose a field of view of the mixture where both Egyptian blue and cadmium yellow grains were present (Figure 5.5): despite the different quantum yields, the retrieved spectra are the same as for the isolated case, therefore the two species can be clearly distinguished both in emission and excitation spectra.

This preliminary test has confirmed our microscope capability of discriminating between different species in the same FOV also on the basis of their excitation spectra. This can have interesting applications especially in the case of materials that differ only for the excitation spectrum, due to a common emission.

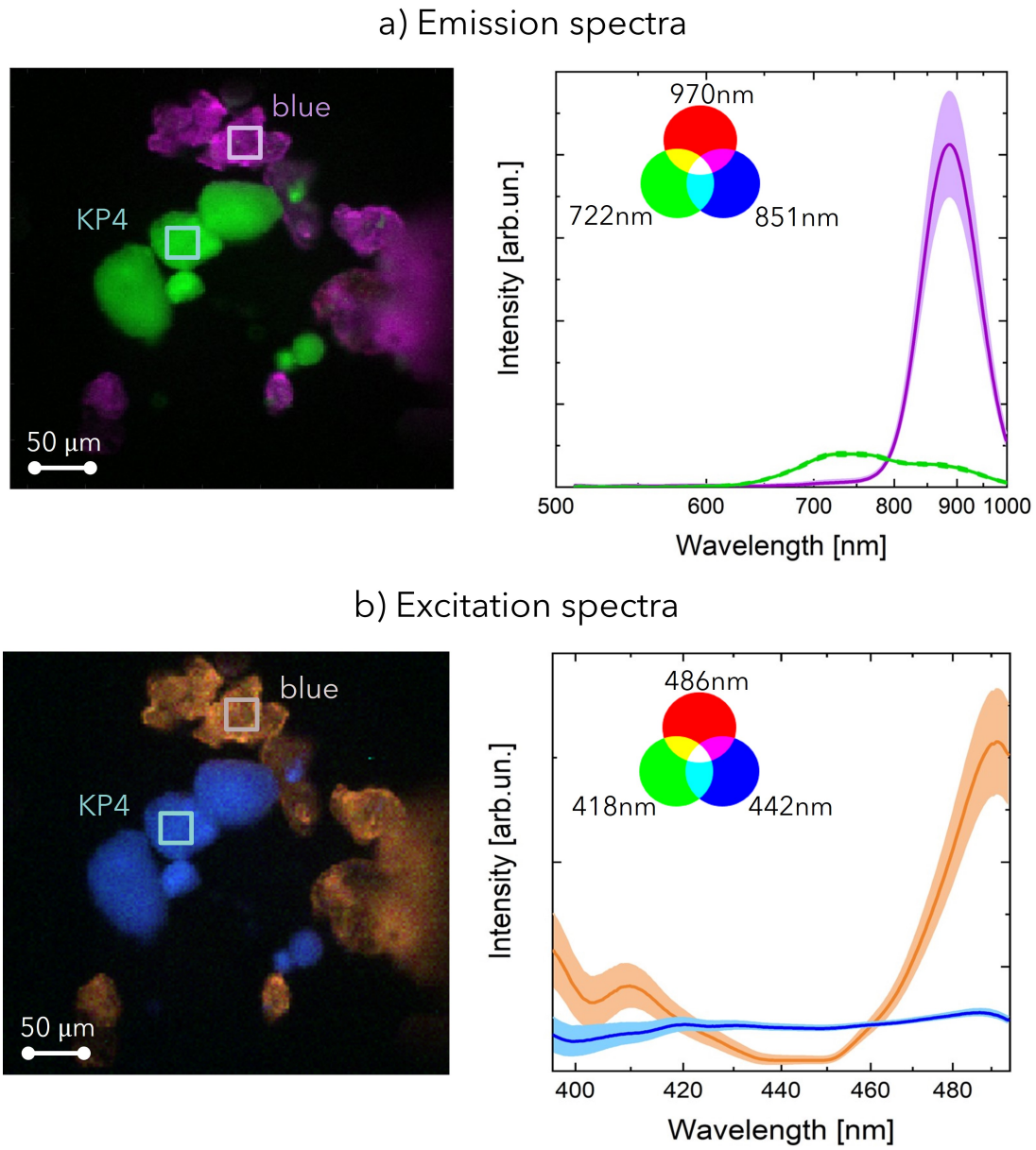

Figure 5.5: Hyperspectral false-colour images of the mixture of pigments and related mean emission (a) and excitation (b) spectra measured in the indicated areas. R,G,B values are calculated by shifting the spectral sensitivities for the three colours to the specified wavelengths. Shaded areas are the wavelength-dependent standard deviations of the spectra. The abscissa is uniform in frequency.

5.2.2. Arabidopsis thaliana: RGECO-1 and Yellow Cameleon

Arabidopsis thaliana is a flowering plant in the mustard family that has become a model organism for the scientific community , as *C. elegans* [33] and *Drosophila* [2], because its genome was completely sequenced [39]. Research on this plant has provided relevant insights into plant biology, for example a deeper understanding of Ca_{2+} ions dynamics, which is involved in various regulatory processes [30]. In particular, in our measurements we focused on cytosolic Ca_{2+} concentration that varies in response to developmental, growth and environmental stimuli. These are commonly referred to as *Ca_{2+} signatures* and they can consist in a single transient increase, with different amplitude and spatio-temporal characteristics, repetitive Ca_{2+} oscillations or concentration gradients [30].

To study these processes in cells and plants, genetically encoded Ca_{2+} indicators (GECIs) have been largely exploited [52]: encoded by a stretch of DNA, they are formed within cells *in situ*, with no addition of any synthetic external compound. Thus, they are very-stable and tolerated by most of cell types. They are categorised into single-fluorescent protein (FP) or two-FP probes, according to the number of fluorescent proteins present in the indicator. In the first type, the binding of Ca_{2+} triggers an intramolecular rearrangement of the protein that alters its fluorescent properties; they are known as *intensiometric* indicators, because the emission intensity at a certain wavelength is typically monitored. The latter are based on a completely different mechanism, that is FRET: after Ca_{2+} binding the two proteins result close enough and properly oriented to see an increase in energy transfer efficiency. Since the ratio of fluorescence intensities of donor and acceptor is generally measured with these indicators, they are defined *ratiometric*.

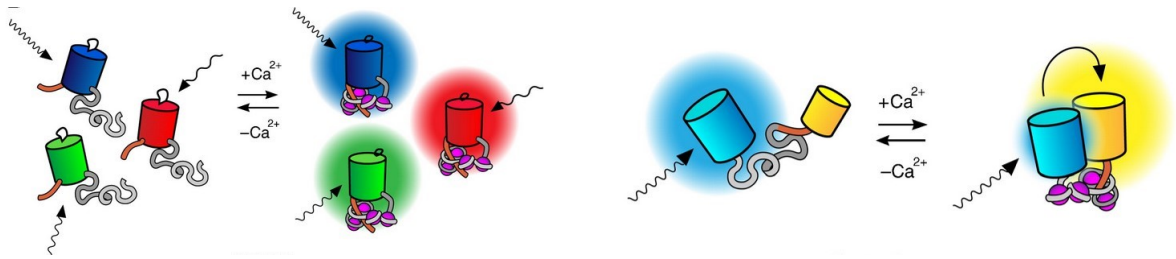

(a) GECOs indicator family. (b) Cameleon indicator family.

Figure 5.6: Pictorial representation of the different mechanisms underlying single-FP and two-FP indicators. (a) Ca_{2+} binding induces a conformational modification of the protein (colours denote fluorescence emission ranges for different available proteins) that changes its optical properties. (b) The intramolecular rearrangements of the two proteins after Ca_{2+} binding lead to a close proximity, allowing FRET to occur. *Image adapted from [52].*

In this Section we report one example for each category; in particular, modifications in the excitation spectra are shown as a consequence of Ca_{2+} concentration variation rather than in fluorescence ones, as reported in [3], [24], [51].

R-GECO in *Arabidopsis thaliana* leaves

Starting from *Aequorea Victoria* green fluorescent protein (GFP), a continuous development of genetically expressed proteins has led to the broad colour palette of fluorescent markers that is available nowadays [27] (colour refers to the emitted radiation). Red FPs have always been of great interest because long wavelengths (1) suffer less scattering in tissues [41, Chapter 11], enabling deeper imaging, (2) induce less autofluorescence and photodamge of the sample.

Photophysical properties of a set of red Ca_{2+} indicators (better known as R-GECIs) have been analyzed in [65]; in particular, we considered the change in the excitation spectrum for the first engineered red GECI, R-GECO1. References [3], [51] showed that an external stimulus (such as mechanical stress, insect herbivory, volatile organic compounds) triggers an increase in Ca_{2+} concentration in *Arabidopsis thaliana* leaves with peculiar spatio-temporal evolution. The consequent change in optical properties of the FP is a blue-shift, from 577 nm to 563 nm, of the excitation peak.

In our measurements the sample consisted of a transgenic *Arabidopsis thaliana* expressing cytosolic RGECO-1. We retrieved the excitation spectrum of the leaf before and after wounding it with tweezers (the same result was obtained for different leaves of the same plant). The excitation source was filtered below 600nm with *Thorlabs®FESH600* and fluorescence emission was collected in a 40nm-bandwidth range centered at 630nm (*OMEGA XF1091* bandpass filter) in order to reduce the overwhelming chlorophyll emission at longer wavelengths [74]. From the parameters reported in Table 5.4 it emerges that we had to find a compromise among low-intensity signal, spatial resolution and scan duration: Ca_{2+} concentration increases immediately after the mechanical stimulus, as a defence response of the plant, and returns to its basal value after some minutes. Since our measurement has to be performed in stationary conditions, i.e., fluorescence signal has to be constant in intensity, we had to limit the scan time, even if a longer integration time would have increased the signal-to-noise ratio. To detect higher signal we then exploited both gain and high binning, at cost of reducing spatial resolution.

Excitation band (nm)	Detection band (nm)	Fiber core	Objective magn./NA	Scan length	Integration time	Gain	Binning
380-600	610-650	400μm	10x/0.30	1.5mm (10μm step)	1.5s	10	6

Table 5.4: Parameters for excitation measurements in *Arabidopsis thaliana* leaves with genetically encoded R-GECO1.

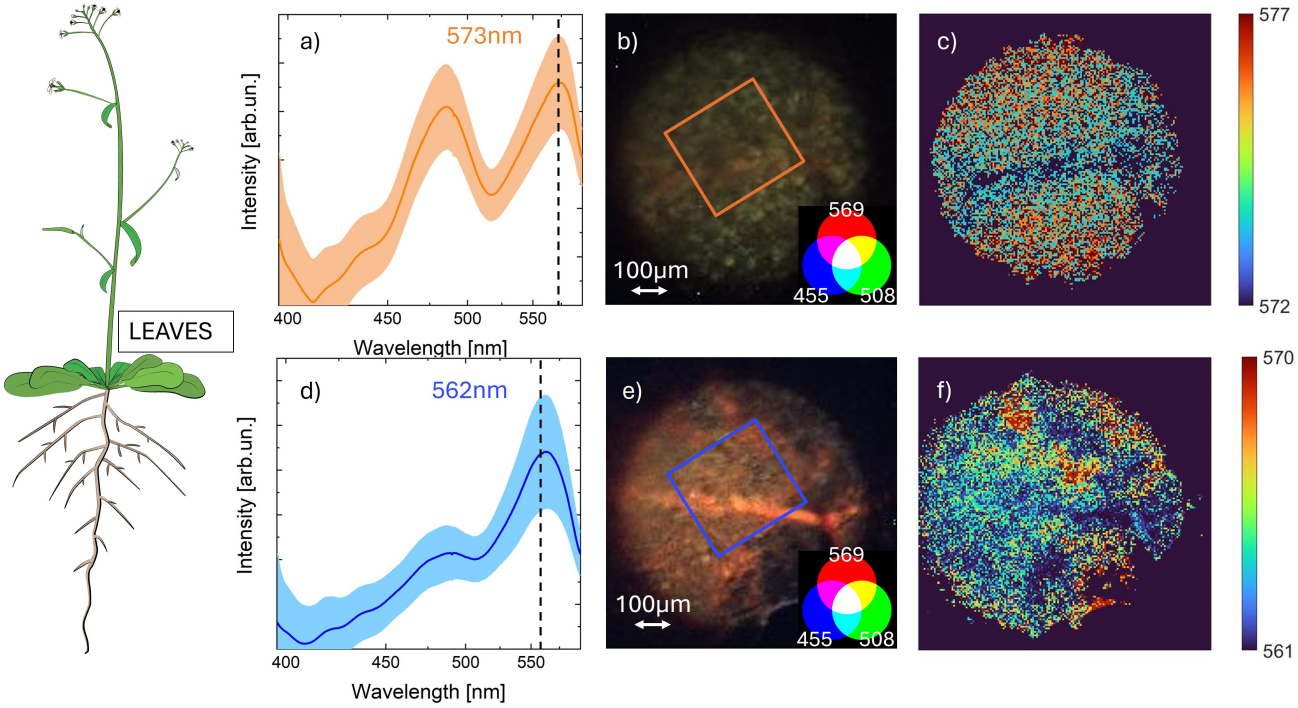

Figure 5.7: Schematic *Arbidopsis thaliana* with box indicating the measured leaves and relative results before (a,b,c) and after (d,e,f) wounding. (a,d) are the mean spectra in the regions indicated with squares; shaded areas are the wavelength-dependent standard deviations of the spectra; the abscissa is uniform in frequency. (b,e) are false-colour RGB (167x167 pixels) images synthesized from the hyperspectral cube for R,G,B sensitivities in the range (400,600)nm centered at the reported wavelengths (in nm). (c,f) are spectral peak maps. The colorbars indicate the peak wavelength expressed in nm.

Figure 5.7 summarises the results: for a leaf at rest (a,b,c) Ca_{2+} concentration is "low" (*Ca_{2+}-free* condition), therefore the average peak position across the whole FOV is at 573nm, while it is blue-shifted to 562nm after mechanical stress (d,e,f) (*Ca_{2+}-saturated* condition). The widefield configuration allowed us to observe also slight disuniformities especially between the midrib and lamina in resting leaf: the spectral peak map in 5.7c reveals a blue-shifted peak in correspondence of the central region of the leaf (where midrib was located). This feature is not surprising since the midrib typically shows higher Ca_{2+} concentration than the peripheral regions, even without stress.
The main difference with respect to RGECO-1 spectra reported in literature lies in the peak in the range (450,500)nm, that is due to chlorophyll.

Cameleon in *Arabidopsis thaliana* roots

One of the most common FRET probes is the Yellow Cameleon YC3.6 which involves the FRET couple CFP-cpVenus (cyan and yellow fluorescent proteins, respectively), that

are specifically engineered to increase energy transfer efficiency in presence of Ca_{2+} [68]. A typical approach for quantitative FRET measurements consists in measuring the ratio between the emission peak intensities of the donor in presence (F_{DA}) and absence (F_D) of the acceptor; it can be shown [56, Chapter 13] that it is related to the transfer efficiency E, defined as the fraction of photons absorbed by the donor that contribute to the acceptor emission, by the formula

$$E = 1 - \frac{F_{DA}}{F_D} \tag{5.1}$$

The same equation holds when intensities are replaced with lifetimes, τ_{DA} and τ_D, under the same conditions.

Alternatively, other quantities can be taken as indicative of resonance energy transfer, e.g., the ratio of the emission intensities of donor and acceptor. Since a partial spectral overlap between excitation (emission) spectra of the proteins is unavoidable for a FRET couple, the main problems that arise when dealing with intensities are: the *donor spectral bleedthrough*, that is donor emission in the spectral range in which acceptor emission is expected; the *cross excitation*, that consists in exciting acceptor fluorophores directly with the incident radiation. One way to circumvent these issues is linear unmixing: this algorithm divides the acquired (emission or excitation) spectrum into two distinct contributions from donor and acceptor independently, i.e., it retrieves the contributions of each protein such that their linear combination results in the experimental spectrum [20], [21], [67].

In the specific case study of *Arabidopsis thaliana* roots, reference [24] shows that (1) FRET signal is more intense in correspondence of primary root tip (where growth takes place [31]) and (2) it is even more evident immediately after an external stimulus.

	Excitation band (nm)	**Detection band (nm)**	**Fiber core**	**Objective magn./NA**	**Scan length**	**Integration time**	**Gain**	**Binning**
root a	380-550	590-1000	400μm	10x/0.3	1.5mm (10μm step)	1.5s	5	6
root b	380-550	590-1000	400μm	20x/0.5	1.5mm (10μm step)	2s	0	6

Table 5.5: Parameters for excitation measurements in *Arabidopsis thaliana* roots with genetically encoded YC3.6. The two rows refer to different roots of the same plant (a,b in Figure 5.10).

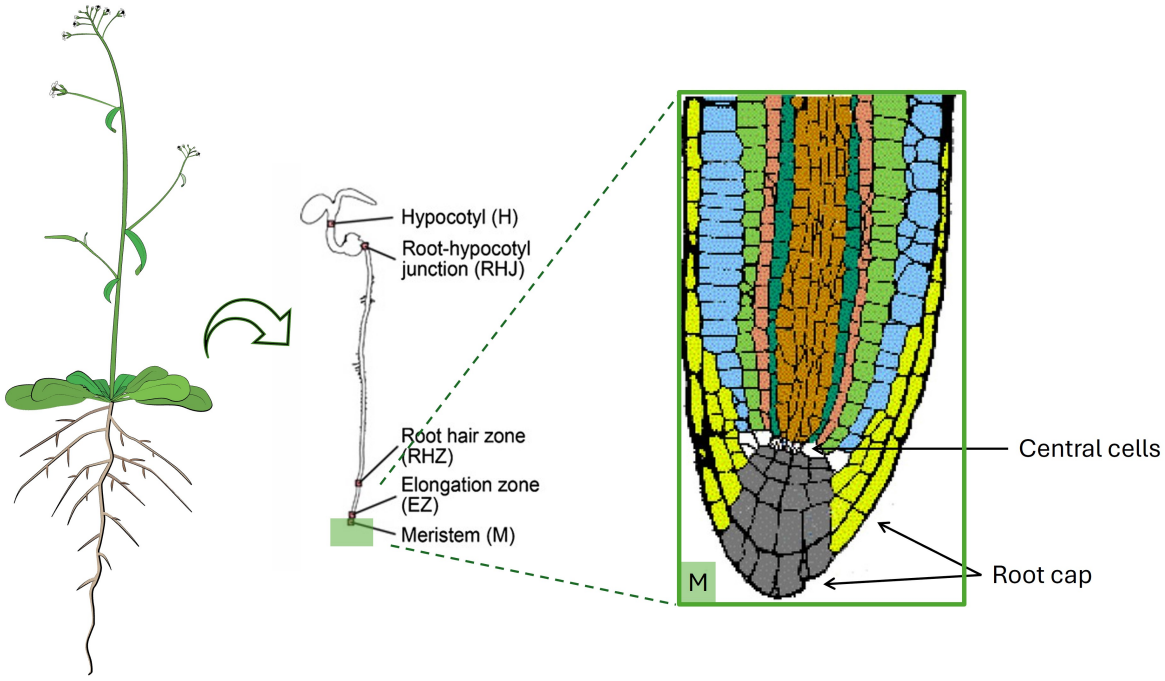

Figure 5.8: Organization of tissues in *Arabidopsis thaliana* root: the meristematic zone (M) of the root is responsible for plant growth; a zoom of the median longitudinal section of the root tip reveals a layered organization of tissues. *Images adapted from [24], [31].*

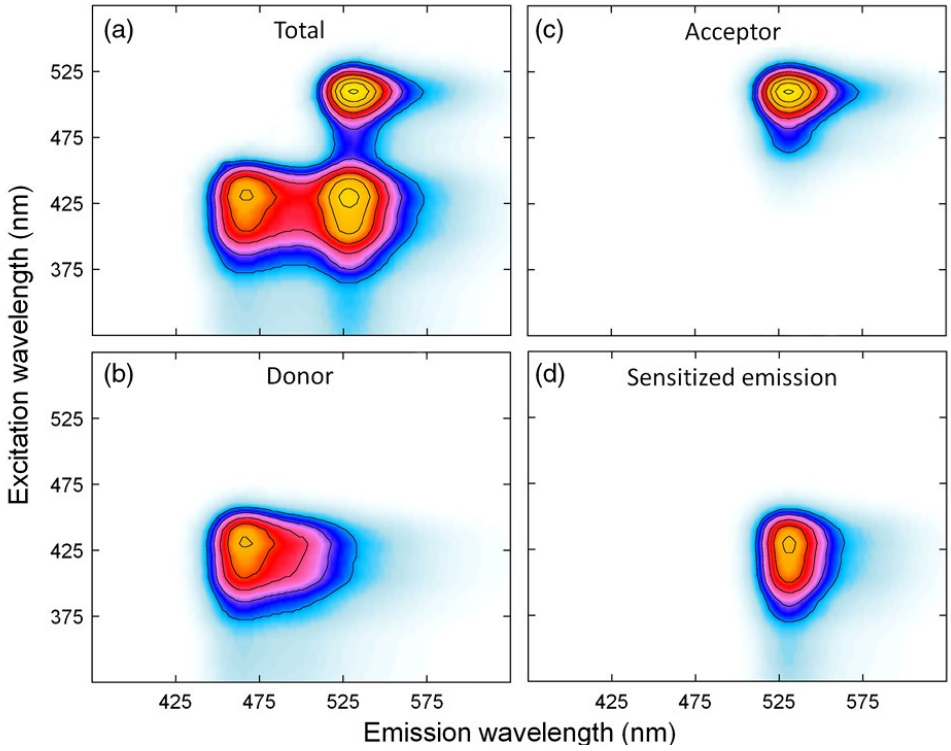

Figure 5.9: Excitation-emission matrix for FRET couple CFP/cpVenus and its unmixing into isolated donor (b) and acceptor (c) contributions and their cross-peak (d). The latter is the FRET signature. *Image from [67].*

Rather than emission intensities, we measured variations in the excitation spectra across the FOV [87]: where acceptor fluorescence increases due to energy transfer, i.e., at root tip, we expect an increased intensity of the donor excitation spectrum. An excitation-emission matrix for CFP and cpVenus can make the concept clearer (Figure 5.9). With an excitation source filtered below 550nm with a *Thorlabs® FESH550* we always excite both proteins; detecting fluorescence above 590nm, we expect to see the acceptor excitation spectrum peaked at 515nm (provided that the acceptor is homogeneously distributed in the sample), but the donor contribution only when FRET takes place, because we are not collecting photons emitted directly from the donor, whose emission peak is at much lower wavelength (477nm). In other words, with our choice of filters, the acceptor is always directly excited by the source, so its fluorescence is collected everywhere in the root, while the donor contribution to fluorescence in this range is detected only in presence of energy transfer, therefore CFP excitation peak at 434nm is measured only with FRET.

Our sample consisted of a transgenic *Arbidopsis thaliana* seedlings, expressing the cytosolic YC3.6; they are kept in a nourishing solution inside a Petri dish, that is directly placed on the sample stage of our microscope. Using a 20x-magnification objective we could observe the root tip as shown in the longitudinal section of Figure 5.8. In the false-colour RGB images of Figure 5.10 we can clearly discriminate between regions where the acceptor excitation peak prevails (reddish) and those with a relevant contribution from the donor (yellowish). This result is in agreement with the previous discussion: in the final part of the meristem, immediately above the root cap, calcium ions are more concentrated, which implies a higher FRET signal with respect to inner regions; this corresponds to a more relevant donor (CFP) contribution in the excitation spectrum.

Table 5.5 reports the measurement parameters: gain and high binning were necessary to detect a sufficiently intense signal from the sample; in this case we were not limited by any fast temporal dynamics, therefore we could exploit a quite long exposure time per frame, still maintaining the measurement time of just a few minutes.

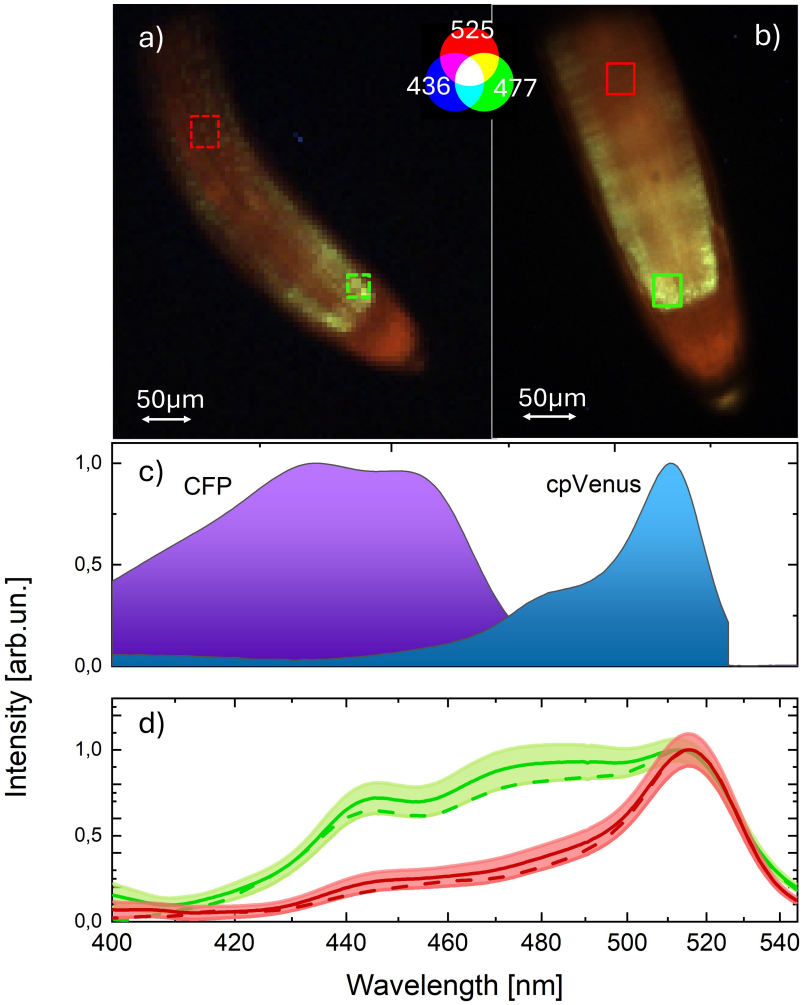

Figure 5.10: (a, b) False-colour RGB images of two different *Arabidopsis thaliana* roots, synthesized from the hyperspectral cubes for R,G,B sensitivities in the range (400,550)nm centered at the reported wavelengths (in nm). (c) Normalized reference excitation spectra for isolated CFP and cpVenus (data from online database *FPbase*, [46], [54]). (d) Mean spectra of the ROIs indicated with squares in (a,b): dotted lines are for root in (a); solid lines and shaded areas (for the wavelength-dependent standard deviations of the spectra) refer to root in (b). The abscissa is uniform in frequency.

A | Classical description of Raman scattering

In a quantum mechanical description [7, Chapter 10] the molecule is described through a wavefunction ψ that depends on the spatial coordinates of the nuclei and the electrons. Due to the great difference in masses between nuclei and electrons, Born-Oppheneimer approximation assumes that nuclear motion can be treated separately from the electronic problem.

Considering only the nuclei it is possible to describe their motion by solving the eigenvalue equation of the Hamiltonian associated to a harmonic oscillator: a normal mode is a collective motion of the atoms in which nuclei vibrate around their equilibrium positions with a characteristic frequency of oscillation, ν_V. Vibrational levels of the system are equispaced by the quantum of energy $h\nu_V$. Not all the transitions between vibrational states are allowed: energy separation between initial and final states is equal to the quantum of energy $h\nu_V$. This implies that incident photons at ν_0 will undergo an energy increase or decrease of $h\nu_V$ after interaction with the system. These selection rules are based on the molecular response to an applied electric field $\mathcal{E}(t) = \mathcal{E}_\prime \, cos(2\pi\nu_0 t)$ and can be appreciated also by means of a classical argument. Consider the induced dipole moment μ(t) which depends on the electrical polarizability α according to

$$\mu = \alpha\mathcal{E}(t) \tag{A.1}$$

If the polarizability changes periodically around its average value α_0 at a frequency ν_V, due to molecular vibrations at this frequency, the resulting dipole is

$$\begin{aligned} \mu(t) = \alpha_0 \, \mathcal{E}_\prime \, cos(2\pi\nu_0 t) + \Delta\alpha \, cos(2\pi\nu_V t) \, \mathcal{E}_\prime \, cos(2\pi\nu_0 t) = \\ \alpha_0 \, \mathcal{E}_\prime \, cos(2\pi\nu_0 t) + \frac{1}{2}\Delta\alpha \, cos(2\pi(\nu_0 + \nu_V)t) \, \mathcal{E}_\prime + \frac{1}{2}\Delta\alpha \, cos(2\pi(\nu_0 - \nu_V)t) \, \mathcal{E}_\prime \end{aligned} \tag{A.2}$$

Since the radiation generated by an oscillating dipole moment has the same frequency as the oscillation [41, Chapter 11], photons with incident frequency ν_0 (Rayleigh line), $\nu_0 + \nu_V$ (Stokes line) and $\nu_0 - \nu_V$ (anti-Stokes line) are emitted, provided that $\Delta\alpha \neq 0$.

B | Semiclassical model for excitation-resolved measurements

To better understand the principle of excitation-resolved measurements, we can focus on the effect of a single frequency component on the sample [44, Chapter 2].

In a semiclassical approach, radiation is treated classically with Maxwell's equations, while energy levels of the system are described quantum mechanically as quantized levels. Precisely,

$$\overrightarrow{E(t,\vec{r})} = \vec{A}\ cos(-2\pi\nu t + \vec{k}\cdot\vec{r} + \phi) = A\ \overrightarrow{u_{pol}}\ cos(-2\pi\nu t + \vec{k}\cdot\vec{r} + \phi) \tag{B.1}$$

is the incident electric field with frequency ν, wavevector $\vec{k}$, phase ϕ and polarization versor $\overrightarrow{u_{pol}}$.

The system (e.g. a molecule) is a 2-level system whose generic state $|\psi_0>$ is given by the superposition of unperturbed states $|\phi_0>, |\phi_1>$ (eigenvectors of the unperturbed Hamiltonian $\hat{H}_0$)

$$|\psi_0(t,\vec{r})> = c_0|\phi_0(t,\vec{r})> + c_1|\phi_1(t,\vec{r})> = c_0|u_0(\vec{r})> e^{-i\frac{\epsilon_0}{\hbar}t} + c_1|u_1(\vec{r})> e^{-i\frac{\epsilon_1}{\hbar}t} \tag{B.2}$$

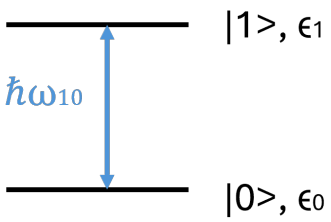

Figure B.1: Schematic of a 2-level system. Eigenstates $|u_0>, |u_1>$ are indicated with a simpler (but equivalent) notation.

with energy ϵ_0 and ϵ_1 respectively, such that $\frac{\epsilon_1-\epsilon_0}{\hbar} = \frac{\epsilon_{10}}{\hbar} = \omega_{10}$ is the (angular) *resonant frequency* of the system. In the *dipole* approximation, i.e., the system dimension is negligible with respect to the electric field wavelength, we can consider only the temporal evolution of the field in the position of the system itself ($\overrightarrow{r_0} = \overrightarrow{0}$, $\phi = 0$ without loss of generality)

$$\overrightarrow{E(t)} = \overrightarrow{A}\ cos(2\pi\nu t) = A\ \overrightarrow{u_{pol}}\ cos(2\pi\nu t) \tag{B.3}$$

This interaction is described with a perturbation term $\hat{H}_1$ in the Hamiltonian, that represents the energy of the electric dipole $\overrightarrow{\mu}$ associated with the system within the electric field

$$\hat{H}_1 = -\hat{\overrightarrow{\mu}} \cdot \overrightarrow{E} \tag{B.4}$$

Time-dependent Schrödinger equation governs the temporal evolution of the eigenstates $|\psi>$ of the perturbed system

$$i\hbar\frac{\partial|\psi>}{\partial t} = (\hat{H}_0 + \hat{H}_1)|\psi> \tag{B.5}$$

obtaining

$$|\psi>= c_0(t)|\phi_0> + c_1(t)|\phi_1> \tag{B.6}$$

where a temporal dependence of coefficient c_0 and c_1 appears (this is true only when dealing with small perturbations of the initial Hamiltonian, since this is the necessary condition for perturbation theory).
Replacing (B.6) in (B.5), we obtain the coupled equations that govern coefficient temporal evolution

$$\begin{cases} \dfrac{\partial c_O}{\partial t} = \dfrac{i}{\hbar} < u_0|\hat{\overrightarrow{\mu}}|u_1 > \cdot \overrightarrow{E}\, c_1 e^{-i\omega_{10}t} \\ \dfrac{\partial c_1}{\partial t} = \dfrac{i}{\hbar} < u_1|\hat{\overrightarrow{\mu}}|u_0 > \cdot \overrightarrow{E}\, c_0 e^{+i\omega_{10}t} \end{cases} \tag{B.7}$$

and writing explicitly the field

$$\begin{cases} \dfrac{\partial c_0}{\partial t} = \dfrac{i}{\hbar} < u_0|\mu_\parallel|u_1 > A\ cos(2\pi\nu t)\ c_1\ e^{-i\omega_{10}t} \\ \dfrac{\partial c_1}{\partial t} = \dfrac{i}{\hbar} < u_1|\mu_\parallel|u_0 > \ A\ cos(2\pi\nu t)\ c_0\ e^{+i\omega_{10}t} \end{cases} \tag{B.8}$$

where $\mu_\parallel$ represents the projection of the dipole moment $\overrightarrow{\mu}$ along the field polarization direction.
When of $2\pi\nu \sim \omega_{10}$, it can be shown that the system wavefunction is

$$|\psi>= \tilde{c_0}|u_0> e^{-i\frac{\epsilon_0}{\hbar}t} + i\tilde{c_1}|u_1> e^{-i\frac{\epsilon_1}{\hbar}t} \tag{B.9}$$

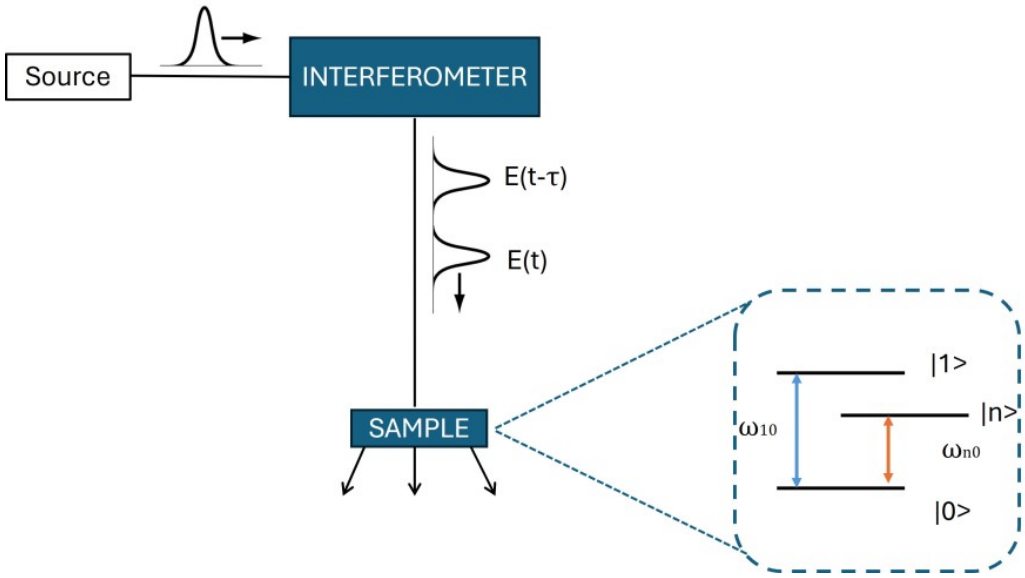

Figure B.2: Working principle of Fourier transform excitation spectroscopy: the sample, described as a 3-level system in the insert, is excited by the two delayed replicas of a source field generated with an interferometer.

where $c_0 = \tilde{c_0}$, $c_1 = i\tilde{c_1}$ with $\tilde{c_0}, \tilde{c_1}$ real numbers (i represents the phase shift of the rotating wavefunction): the field has created a non-equilibrium charge distribution in the sample that is the physical origin of a macroscopic polarization $\overrightarrow{P(t)}$. Classical definition of polarization is $\overrightarrow{P(t)} = N < \overrightarrow{p} >$, with N atoms/molecules per unit volume and $< \overrightarrow{p} >$ average electric dipole moment. In quantum mechanics, it then becomes

$$\begin{aligned}\overrightarrow{P(t)} &= N < \hat{\overrightarrow{\mu}} >= N < \psi|\hat{\overrightarrow{\mu}}|\psi >= \\ &= \tilde{c_0}\tilde{c_1} < u_0|\hat{\overrightarrow{\mu}}|u_1 > \sin(\omega_{10}t) \sim \\ &\propto + < u_0|\hat{\overrightarrow{\mu}}|u_1 >^2 sin(\omega_{10}t)\end{aligned} \tag{B.10}$$

According to Maxwell's equations, oscillating charges create an electromagnetic wave, *free induction decay (FID)*, that is $\frac{\pi}{2}$-phase shifted with respect to the macroscopic polarization [41, Chapter 11]

$$E_{FID} \propto - < u_0|\hat{\overrightarrow{\mu}}|u_1 >^2 cos(\omega_{10}t) \tag{B.11}$$

In the specific case of a field resonant with the 2-level system, i.e., $\nu = \omega_{10}$, this signal interferes with the incident radiation (Equation B.3) giving destructive interference: resulting field has a lower intensity than the initial one, therefore E is absorbed by the sample. Hence, absorption is the result of a double interaction with the field: the first creates a polarization that is the source of the emitted field E_{FID} ; the second consists in the interference between E_{FID} and the incident radiation.

This absorption can be measured by means of a spectrometer: the spectrum of the total field E_{FID}+E is

$$S(\omega) = |FT(E_{FID}+E)|^2 = \left| \int_{-\infty}^{+\infty} (E_{FID}+E)\cdot e^{i2\pi\nu t}\,dt \right|^2 = \\ = S_{FID} + S_0 + 2\Re\left[\int_{-\infty}^{+\infty} E_{FID}\cdot e^{i2\pi\nu t}\,dt \cdot \left(\int_{-\infty}^{+\infty} E\cdot e^{i2\pi\nu t}\,dt \right)^* \right] \tag{B.12}$$

with S_0 and S_{FID} spectra of the incident field and generated signal, respectively.

The absorbance is then defined as

$$A(\omega) \equiv -log\left(\frac{S(\omega)}{S_0} \right) \tag{B.13}$$

With this definition, if a delta-like field is sent on the sample, a typical Lorentzian absorption line can be retrieved, by adopting the density matrix formalism to describe the sample [44, Chapter 4]. However, to extract the excitation spectrum it is necessary to introduce a delayed replica $E(t-\tau)$ of the field $E(t)$: the signal emitted by the system E_{FID}, as a result of the induced polarization, interferes with both replicas. When $\tau = 0$ there is the expected destructive interference, i.e., the field is absorbed and the 2-level system is excited; but when a π shift is introduced (i.e. $\tau = \frac{1}{2\nu}$) a constructive interference is observed between E_{FID} and the delayed replica, that implies no absorption by the system (i.e., it is in its ground state). In other words, by tuning the delay τ between two replicas of a field resonant with the system, we can induce a modulation in its state with a period $\frac{1}{\nu} = \frac{2\pi}{\omega_{10}}$; consequently, also the emitted light at ω_{10} shows the same temporal oscillation with τ. On the contrary, a non-resonant field cannot interact with the system, so no emission can be detected.

Generalizing this description to a more (realistic) complex system, for example with three levels (|0> and |1> that decays rapidly to an intermediate |n> as in Figure B.2): by temporally modulating the incident resonant field, we expect a modulation with the same period of the emission from |n> at ω_{n0}; this means that the modulation of fluorescence signal carries information about the absorbed frequencies.

Conclusions and future developments

In this thesis work we described the great versatility of a widefield Fourier transform hyperspectral microscope based on a common-path birefringent interferometer (TWINS). Starting from an upgraded commercial microscope that enables us to perform Raman, fluorescence emission, reflectance and transmission measurements [4], we implemented an additional illumination path for excitation imaging. An incoherent white source is coupled to a TWINS interferometer and then into the microscope via an optical fiber; a delay scan of the interferometer provides a modulated illumination on the sample, whose fluorescence intensity is collected by an open band 2D detector for each motor position; after the acquisition of the temporal hypercube, a Fourier transform operation gives the excitation spectrum of the sample for each pixel of the field of view.

The measurements described in Chapter 5 validated the system capability of retrieving excitation spectra as well as emission and Raman spectra. Some preliminary tests were conducted to compare the results of the new excitation approach with those obtained through the well-established TWINS in detection. Two examples with biological samples were discussed to highlight one possible application of the technique for discriminating amongst fluorescent species in the biomedical field.

As pointed out, coupling a completely incoherent light source with the TWINS required some effort; the adopted configuration provides a high degree of collimation of the beam through the interferometer, which guarantees a high fringe contrast on the sample plane. This excitation path results cost-effective, since a low-cost white lamp is adopted for illumination, and versatile, thanks to the fiber coupling into the microscope that allows us to replace the modulated source with a different one (e.g., a laser) in a few minutes. However, to really exploit the potentiality of our multimodal microscope for excitation-resolved measurements, the signal-to-noise ratio should be increased. Since the TWINS in detection is not used in excitation spectra measurements and introduces significant power losses, a module with two exit ports could be designed for the detection path of the microscope: only a monochrome low-noise camera, for excitation measurements, and the TWINS, for emission ones. Moreover, higher power could be provided on the sample plane, if the incoherent source were replaced with a supercontinuum laser characterised by higher brightness and lower divergence; of course, this would increase the costs considerably.

With this optimization, the integration time would be shorter, opening the way to the analysis of fast time-dependent processes. We could shorten the acquisition time even further by proper undersampling.

Only qualitative results have been reported, but some case studies may be suitable also for a quantitative analysis, e.g., the determination of either the abundances of different fluorophores in the sample or the Förster energy transfer efficiency, as reported in [20].

Acknowledgements

I would like to thank my advisors Gianluca Valentini and Cristian Manzoni for their passion and precision in explaining all I needed to carry out this work, their patience in answering all my questions and their support also before the thesis work itself when I was really uncertain about the thesis topic that I would have chosen.

I acknowledge PhD students Matteo Corti and Benedetto Ardini who addressed all my doubts, even when they were not physically present in the laboratory, and shared their dedication and interest in this research field. Also Giorgia Tortora, the *wounding girl*, was really helpful in the last period of the work when I needed to measure leaves, roots and any sort of plant. Naturally, I must thank, even if without listing all their names, the other PhD students and researchers who did not work with me directly, but always made me laugh and relax during lunch breaks.

This work was just the last period of a long, intense and fascinating study program. I am very grateful to my dear mates who shared passion and interest in the courses, but also anxiety before the exams, joy and satisfaction after good results. In particular: Marta, for our long question sessions to understand as deeply as possible the lessons and to support each other during exam preparation and for our few but intense music sessions; Fabio and Erika, for our laughs, discussions and exotic experiences.

Finally, I thank my parents for their constant and precious support in any situation during all these years.

Bibliography

[1] G. Accorsi, G. Verri, M. Bolognesi, N. Armaroli, C. Clementi, C. Miliani, and A. Romani. The exceptional near-infrared luminescence properties of cuprorivaite (egyptian blue). *Chemical Communications*, (23):3392–3394, 2009.

[2] M. D. Adams, S. E. Celniker, R. A. Holt, C. A. Evans, J. D. Gocayne, P. G. Amanatides, S. E. Scherer, P. W. Li, R. A. Hoskins, R. F. Galle, et al. The genome sequence of drosophila melanogaster. *Science*, 287(5461):2185–2195, 2000.

[3] Y. Aratani, T. Uemura, T. Hagihara, K. Matsui, and M. Toyota. Green leaf volatile sensory calcium transduction in arabidopsis. *Nature Communications*, 14(1):6236, 2023.

[4] B. Ardini, A. Bassi, A. Candeo, A. Genco, C. Trovatello, F. Liu, X. Zhu, G. Valentini, G. Cerullo, R. Vanna, et al. High-throughput multimodal wide-field fourier-transform raman microscope. *Optica*, 10(6):663–670, 2023.

[5] B. Ardini, M. Corti, M. Ghirardello, A. Di Benedetto, L. Berti, C. Cattò, S. Goidanich, G. Sciutto, S. Prati, G. Valentini, et al. Enhancing hyperspectral imaging through macro and multi-modal capabilities. *Journal of Physics: Photonics*, 6(3):035013, 2024.

[6] S. Aryal, Z. Chen, and S. Tang. Mobile hyperspectral imaging for material surface damage detection. *Journal of Computing in Civil Engineering*, 35(1):04020057, 2021.

[7] P. W. Atkins and R. S. Friedman. *Molecular quantum mechanics*. Oxford University Press, USA, 2011.

[8] V. Babentsov, J. Riegler, J. Schneider, O. Ehlert, T. Nann, and M. Fiederle. Deep level defect luminescence in cadmium selenide nano-crystals films. *Journal of crystal growth*, 280(3-4):502–508, 2005.

[9] C. Bai, J. Li, Y. Xu, H. Yuan, and J. Liu. Compact birefringent interferometer for fourier transform hyperspectral imaging. *Optics express*, 26(2):1703–1725, 2018.

[10] R. Bell. *Introductory Fourier transform spectroscopy*. Elsevier, 2012.

[11] E. Ben-Dor, D. Schläpfer, A. J. Plaza, and T. Malthus. Hyperspectral remote sensing. *Airborne measurements for environmental research: Methods and instruments*, pages 413–456, 2013.

[12] L. Binet, J. Lizion, S. Bertaina, and D. Gourier. Magnetic and new optical properties in the uv–visible range of the egyptian blue pigment cuprorivaite cacusi4o10. *The Journal of Physical Chemistry C*, 125(45):25189–25196, 2021.

[13] M. Born and E. Wolf. *Principles of optics: electromagnetic theory of propagation, interference and diffraction of light*. Elsevier, 2013.

[14] D. Brida, C. Manzoni, and G. Cerullo. Phase-locked pulses for two-dimensional spectroscopy by a birefringent delay line. *Optics letters*, 37(15):3027–3029, 2012.

[15] A. Burmester. Artists' pigments. a handbook of their history and characteristics, volume 3, 2000.

[16] R. L. Byer. Quasi-phasematched nonlinear interactions and devices. *Journal of Nonlinear Optical Physics & Materials*, 6(04):549–592, 1997.

[17] A. Candeo, B. Nogueira de Faria, M. Erreni, G. Valentini, A. Bassi, A. M. de Paula, G. Cerullo, and C. Manzoni. A hyperspectral microscope based on an ultrastable common-path interferometer. *APL photonics*, 4(12), 2019.

[18] A. Cesaratto, C. D'Andrea, A. Nevin, G. Valentini, F. Tassone, R. Alberti, T. Frizzi, and D. Comelli. Analysis of cadmium-based pigments with time-resolved photoluminescence. *Analytical Methods*, 6(1):130–138, 2014.

[19] D. Chase. Phase correction in ft-ir. *Applied spectroscopy*, 36(3):240–244, 1982.

[20] K. Chen, R. Yan, L. Xiang, and K. Xu. Excitation spectral microscopy for highly multiplexed fluorescence imaging and quantitative biosensing. *Light: Science & Applications*, 10(1):97, 2021.

[21] K. Chen, W. Li, and K. Xu. Super-multiplexing excitation spectral microscopy with multiple fluorescence bands. *Biomedical Optics Express*, 13(11):6048–6060, 2022.

[22] P. Connes. Early history of fourier transform spectroscopy. *Infrared Physics*, 24 (2-3):69–93, 1984.

[23] J. W. Cooley and J. W. Tukey. An algorithm for the machine calculation of complex fourier series. *Mathematics of computation*, 19(90):297–301, 1965.

[24] A. Costa, A. Candeo, L. Fieramonti, G. Valentini, and A. Bassi. Calcium dynamics in root cells of arabidopsis thaliana visualized with selective plane illumination microscopy. *PLoS One*, 8(10):e75646, 2013.

[25] C. Cucci, J. K. Delaney, and M. Picollo. Reflectance hyperspectral imaging for investigation of works of art: old master paintings and illuminated manuscripts. *Accounts of chemical research*, 49(10):2070–2079, 2016.

[26] L. M. Dale, A. Thewis, C. Boudry, I. Rotar, P. Dardenne, V. Baeten, and J. A. F. Pierna. Hyperspectral imaging applications in agriculture and agro-food product quality and safety control: A review. *Applied Spectroscopy Reviews*, 48(2):142–159, 2013.

[27] R. N. Day and M. W. Davidson. The fluorescent protein palette: tools for cellular imaging. *Chemical Society Reviews*, 38(10):2887–2921, 2009.

[28] A. De Juan, J. Jaumot, and R. Tauler. Multivariate curve resolution (mcr). solving the mixture analysis problem. *Analytical Methods*, 6(14):4964–4976, 2014.

[29] T. Dey. Microplastic pollutant detection by surface enhanced raman spectroscopy (sers): a mini-review. *Nanotechnology for Environmental Engineering*, 8(1):41–48, 2023.

[30] A. N. Dodd, J. Kudla, and D. Sanders. The language of calcium signaling. *Annual review of plant biology*, 61(1):593–620, 2010.

[31] L. Dolan, K. Janmaat, V. Willemsen, P. Linstead, S. Poethig, K. Roberts, and B. Scheres. Cellular organisation of the arabidopsis thaliana root. *Development*, 119(1):71–84, 1993.

[32] A. Dutt and V. Rokhlin. Fast fourier transforms for nonequispaced data. *SIAM Journal on Scientific computing*, 14(6):1368–1393, 1993.

[33] T. C. elegans Sequencing Consortium*. Genome sequence of the nematode c. elegans: A platform for investigating biology. *Science*, 282(5396):2012–2018, 1998. doi: 10.1126/science.282.5396.2012.

[34] P. F. Favreau, C. Hernandez, T. Heaster, D. F. Alvarez, T. C. Rich, P. Prabhat, and S. J. Leavesley. Excitation-scanning hyperspectral imaging microscope. *Journal of biomedical optics*, 19(4):046010–046010, 2014.

[35] R. L. Feller. *Artist's pigments: a handbook of their history and characteristics. Vol. 1*, volume 1. 1986.

[36] A. Filler. Apodization and interpolation in fourier-transform spectroscopy. *JOSA*, 54(6):762–767, 1964.

[37] M. L. Forman, W. H. Steel, and G. A. Vanasse. Correction of asymmetric interferograms obtained in fourier spectroscopy. *JOSA*, 56(1):59–63, 1966.

[38] Y. Garini, I. T. Young, and G. McNamara. Spectral imaging: principles and applications. *Cytometry part a: the journal of the international society for analytical cytology*, 69(8):735–747, 2006.

[39] A. G. I. genomeanalysis@ tgr. org genomeanalysis@ gsf. de. Analysis of the genome sequence of the flowering plant arabidopsis thaliana. *nature*, 408(6814):796–815, 2000.

[40] G. Gilardi et al. *Analisi tre*. MC-GRAW-HILL, 1994.

[41] D. J. Griffiths. *Introduction to electrodynamics*. Cambridge University Press, 2023.

[42] P. R. Griffiths. Fourier transform infrared spectrometry. *Science*, 222(4621):297–302, 1983. doi: 10.1126/science.6623077.

[43] N. Hagen and M. W. Kudenov. Review of snapshot spectral imaging technologies. *Optical Engineering*, 52(9):090901–090901, 2013.

[44] P. Hamm and M. Zanni. *Concepts and methods of 2D infrared spectroscopy*. Cambridge University Press, 2011.

[45] B. Hammack, S. Kranz, and B. Carpenter. *Albert Michelson's Harmonic Analyzer: A Visual Tour of a Nineteenth Century Machine that Performs Fourier Analysis*. Articulate Noise Books, 2014.

[46] R. Heim and R. Y. Tsien. Engineering green fluorescent protein for improved brightness, longer wavelengths and fluorescence resonance energy transfer. *Current biology*, 6(2):178–182, 1996.

[47] J. G. Hirschberg, G. Vereb, C. K. Meyer, A. K. Kirsch, E. Kohen, and T. M. Jovin. Interferometric measurement of fluorescence excitation spectra. *Applied optics*, 37 (10):1953–1957, 1998.

[48] H. K. Hughes. The physical meaning of parseval's theorem. *American Journal of Physics*, 33(2):99–101, 1965.

[49] S. Jose, D. Joshy, S. B. Narendranath, and P. Periyat. Recent advances in infrared reflective inorganic pigments. *Solar Energy Materials and Solar Cells*, 194:7–27, 2019.

[50] A. Jullien, R. Pascal, U. Bortolozzo, N. Forget, and S. Residori. High-resolution hyperspectral imaging with cascaded liquid crystal cells. *Optica*, 4(4):400–405, 2017.

[51] V. Kiep, J. Vadassery, J. Lattke, J.-P. Maaß, W. Boland, E. Peiter, and A. Mithöfer. Systemic cytosolic ca2+ elevation is activated upon wounding and herbivory in arabidopsis. *New Phytologist*, 207(4):996–1004, 2015.

[52] V. P. Koldenkova and T. Nagai. Genetically encoded ca2+ indicators: Properties and evaluation. *Biochimica et Biophysica Acta (BBA)-Molecular Cell Research*, 1833(7):1787–1797, 2013.

[53] S. Kolenikov, G. Angeles, et al. The use of discrete data in pca: theory, simulations, and applications to socioeconomic indices. *Chapel Hill: Carolina Population Center, University of North Carolina*, 20:1–59, 2004.

[54] G.-J. Kremers, J. Goedhart, E. B. van Munster, and T. W. Gadella. Cyan and yellow super fluorescent proteins with improved brightness, protein folding, and fret förster radius. *Biochemistry*, 45(21):6570–6580, 2006.

[55] H. Kuzmany. *Solid-state spectroscopy: an introduction*. Springer Science & Business Media, 2009.

[56] J. R. Lakowicz. *Principles of fluorescence spectroscopy*. Springer, 2006.

[57] I. Lezcano-Gonzalez, E. Campbell, A. Hoffman, M. Bocus, I. Sazanovich, M. Towrie, M. Agote-Aran, E. Gibson, A. Greenaway, K. De Wispelaere, et al. Insight into the effects of confined hydrocarbon species on the lifetime of methanol conversion catalysts. *Nature Materials*, 19(10):1081–1087, 2020.

[58] G. Lu and B. Fei. Medical hyperspectral imaging: a review. *Journal of biomedical optics*, 19(1):010901–010901, 2014.

[59] G. Lutz et al. *Semiconductor radiation detectors*. Number PUBDB-2020-02521. Springer, 2007.

[60] J. Mertz. *Introduction to optical microscopy*. Cambridge University Press, 2019.

[61] L. Mertz. Auxiliary computation for fourier spectrometry. *Infrared Physics*, 7(1): 17–23, 1967.

[62] A. A. Michelson. Xxxviii. on the application of interference-methods to spectroscopic measurements.—i. *The London, Edinburgh, and Dublin Philosophical Magazine and Journal of Science*, 31(191):338–346, 1891.

[63] A. A. Michelson. Xxx. on the application of interference methods to spectroscopic measurements.—ii. *The London, Edinburgh, and Dublin Philosophical Magazine and Journal of Science*, 34(208):280–299, 1892.

[64] A. A. Michelson and S. W. Stratton. Art. i.–a new harmonic analyzer. *American Journal of Science (1880-1910)*, 5(25):1, 1898.

[65] R. S. Molina, Y. Qian, J. Wu, Y. Shen, R. E. Campbell, M. Drobizhev, and T. E. Hughes. Understanding the fluorescence change in red genetically encoded calcium ion indicators. *Biophysical journal*, 116(10):1873–1886, 2019.

[66] W. Müller, M. Kielhorn, M. Schmitt, J. Popp, and R. Heintzmann. Light sheet raman micro-spectroscopy. *Optica*, 3(4):452–457, 2016.

[67] S. Mustafa, J. Hannagan, P. Rigby, K. Pfleger, and B. Corry. Quantitative förster resonance energy transfer efficiency measurements using simultaneous spectral unmixing of excitation and emission spectra. *Journal of biomedical optics*, 18(2): 026024–026024, 2013.

[68] T. Nagai, S. Yamada, T. Tominaga, M. Ichikawa, and A. Miyawaki. Expanded dynamic range of fluorescent indicators for ca2+ by circularly permuted yellow fluorescent proteins. *Proceedings of the National Academy of Sciences*, 101(29): 10554–10559, 2004.

[69] M. Nicola, C. Garino, S. Mittman, E. Priola, L. Palin, M. Ghirardello, V. Damagatla, A. Nevin, A. Masic, D. Comelli, et al. Increased nir photoluminescence of egyptian blue via matrix effect optimization. *Materials Chemistry and Physics*, 313: 128710, 2024.

[70] R. Norton and R. Beer. Errata: New apodizing functions for fourier spectrometry. *JOSA*, 67(3):419–419, 1977.

[71] H. Nyquist. Certain topics in telegraph transmission theory. *Transactions of the American Institute of Electrical Engineers*, 47(2):617–644, 1928.

[72] A. Oriana, J. Réhault, F. Preda, D. Polli, and G. Cerullo. Scanning fourier transform spectrometer in the visible range based on birefringent wedges. *JOSA A*, 33(7): 1415–1420, 2016.

[73] C. Palmer and E. G. Loewen. Diffraction grating handbook. 2005.

[74] R. Pedrós, I. Moya, Y. Goulas, and S. Jacquemoud. Chlorophyll fluorescence emission spectrum inside a leaf. *Photochemical & photobiological sciences*, 7:498–502, 2008.

[75] L. Peng, J. A. Gardecki, B. E. Bouma, and G. J. Tearney. Fourier fluorescence spectrometer for excitation emission matrix measurement. *Optics express*, 16(14): 10493–10500, 2008.

[76] A. Perri, F. Preda, C. D'Andrea, E. Thyrhaug, G. Cerullo, D. Polli, and J. Hauer. Excitation-emission fourier-transform spectroscopy based on a birefringent interferometer. *Optics express*, 25(12):A483–A490, 2017.

[77] A. Perri, B. N. De Faria, D. T. Ferreira, D. Comelli, G. Valentini, F. Preda, D. Polli, A. De Paula, G. Cerullo, and C. Manzoni. Hyperspectral imaging with a twins birefringent interferometer. *Optics express*, 27(11):15956–15967, 2019.

[78] Y. Peter and M. Cardona. *Fundamentals of semiconductors: physics and materials properties*. Springer Science & Business Media, 2010.

[79] L. Piatkowski, E. Gellings, and N. F. Van Hulst. Broadband single-molecule excitation spectroscopy. *Nature communications*, 7(1):10411, 2016.

[80] H. M. Pickett and H. L. Strauss. Signal-to-noise ratio in fourier transform spectrometry. *Analytical Chemistry*, 44(2):265–270, 1972.

[81] G. Pozza, D. Ajò, G. Chiari, F. De Zuane, and M. Favaro. Photoluminescence of the inorganic pigments egyptian blue, han blue and han purple. *Journal of Cultural Heritage*, 1(4):393–398, 2000.

[82] T. Rajaramanan, M. Keykhaei, F. Gourji, et al. Eco-friendly egyptian blue (cacusi4o10) dye for luminescent solar concentrator applications. mater adv, 2023.

[83] C. V. Raman and K. S. Krishnan. A new type of secondary radiation. *Nature*, 121 (3048):501–502, 1928.

[84] M. Rüsing, S. Neufeld, J. Brockmeier, C. Eigner, P. Mackwitz, K. Spychala, C. Silberhorn, W. G. Schmidt, G. Berth, A. Zrenner, et al. Imaging of 180 ferroelectric domain walls in uniaxial ferroelectrics by confocal raman spectroscopy: Unraveling the contrast mechanism. *Physical Review Materials*, 2(10):103801, 2018.

[85] S. Sanna, S. Neufeld, M. Rüsing, G. Berth, A. Zrenner, and W. G. Schmidt. Raman scattering efficiency in litao 3 and linbo 3 crystals. *Physical Review B*, 91(22):224302, 2015.

[86] D. Sculley. Web-scale k-means clustering. In *Proceedings of the 19th international conference on World wide web*, pages 1177–1178, 2010.

[87] L. Stryer. Fluorescence spectroscopy of proteins: Fluorescent probes provide insight into the structure, interactions, and dynamics of proteins. *Science*, 162(3853):526–533, 1968.

[88] C. Sun, M. Wang, J. Cui, X. Yao, and J. Chen. Comparison and analysis of wavelength calibration methods for prism–grating imaging spectrometer. *Results in Physics*, 12:143–146, 2019.

[89] D. Sun, Y. Zhang, D. Wang, W. Song, X. Liu, J. Pang, D. Geng, Y. Sang, and H. Liu. Microstructure and domain engineering of lithium niobate crystal films for integrated photonic applications. *Light: Science & Applications*, 9(1):197, 2020.

[90] O. Svelto, D. C. Hanna, et al. *Principles of lasers*, volume 1. Springer, 2010.

[91] E. Thyrhaug, S. Krause, A. Perri, G. Cerullo, D. Polli, T. Vosch, and J. Hauer. Single-molecule excitation–emission spectroscopy. *Proceedings of the National Academy of Sciences*, 116(10):4064–4069, 2019.

[92] F. Vernuccio, R. Vanna, C. Ceconello, A. Bresci, F. Manetti, S. Sorrentino, S. Ghislanzoni, F. Lambertucci, O. Motiño, I. Martins, et al. Full-spectrum cars microscopy of cells and tissues with ultrashort white-light continuum pulses. *The Journal of Physical Chemistry B*, 127(21):4733–4745, 2023.

[93] R. Vogel, P. T. Prins, F. T. Rabouw, and B. M. Weckhuysen. Operando time-gated raman spectroscopy of solid catalysts. *Catal. Sci. Technol.*, 13:6366–6376, 2023. doi: 10.1039/D3CY00967J.

[94] D. N. Wadduwage, V. R. Singh, H. Choi, Z. Yaqoob, H. Heemskerk, P. Matsudaira, and P. T. So. Near-common-path interferometer for imaging fourier-transform spectroscopy in wide-field microscopy. *Optica*, 4(5):546–556, 2017.

[95] Y. W. Wang, N. P. Reder, S. Kang, A. K. Glaser, and J. T. Liu. Multiplexed optical imaging of tumor-directed nanoparticles: a review of imaging systems and approaches. *Nanotheranostics*, 1(4):369, 2017.

[96] R. Weis and T. Gaylord. Lithium niobate: Summary of physical properties and crystal structure. *Applied Physics A*, 37:191–203, 1985.

[97] W. Wien. Sitzungsber. dk akad. d. wissensch. zu berlin 6. 1893.

[98] N. Wiener. Generalized harmonic analysis. *Acta Mathematica*, 55:117–258, 1930.

[99] W. Xiong, C.-I. Chang, C.-C. Wu, K. Kalpakis, and H. M. Chen. Fast algorithms to implement n-findr for hyperspectral endmember extraction. *IEEE Journal of selected topics in applied earth observations and remote sensing*, 4(3):545–564, 2011.

[100] J. Zhao, C. Ma, M. Rüsing, and S. Mookherjea. High quality entangled photon pair generation in periodically poled thin-film lithium niobate waveguides. *Physical review letters*, 124(16):163603, 2020.

[101] Z. Zhou, B. Pain, and E. R. Fossum. Frame-transfer cmos active pixel sensor with pixel binning. *IEEE Transactions on electron devices*, 44(10):1764–1768, 1997.